



**TECHNISCHE
UNIVERSITÄT
DRESDEN**

Fakultät Umweltwissenschaften

Thema der Dissertation

Multiphysics processes in solid thermal energy storage

kumulative Dissertation zur Erlangung des akademischen Grades
Doktor der Naturwissenschaften (Dr. rer. nat.)

vorgelegt von

Dr.Eng. Miao, Xing-Yuan

geboren am: 05.09.1986 in: Sichuan, China

Gutachter:

Herr Prof. Dr.-Ing. habil. Markus Kästner
Technische Universität Dresden

Herr Dr. Fabien Magri
Freie Universität Berlin

Herr Prof. Dr. Zhongwen Ou
Army Logistics University of PLA

Dresden,

EXPLANATION OF THE DOCTORAL CANDIDATE

This is to certify that this copy is fully congruent with the original copy of the dissertation with the topic:

'Multiphysics processes in solid thermal energy storage'

hereby confirmed

.....
Place, Date

.....
Signature (surname, first name)

ABSTRACT

To enable the adaptability of solar thermal energy (STE) applications, e.g. concentrating solar power (CSP), to persistent energy demanding in spite of the intermittent nature of STE, thermal energy storage (TES) technologies are applied as attractive solutions to render STE-based systems more competitive on the electrical power market. Furthermore, solid TES systems are considered as a promising alternative compared to commonly used fluid storage solutions to further reduce the financial investment for the TES unit. From both engineering and commercialisation perspectives, it can be designed for componentisation to complete modular assembly to match designated loading supply for different scales of CSP plants. The successful integration of solid sensible heat storage (SHS) into parabolic trough power plants has been demonstrated in recent decade. At present, to provide ready service to direct domestic heat applications, TES technology for low temperatures has gained growing concern in addition to the electricity supplement. This offers the possibility to develop new mixed solid-liquid(water) storage materials to enhance the heat storage density, such as a novel water-saturated cementitious material designed for a national project of storing solar collector-supplied energy (IGLU project). However, because of the essence of solids, important specific issues have to be addressed to ensure the performance efficiency and stability of solid TES systems over a long period of operation. Present efforts from both academics and industry focus on thermal aspects as the primary concern. The solid TES is subjected to multiphysics processes, however, implying that the thermal behaviour will be a product of the mutual interaction of several involved physical fields and in turn affects the latter. Among them, the associated mechanical behaviour of the heat storage components has a major impact on the system reliability and durability, as well as thermal performance, because potential structural damage will significantly influence the heat transport through the TES structure and may endanger the integrity of the structure itself.

This contribution is motivated by the development of an innovative solid TES module (IGLU TES) for the above mentioned IGLU project. The research goal of this contribution is to examine the performance and integrity of solid TES with tubular heat exchangers under multiphysics conditions, specifically, to identify the possibilities and consequences of failure due to mechanical damage or thermal degradation. The research starts from a generalised thermo-hydro-mechanical (THM) analysis of the IGLU TES to gain an initial insight into the coupling effects between the different physical fields and their relative importance. Critical regions are then identified around the near field of the tubular heat exchanger judging from the critical stress fields that can challenge the structural integrity of solid TES by causing fractures in the involved materials. The critical regions thus determined inform the extended analysis specific to a structure of a solid TES with embedded tubular heat exchangers. Particularly, an analytical approach is proposed by making appropriate simplifications based on the preceding numerical analyses to perform a robust analysis on critical material and geometrical quantities that exert the most significant influence on structural reliability of solid TES system. The derived analytical solution can be processed to quantify the dependence of critical stresses on multiple parameters, guiding materials and geometry selection for the most promising system

optimisation with permitting great design flexibility for the storage configuration. Being analytical, the approach requires minimal effort and is suitable for early design phases. The analytical solution showed that the risk of material and structural failure cannot be reduced arbitrarily even under the optimal design configuration. Therefore, a phase-field approach to modelling fracture is developed to capture probable fracturing processes caused by the mismatch of thermal expansivities of the system components, and quantify the influence of the resulting fracture topologies on the thermal performance of a solid TES system. The proposed phase-field approach within a coupled thermo-mechanical setting is employed to two representative solid SHS configurations differing both in terms of the storage medium and the storage temperature levels. Fracturing is observed within the solid storage body, and the resulting thermal performance degradation as a result of a heat transport barrier associated with the trapped fluid medium of potentially low thermal conductivity is examined, leading to significant fluctuations of the heating power in a running system.

KURZFASSUNG

Um die zuverlässige Integration von Solarthermieanwendungen (ST), z. B. konzentrierte Solarenergie (*concentrating solar power*, CSP) bei steigendem Energiebedarf und trotz des fluktuierenden Charakters von ST zu ermöglichen, werden thermische Energiespeichertechnologien (TES) als attraktive Lösungen eingesetzt, um ST-basierte Systeme auf dem Energiemarkt wettbewerbsfähiger zu machen. Darüber hinaus werden Feststoff-TES-Systeme als vielversprechende Alternative zu herkömmlichen Flüssigkeitsspeicherlösungen betrachtet, um die Investitionskosten für die TES-Einheit weiter zu senken. Sowohl aus technischer als auch aus kommerzieller Sicht können sie vorteilhaft mittels der Komponentenfertigung bis hin zum kompletten modularen Aufbau ausgelegt werden, um die vorgesehene Beladungsmenge für verschiedene Leistungsbereiche von CSP-Anlagen abzudecken. Die erfolgreiche Integration von feststoffbasierten, sensiblen Wärmespeichern (SWS) in Parabolrinnen-Kraftwerken hat sich in den letzten zehn Jahren bewährt. Gegenwärtig gewinnt die TES-Technologie für niedrige Temperaturen neben Hochtemperaturanwendungen zur Stromerzeugung zunehmend an Bedeutung. Dies bietet die Möglichkeit, neue gemischte Feststoff-Flüssigkeits-Speichermaterialien zu entwickeln, um die Wärmespeicherdichte zu erhöhen, wie hier am Beispiel eines neuartigen, wassergesättigten zementartigen Materials demonstriert wird, das im Rahmen eines nationalen Projekts zur Speicherung von mit Solarkollektoren gewonnener Energie (IGLU-Projekt) entwickelt wurde. Wegen typischer Eigenschaften der Feststoffe müssen jedoch wichtige spezifische Probleme gelöst werden, um die Leistungsfähigkeit und Stabilität von festen TES-Systemen über einen langen Zeitraum zu gewährleisten. Die gegenwärtigen Bemühungen von Wissenschaft und Industrie konzentrieren sich auf thermische Aspekte als zentrales Hauptanliegen. Feststoffbasierte TES sind jedoch multiphysikalischen Prozessen unterworfen, d.h. das thermische Verhalten ist ein Produkt der gegenseitigen Wechselwirkung mehrerer beteiligter physikalischer Felder und beeinflusst selbst wiederum diese Felder. Das damit verbundene mechanische Verhalten der Wärmespeicherkomponenten hat einen großen Einfluss auf die Zuverlässigkeit und Haltbarkeit des Systems sowie die thermische Leistung, da mögliche Strukturschäden den Wärmetransport durch die TES-Struktur erheblich beeinflussen und die Integrität der Struktur selbst gefährden können.

Die Motivation dieses Beitrags liegt in der Entwicklung eines innovativen feststoffbasierten TES-Moduls (IGLU TES) für das oben genannte IGLU-Projekt. Ziel dieses Beitrags ist es, die Leistungsfähigkeit und Integrität von feststoffbasierten TES mit Röhrenwärmetauschern unter multiphysikalischen Bedingungen zu untersuchen, um insbesondere die Möglichkeiten und Folgen eines Versagens durch mechanische Schädigung oder thermische Degradation zu identifizieren. Die Arbeit geht von einer verallgemeinerten thermo-hydro-mechanischen (THM) Analyse des IGLU TES aus, um einen ersten Einblick in die Kopplungseffekte zwischen den verschiedenen physikalischen Feldern und deren relative Bedeutung zu gewinnen. Kritische Bereiche in den Zonen um den Röhrenwärmetauscher werden dann anhand der sich einstellenden Spannungsfelder als kritisch identifiziert, da sie die strukturelle Integrität des Speichermoduls beeinträchtigen können, indem in diesen Zonen

die Festigkeit charakterisierende oder bruchmechanische Kriterien überschritten werden. Die so ermittelten kritischen Bereiche erlauben eine vertiefte, strukturspezifische Analyse eines feststoffbasierten TES mit eingebetteten Röhrenwärmetauschern. Insbesondere wird ein analytischer Ansatz vorgeschlagen, indem geeignete Vereinfachungen auf der Grundlage der vorangegangenen numerischen Analysen vorgenommen werden, um eine robuste Analyse derjenigen materialspezifischen und geometrischen Größen durchzuführen, die den größten Einfluss auf die strukturelle Zuverlässigkeit des Speichermoduls ausüben. Die abgeleitete analytische Lösung kann zur Quantifizierung der Abhängigkeit kritischer Spannungen von mehreren Systemparametern, Materialkennwerten und Geometriegrößen herangezogen werden, um unter gewählten Gesichtspunkten eine Systemoptimierung mit großer Designflexibilität für die Speicherkonfiguration durchzuführen. Der analytische Ansatz erfordert nur minimalen Aufwand und eignet sich für frühe Designphasen. Dabei zeigte sich, dass das Risiko von Material- und Strukturversagen auch bei optimaler Auslegung nicht beliebig reduziert werden kann. Daher wird ein Phasenfeld-Ansatz zur Modellierung von Risswachstumsprozessen entwickelt, um wahrscheinliche Schädigungsmuster zu erfassen, die durch die Nichtübereinstimmung der thermischen Ausdehnungskoeffizienten der Systemkomponenten verursacht werden, und den Einfluss der resultierenden Ristopologien auf das thermische Verhalten eines festen TES-Systems zu quantifizieren. Der vorgeschlagene Phasenfeldansatz, formuliert innerhalb eines gekoppelten thermomechanischen Ansatzes, wird auf zwei repräsentative feste SWS-Konfigurationen angewendet, die sich sowohl hinsichtlich des Speichermediums als auch der Speichertemperatur unterscheiden. Innerhalb des Festkörpers wird ein Bruchvorgang beobachtet und die daraus resultierende thermische Leistungsabnahme durch eine Wärmetransportbehinderung in Abhängigkeit des eingeschlossenen flüssigen Mediums mit potentiell niedriger Wärmeleitfähigkeit untersucht, was zu erheblichen Schwankungen der Heizleistung in einem laufenden System führen kann.

LIST OF PUBLICATIONS

JOURNAL PUBLICATIONS

- X.-Y. Miao, O. Kolditz, T. Nagel, Modelling thermal performance degradation of high and low-temperature solid thermal energy storage due to cracking processes using a phase-field approach. *Energy Conversion and Management*, Volume 180, January 2019, Pages 977-989.
- X.-Y. Miao, T. Zheng, U.-J. Görke, O. Kolditz, T. Nagel, Thermo-mechanical analysis of heat exchanger design for thermal energy storage systems. *Applied Thermal Engineering*, Volume 114, March 2017, Pages 1082-1089.
- X.-Y. Miao, C. Beyer, U.-J. Görke, O. Kolditz, H. Hailemariam, T. Nagel, Thermo-hydro-mechanical analysis of cement-based sensible heat stores for domestic applications. *Environmental Earth Sciences*, Volume 75, Issue 18, September 2016, Article:1293.
- T. Zheng, X.-Y. Miao, D. Naumov, H. Shao, O. Kolditz, T. Nagel, A thermo-hydro-mechanical finite-element model with freezing processes in saturated soils. *Environmental Geotechnics*, doi: <https://doi.org/10.1680/jenge.18.00092>.
- F. Parisio, A. Tarokh, R. Makhnenko, D. Naumov, X.-Y. Miao, O. Kolditz, T. Nagel, Experimental characterization and numerical modelling of fracture processes in granite. *International Journal of Solids and Structures*, Volume 163, May 2019, Pages 102-116.

EXTENDED CONFERENCE PROCEEDINGS

- X.-Y. Miao, T. Zheng, O. Kolditz, T. Nagel, Phase-field modeling of cracking processes in geomaterials for subsurface geotechnical engineering and energy storage. *Advance of Computer Methods in Geomechanics: Proceedings of the fifteenth International Conference of the International Association for Computer Methods and Advanced in Geomechanics*, Wuhan, China, October 19-23, 2017, accepted.
- X.-Y. Miao, O. Kolditz, T. Nagel, Phase-field modeling of fracture in poroelastic solids for thermal energy storage. *Poromechanics VI: Proceedings of the Sixth Biot Conference on Poromechanics*, Paris, France, July 9-13, 2017, Pages 1976-1983.
- T. Zheng, X.-Y. Miao, D. Naumov, H. Shao, O. Kolditz, T. Nagel, A thermo-hydro-mechanical finite element model of freezing in porous media – thermo-mechanically consistent formulation and application to ground source heat pumps. *Proceedings of the Seventh International Conference on Computational Methods for Coupled Problems in Science and Engineering*, Rhodes Island, Greece, June 12-14, 2017, Pages 1008-1019.

CHAPTERS IN BOOKS

X.-Y. Miao, J. Maßmann, T. Nagel, D. Naumov, F. Parisio, P. Vogel. M processes. In O. Kolditz, T. Nagel, H. Shao, W. Wang, S. Bauer (Eds.), *Thermo-Hydro-Mechanical-Chemical Processes in Fractured Porous Media: Modelling and Benchmarking: From Benchmarking to Tutoring*, Chapter 3, Pages 37-116. New York: Springer, 2018.

P. Vogel, J. Maßmann, X.-Y. Miao, T. Nagel. TM processes. In O. Kolditz, T. Nagel, H. Shao, W. Wang, S. Bauer (Eds.), *Thermo-Hydro-Mechanical-Chemical Processes in Fractured Porous Media: Modelling and Benchmarking: From Benchmarking to Tutoring*, Chapter 9, Pages 187-217. New York: Springer, 2018.

P. Vogel, J. Maßmann, T. Zheng, X.-Y. Miao, D. Naumov, T. Nagel. THM processes. In O. Kolditz, T. Nagel, H. Shao, W. Wang, S. Bauer (Eds.), *Thermo-Hydro-Mechanical-Chemical Processes in Fractured Porous Media: Modelling and Benchmarking: From Benchmarking to Tutoring*, Chapter 10, Pages 219-251. New York: Springer, 2018.

F. Magri, M. Cacace, T. Fischer, D. Naumov, W. Wang, N. Watanabe, T. Zheng, X.-Y. Miao, T. Nagel, M. Walther. HT (Convection) Processes. In O. Kolditz, T. Nagel, H. Shao, W. Wang, S. Bauer (Eds.), *Thermo-Hydro-Mechanical-Chemical Processes in Fractured Porous Media: Modelling and Benchmarking: From Benchmarking to Tutoring*, Chapter 7, Pages 157-177. New York: Springer, 2018.

T. Nagel, J. Maßmann, X.-Y. Miao, Peter Vogel. Thermomechanics. In O. Kolditz, U.-J. Görke, W. Wang, H. Shao, S. Bauer (Eds.), *Thermo-Hydro-Mechanical-Chemical Processes in Fractured Porous Media: Modelling and Benchmarking: Benchmarking Initiatives*, Chapter 8, Pages 139-156. New York: Springer, 2016.

ACKNOWLEDGEMENTS

The work presented in this thesis is the results of the research project on Intelligent Thermal Energy Storage, carried out between 2015 and 2018, when I was a research scientist at Department Umweltinformatik in Helmholtz-Zentrum für Umweltforschung (UFZ). The past three years in the institute has been one of my best experiences until now. I would like to take this opportunity to thank the people contributed to the realisation of this work - all their support is most gratefully acknowledged.

First of all, I would like to sincerely express my appreciation to my supervisor Professor Olaf Kolditz for giving me the opportunity to prepare my thesis at the department, for his scientific support, and for the very interesting and promising discussions. His research in the field of coupled thermo-hydro-mechanical-chemical (THMC) processes in fractured porous media built the important foundation for this work. I appreciate that he has always encouraged me and provided me the chances to attend conferences, workshops, and international courses to learn from the great minds of different fields and to have greater insight into the scientific work that I would like to spend the whole life making contribution to.

Next, I want to thank the group leader of Computational Energy Systems at Department Umweltinformatik, Professor Thomas Nagel for initiating the research project, for the very helpful discussions, innovative ideas, critical and detailed comments to achieve an outstanding quality of the performed research and to improve my professional skills. My fundamental understanding on the Theory of Porous Media is thanks to Thomas' professional and patient guidance with his advanced knowledge.

I am very grateful to Professor Rudolf Liedl for his great and selfless scientific support and help. I deeply admire his profound knowledge and outstanding personalities, and very appreciate his recognition and encouragement for my scientific work.

I would like to particularly thank Doctor Fabien Magri at Freie Universität Berlin, Doctor Cui Chen at Helmholtz-Zentrum für Umweltforschung, Professor Zhaohui Chen at Chongqing University, Doctor Hua Shao at Bundesanstalt für Geowissenschaften und Rohstoffe, Professor Qi Li at Institute of Rock and Soil Mechanics of Chinese Academy of Sciences, Professor Zhongwen Ou at Army Logistics University, my supervisors in my master and first PhD period, Professor Tingsheng Zhao and Professor Guoqing Li for their very important support and help concerning my future academic perspective.

Moreover, I want to thank all the colleagues at the institute for creating a pleasant and friendly working atmosphere. Especially, I want to thank Doctor Wenqing Wang for his technical support and academic advice all the way. I appreciate having Professor Haibing Shao, Renchao Lu, Tianyuan Zheng, Yonghui Huang, and Leslie Jakobs' kindly and thoughtful care and help in my daily life.

Finally, I would like to express my deeply gratitude to my family and especially my parents, my grandparents, and Xin Zhang for their always completely support and encouragement.

Dedicated to Liang Yang, my mother

CONTENTS

1	INTRODUCTION AND OVERVIEW	1
1.1	Motivation	1
1.2	Scope, aims and state of the art	3
1.3	Outline of the thesis	4
I THERMO-HYDRO-MECHANICAL ANALYSIS OF SOLID THERMAL ENERGY STORAGE		
2	THERMO-HYDRO-MECHANICAL ANALYSIS OF A NOVEL MIXED SOLID-LIQUID SENSIBLE HEAT STORAGE	7
2.1	Thermo-hydro-mechanical analysis of a testing module for system development	8
2.2	Conclusion	12
3	THERMO-MECHANICAL ANALYSIS OF HEAT EXCHANGER DESIGN FOR SOLID THERMAL ENERGY STORAGE SYSTEMS	14
3.1	Characterisation of physical quantities on the mechanical behaviour of solid thermal energy storage	15
3.2	Conclusion	17
II PHASE-FIELD APPROACH FOR CHARACTERISATION OF FRACTURING IN SOLID THERMAL ENERGY STORAGE		
4	PHASE-FIELD APPROACH FOR THE IDENTIFICATION OF THERMO-MECHANICAL FRACTURING IN SOLID THERMAL ENERGY STORAGE	20
4.1	Model formulation for brittle fracture in thermo-elastic solids	20
4.1.1	The concept of a diffusive crack	20
4.1.2	Constitutive equations of thermo-elasticity in thermodynamics	20
4.1.3	Degradation of elastic energy and heat conduction	22
4.2	Thermal fracturing in solid sensible heat storage	22
4.3	Conclusion and discussion	24
5	SUMMARY AND OUTLOOK	25
5.1	Summary	25
5.2	Outlook	26
Appendix		38
1	Processes development in OGS	38
1.1	A visco-elastic material model for simple-shear creep	38
1.2	An elasto-plastic material model with hardening	38
1.3	A phase-field model of brittle fracture	39
1.4	A thermo-mechanical material model for elastic solids	39
1.5	A thermo-mechanical phase-field model of brittle fracture	39
1.6	A thermo-hydro-mechanical model for porous media	40
2	Detailed description of models development and applications	41
2.1	Governing equations for fluid-saturated porous media	41
2.2	Thermo-hydro-mechanical modelling of solid-fluid sensible heat storage	43
2.3	Thermo-mechanical modelling of solid thermal energy storage with integrated heat exchangers	61

2.4	Phase-field modelling of fracture in poroelastic solids	70
2.5	Phase-field modelling of fracture in thermo-elastic solids	79
2.6	Thermo-mechanical phase-field modelling of fracture for solid thermal energy storage	92

NOMENCLATURE

Throughout this contribution bold face symbols denote tensors and vectors. Normal face letters represent scalar quantities.

Greek symbols

α	constituent identifier in subscript and superscript, $\alpha = \{S, F\}$	
$\bar{\alpha}_i$	plane strain linear thermal expansion coefficient of the material phase i	[K ⁻¹]
α_{TS}	thermal expansion coefficient tensor of solid phase	[K ⁻¹]
$\beta_{T\alpha}$	volumetric coefficient of thermal expansion of the constituent α	[K ⁻¹]
β_{Teff}	effective volumetric coefficient of thermal expansion of the mixture	[K ⁻¹]
γ	crack-surface density	[m ⁻¹]
Γ	crack surface	
ε	length-scale parameter	[m]
ϵ	small strain tensor	[-]
ϵ_{el}	elastic strain tensor	[-]
ϵ_{th}	thermal strain tensor	[-]
η	specific entropy	[J K ⁻¹ kg ⁻¹]
ϑ	absolute temperature	[K]
ϑ_0	reference temperature	[K]
κ_F	intrinsic permeability tensor	[m ²]
λ_d	thermal conductivity tensor of crack-phase	[J m ⁻¹ K ⁻¹ s ⁻¹]
λ_F	thermal conductivity tensor of fluid phase	[J m ⁻¹ K ⁻¹ s ⁻¹]
λ_S	thermal conductivity tensor of intact solid phase	[J m ⁻¹ K ⁻¹ s ⁻¹]
λ_{eff}	effective thermal conductivity tensor	[J m ⁻¹ K ⁻¹ s ⁻¹]
μ	shear modulus	[N m ⁻²]
μ_{FR}	effective dynamic viscosity of the pore fluid	[N s m ⁻²]
$\bar{\nu}_i$	plane strain Poisson's ratio of the material phase i	[-]
ξ	threshold	[-]
ρ_α	partial density of the constituent α	[kg m ⁻³]
$\rho_{\alpha R}$	effective (realistic) density of the constituent α	[kg m ⁻³]
ρ_{eff}	effective (realistic) density of the mixture	[kg m ⁻³]
$\sigma_{\phi\phi}^i$	circumferential stress of the material phase i in cylindrical coordinates	[N m ⁻²]
σ_{rr}^i	radial stress of the material phase i in cylindrical coordinates	[N m ⁻²]
σ_{zz}^i	axial stress of the material phase i in cylindrical coordinates	[N m ⁻²]
σ_{mp}	critical stress	[N m ⁻²]
σ	Cauchy stress tensor	[N m ⁻²]
σ_S^E	effective stress tensor	[N m ⁻²]
ϕ_α	volume fraction of the constituent α	[-]
ψ	Helmholtz free energy density	[J m ⁻³]
ψ_m	mechanical part of Helmholtz free energy density	[J m ⁻³]
ψ_{th}	thermal part of Helmholtz free energy density	[J m ⁻³]
ψ_{surf}	crack surface energy density	[J m ⁻³]

$\bar{\psi}$	specific Helmholtz free energy	[J kg ⁻¹]
$\bar{\psi}_\alpha$	specific Helmholtz free energy of the constituent α	[J kg ⁻¹]
Ω	spatial domain of a solid body	
$\partial\Omega_u, \partial\Omega_\theta$	Dirichlet boundaries of a solid body	
$\partial\Omega_t, \partial\Omega_q$	Neumann boundaries of a solid body	

Operators

$\mathbf{a} \cdot \mathbf{b}$	dot product of \mathbf{a} and \mathbf{b}	
$\mathbf{A} : \mathbf{B}$	double contraction of \mathbf{A} and \mathbf{B}	
$\langle \cdot \rangle_\pm$	signed Macauley brackets: $\langle \cdot \rangle_\pm = [\cdot \mp \cdot]/2$	
$(\cdot)^D$	deviatoric part of a tensor	
$(\cdot)'_S$	material time derivative of a quantity with respect to the solid motion: $(\cdot)'_S = \partial(\cdot)/\partial t + \text{grad}(\cdot) \cdot \mathbf{v}_S$	
$\text{div}()$	divergence operator	
$\text{grad}()$	gradient operator	
$\text{tr}()$	trace operator	

Roman symbols

A_i, C_i	integration constants of the material phase i	[N, N m ⁻²]
c_p	isobaric specific heat capacity of the mixture	[J kg ⁻¹ K ⁻¹]
$c_{p\alpha}$	isobaric specific heat capacity of the constituent α	[J kg ⁻¹ K ⁻¹]
\mathbf{C}	fourth-order stiffness tensor	[N m ⁻²]
d	crack-phase indicator	[-]
D	dimension in space	[-]
D_S	gradient of σ_{mp} with respect to S	[N m ⁻³]
e_m	volumetric strain of the mixture	[-]
e_{th}	volumetric thermal strain	[-]
\bar{E}_i	plane strain Young's modulus of the material phase i	[N m ⁻²]
\mathbf{g}	gravitational acceleration vector ($ \mathbf{g} = 9.81 \text{ m s}^{-2}$)	[m s ⁻²]
G_c	critical Griffith-type energy release rate	[J m ⁻²]
i	material phase identifier in superscript and subscript, $i = \{a, b\}$	
\mathbf{I}	second-order identity tensor	[-]
K	bulk modulus	[N m ⁻²]
K_S	bulk modulus of solid skeleton	[N m ⁻²]
l_{ch}	material's internal length	[m]
l_G	Griffith length	[m]
\mathbf{n}	outward unit normal vector	[-]
p	pore fluid pressure	[N m ⁻²]
p_i	pressure applied on inner or outer boundaries of the material phase i	[N m ⁻²]
$\hat{\mathbf{p}}_\alpha$	volume-specific direct momentum production of the constituent α	[N m ⁻³]
$\hat{\mathbf{p}}_\alpha^E$	volume-specific extra momentum production of the constituent α	[N m ⁻³]
\mathbf{q}	heat flux	[J m ⁻² s ⁻¹]
r	radius in cylindrical coordinate system	[m]
r_{ii}	inner radius of the material phase i	[m]
r_{io}	outer radius of the material phase i	[m]
S	tube pitch	[m]

T	absolute temperature	[K]
T_0	reference temperature	[K]
\mathbf{u}_S	solid displacement vector	[m]
\mathbf{v}_F	fluid velocity vector	[m s ⁻¹]
\mathbf{w}_{FS}	fluid seepage velocity vector ($\mathbf{w}_{FS} = \mathbf{v}_F - \mathbf{v}_S$)	[m s ⁻¹]

ACRONYMS

STE	solar thermal energy
CSP	concentrating solar power
TES	thermal energy storage
SHS	sensible heat storage
LHS	latent heat storage
TCS	thermo-chemical storage
LT	low temperature
HT	high temperature
FEM	finite element method
OGS	the open-source finite element platform OpenGeoSys
THMC	thermo-hydro-mechanical-chemical
THM	thermo-hydro-mechanical
TM	thermo-mechanical
TPM	the Theory of Porous Media
AA	aluminium alloy
PEHD	high density polyethylene/polyethylene HD
AA-PE	aluminium-polyethylene
HTF	heat transfer fluid
PDE	partial differential equation

INTRODUCTION AND OVERVIEW

1.1 MOTIVATION

Driven by the thirst for sustainable energy production and storage with a low environmental impact of engineered solutions [22], the utilisation of solar thermal energy (STE) in energy systems has gained extensive popularity [43, 119]. The harvested solar thermal energy can be either directly employed to support domestic thermal use (Figure 1a), or converted into electricity by concentrating solar power (CSP) technologies (Figure 1b) [110]. One of the principal hindrances that limits the economic applications of STE is the mismatch between the intermittent power supply and the persistent power demand, cf. [14, 21, 44, 54, 75, 104, 118]. CSP coupled thermal energy storage (TES) technologies can convert solar energy into electricity with dispatchable flexibility, which is a major advantage over other converting systems, such as photovoltaics. To facilitate a reliable dispatch of STE-based power systems, TES modules are integrated to take the role of thermal batteries for the storage/release of surplus heating power [35, 38, 44, 46, 57, 70, 77, 96, 115]. The successful implementation of TES solutions into STE-based power systems for the management of the generated solar thermal power promotes the active development associated by means of high efficiency and economical flexibility for different system scales.

Three main technologies are available for implementing TES units (Figure 2): sensible heat storage (SHS), latent heat storage (LHS), and thermo-chemical storage (TCS). Sensible heat storage stores or releases the thermal energy by raising or lowering the temperature of a liquid or solid storage medium. Latent heat storage absorbs or releases energy primarily through a phase change of the storage material. Thermo-chemical storage converts and releases thermal energy by reversible chemical reactions or adsorption processes. The implementation of LHS and TCS remains a challenging issue due to technical and economic difficulties, cf. [4, 39, 58, 80, 81, 101]. Particularly, the costs associated with the storage materials, the complex heat transfer system components as well as peripherals, and the incorporation into a larger energy supply system are much higher for LHS and TCS than for SHS, cf. [3, 49, 109, 117]. Sensible heat storage is therefore an attractive solution in practical TES engineering for efficient and stable utilisation of solar thermal power (Figure 1), cf. [24, 26, 27, 36, 49, 63, 94, 105, 118].

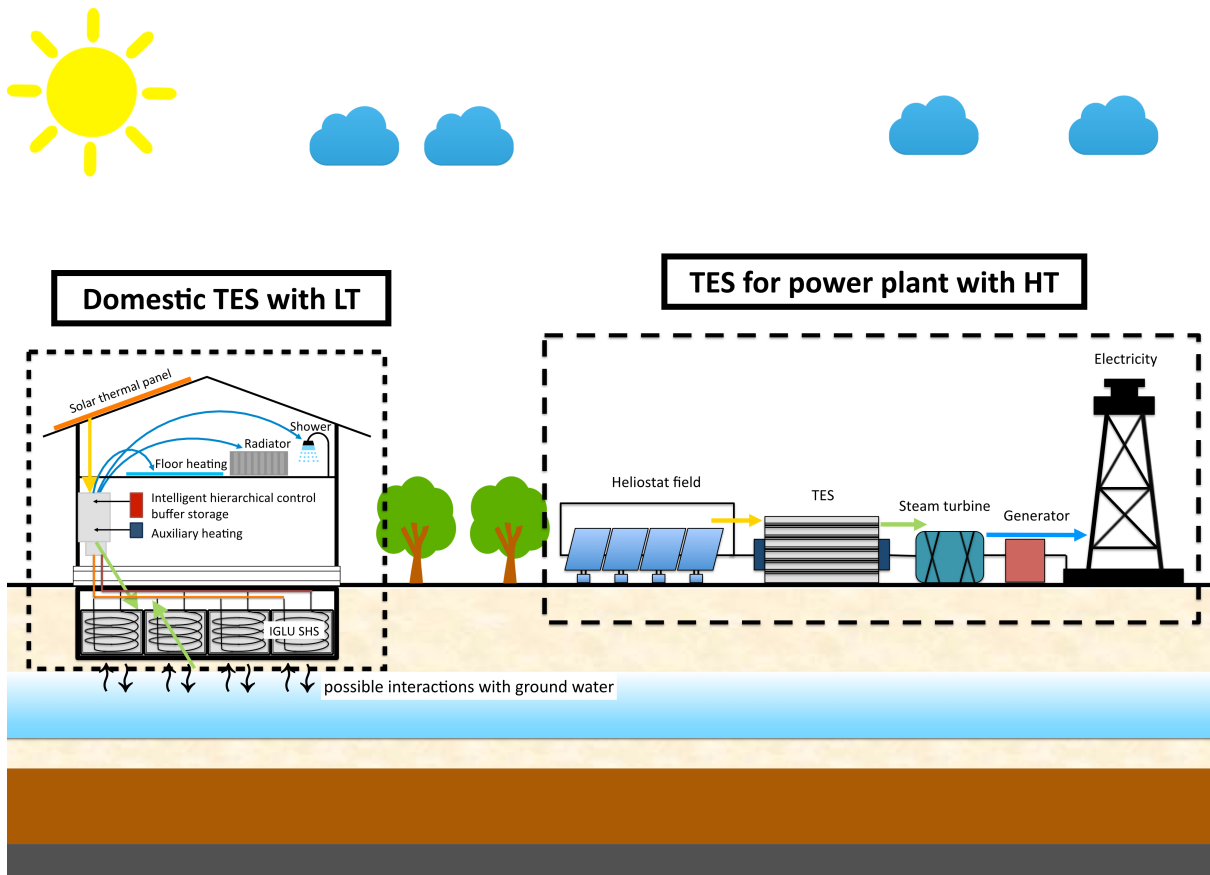


Figure 1: Design and construction of solid TES systems for specific applications. (a) TES operating at low temperature for domestic applications. Due to the integration into the shallow subsurface, potential interactions with ground water need to be considered; (b) TES operating at high temperature for solar thermal power plants.

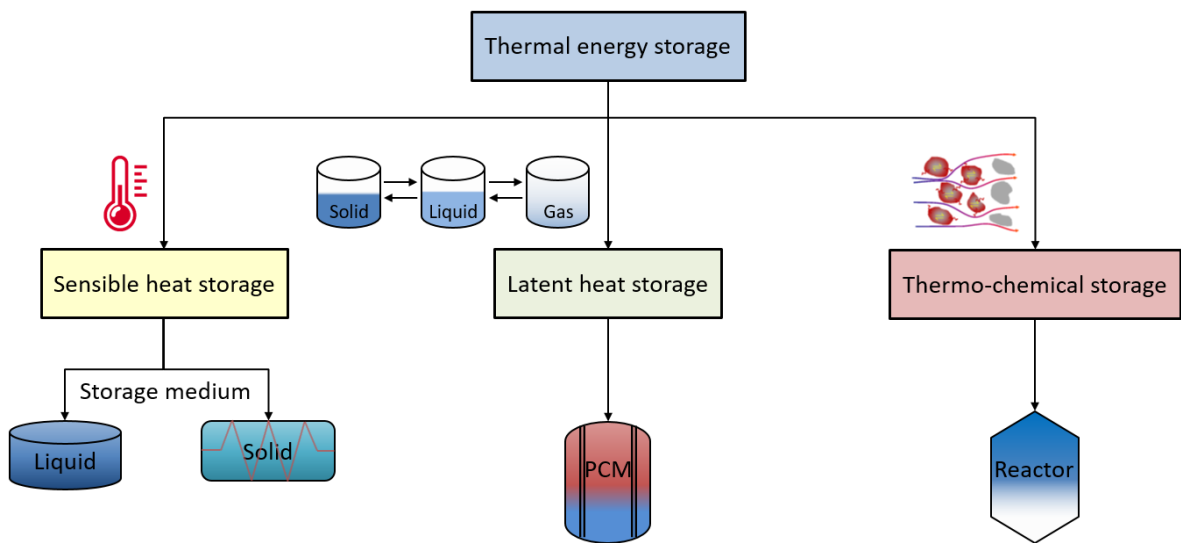


Figure 2: Thermal energy storage solutions based on different mechanisms.

1.2 SCOPE, AIMS AND STATE OF THE ART

The present study is focused on sensible heat storage (SHS) using a solid or a mixed solid-liquid storage medium. It is the aim of this contribution to examine the mechanical integrity and the thermal performance of solid SHS systems by taking into account specific multiphysics processes. Material and geometrical aspects affecting the critical stresses that might cause structural damage are discussed. Particularly, fracturing processes induced by the mismatched thermal expansion between the storage medium and the heat exchanger are identified. The consequent changes due to cracking in relevant thermal and mechanical properties implying the behaviour instability or degradation of solid SHS are quantified as well.

In spite of the attractive system efficiencies and environmental benefits associated with TES technology, it still faces challenges in view of large-scale commercial applications in association with specific system power and scale, as well as economic requirements. Comparing to the fluid storage medium (mineral/synthetic oils, molten salts, etc.), a significant cost reduction can be achieved by the alternative use of appropriate natural or artificial solid materials, such as concrete, rocks, and ceramics as the storage medium despite a moderate expense in terms of the energy storage capacity, cf. [52, 59, 60, 61, 71, 76, 90, 98, 102]. Intensive research and development on solid storage media have been performed to optimise the performance of specific TES systems, such as increasing the heat capacity, shortening the charging/discharging time, and strengthening the thermal and mechanical stability of the storage medium at high temperatures, cf. [5, 36, 60, 73, 90, 94, 102, 116]. Therein, concrete composites are mentioned as a promising solid medium for SHS system from technical and economic perspectives [52, 74]. An in-situ investigation of the integration of concrete TES units into parabolic trough solar thermal power plants has been reported by Laing and coworkers [71, 72] with a particular focus on the long-term storage performance.

For the performance characterisation of solid storage materials, particularly cementitious composites, many experimental tests have been conducted. For example, Laing et al. [73] tested the long-term behaviour of two distinct storage materials (a castable ceramic and a high-temperature concrete) developed by Tamme et al. [106]. John et al. [61] developed an economical high-temperature concrete mixture with a temperature resistance of up to 600 °C. Ozger et al. [92] produced a nylon fibre-reinforced concrete as the storage material to enhance both the thermal and the mechanical performance. The thermal properties and stability of such concrete mixture were investigated at a range of temperature levels up to 450 °C. Skinner et al. [102] examined an ultrahigh-performance concrete incorporated into a TES system capable of resisting temperatures of up to 500 °C. Note that they observed significant thermally induced cracking in concrete as a consequence of the mismatched thermal expansion between the concrete storage medium and the heat exchanger. Alonso et al. [5] designed a calcium aluminate cement-based storage material and tested its long-term stability under thermal cycles at high temperatures up to 550 °C.

Thermal efficiency and mechanical stability are of major concern to solid SHS systems both scientifically and industrially. Previous studies have implied that a promising solid SHS system must not only achieve a high thermal efficiency, but also maintain functional reliability under incessant multiphysics proceedings. In this contribution, the study of the most dominant quantities that have a major impact on the performance of solid SHS is first performed with

respect to a prototype SHS (Figure 1a) which is currently being developed as the TES module in a national STE project (IGLU¹ SHS). The developed analytical and numerical approaches are further extended to assist the multi-disciplinary design of solid TES structure with tubular heat exchangers. The subject of this study is (i) to quantify the influence of material properties and geometric dimensions on the performance characteristics of a solid TES module; (ii) to optimise the structural integrity and stability of solid TES systems from a thermo-mechanical perspective; (iii) to examine the probable thermal performance degradation of solid TES systems due to the progression of structural damage. To perform analyses based on the presented constitutive models, governing partial differential equations (PDEs) are solved by the scientific open-source finite element platform OpenGeoSys (OGS), in applying either monolithic or staggered schemes.

1.3 OUTLINE OF THE THESIS

The present thesis is organised as follows: Starting with Chapter 2, the concept of IGLU SHS is explained first. A comprehensive study on this SHS with respect to a primary thermo-hydro-mechanical (THM) analysis proceeding from the Theory of Porous Media (TPM) is performed. This study lays its emphasis on mechanics and fluid hydraulics within the SHS module subjected to external thermal and mechanical loading. The basic governing equations of coupled thermo-hydro-mechanical processes in porous media are briefly introduced to build the numerical model. Numerical simulations are employed for the system development and the prediction of potential failures of this specific SHS structure. The dominant set of processes is identified. Based on these results, an analytical solution based on thermo-mechanical arguments is developed to robustly evaluate the mechanical fields around the heat exchanger and the storage material. According to the findings from Chapter 2, Chapter 3 proposes an analytical approach which is extended from the analytical solution derived in Chapter 2 to perform extensive sensitivity analyses and quantify optimal properties in the sense of achieving a minimal critical stress response. While the previous chapters investigated the possible onset of damage, Chapter 4 studies its progression and quantifies the thermal performance degradation of solid TES modules associated with mechanical damage. A thermo-mechanically coupled phase-field model is developed to examine the thermally induced fracturing within the solid storage medium initiating around the embedded heat exchangers. The basic concept and mathematical model of a phase-field approach applied in this study are presented as well. A final summary including the main conclusions and discussions is stated in Chapter 5 together with a prospect onto further possible developments and model applications based on the present work.

¹ "Untersuchung, Modellierung und Bewertung eines intelligenten geothermischen Langzeitwärmespeichers mit umweltneutralem Verhalten", or "Analysis, Modelling and assessment if an intelligent and environmentally neutral geothermal long-term heat storage system." is a project funded by the German Federal Ministry for Economic Affairs and Energy (BMWi).

Part I

THERMO-HYDRO-MECHANICAL ANALYSIS OF SOLID
THERMAL ENERGY STORAGE

The detailed study of this part is included in:

X.-Y. Miao, C. Beyer, U.-J. Görke, O. Kolditz, H. Hailemariam, T. Nagel, Thermo-hydro-mechanical analysis of cement-based sensible heat stores for domestic applications. *Environmental Earth Sciences*, Volume 75, Issue 18, September 2016, Article:1293.

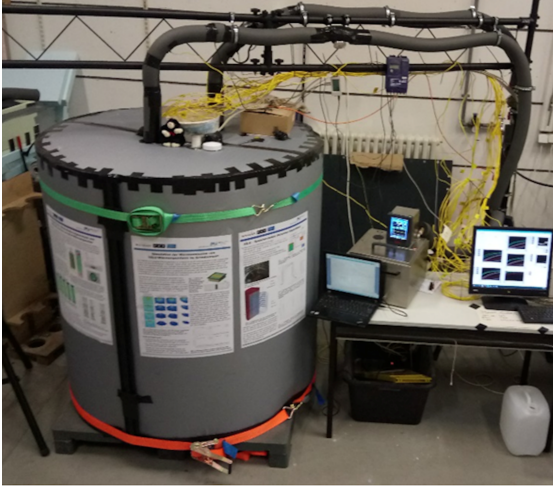
X.-Y. Miao, T. Zheng, U.-J. Görke, O. Kolditz, T. Nagel, Thermo-mechanical analysis of heat exchanger design for thermal energy storage systems. *Applied Thermal Engineering*, Volume 114, March 2017, Pages 1082-1089.

THERMO-HYDRO-MECHANICAL ANALYSIS OF A NOVEL MIXED SOLID-LIQUID SENSIBLE HEAT STORAGE

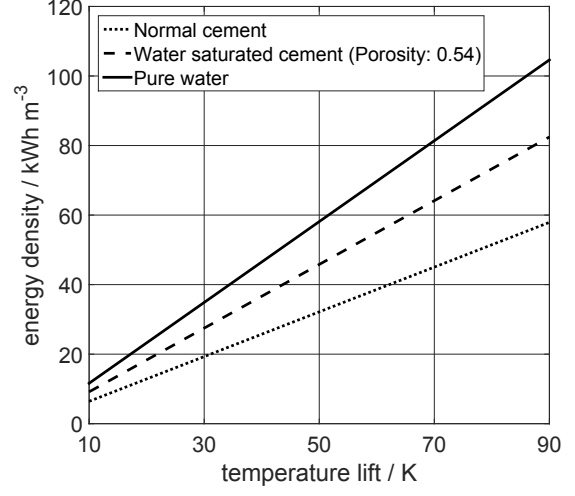
In this chapter, the thermo-hydro-mechanical analysis to mixed solid-liquid TES system is performed on a novel prototype SHS (see Figure 3a) with emphasis on the mechanical behaviours under such multiphysics conditions.

Currently, the most prevalent SHS system is a storage tank with water (domestic) or molten salt (high-temperature applications for power generation) as heat storage media, cf. [49, 53, 70]. However, this technology has the disadvantages of a large space demand, a complex process handling, and tanks requiring expensive corrosion resistant materials, cf. [50, 103]. For another, to increase the solar share in domestic applications, solar thermal or photovoltaic installations need to be combined with suitable storage technologies, cf. [11, 12, 47]. For daily domestic demand, solid SHS, with embedded heat exchangers through which the heat transfer medium is flowing, is considered as an effective and economical solution for limited space requirements and vessel costs combined with easy handling and the general advantages of SHS systems.

A novel mixed solid-liquid SHS is developed for environmentally neutral and economically viable solar collector-supplied energy storage system featuring a modular design for integration into heating systems of domestic or industrial buildings (Figure 1a). This solution is considered as an effective alternative to currently available SHS systems. A water-saturated cementitious material is fabricated as the storage medium, combined with easily available piping equipment for helically arranged heat exchangers. In comparison with the normal treated cementitious composites, it has a significantly increased storage capacity associated with energy density achievable, see Figure 3. Three heat exchanger candidates: aluminium alloys (AA), high-density polyethylene (PEHD), aluminium-polyethylene (AA-PE) composite are selected as feasible options for domestic solar TES in terms of performance, investment and maintenance costs. The specified charging temperature for this SHS module is 90 °C.



(a) A IGLU SHS prototype.



(b) Energy storage density.

Figure 3: (a) A single configured testing module. Images photographed by Mr M.Sc. Johannes Nordbeck, Department of Geosciences, Kiel University, johannes.nordbeck@ifg.uni-kiel.de. Material properties of the storage material are measured by Prof. Frank Wuttke's group, Chair of Geomechanics & Geotechnics, Kiel University, www.geotechnics.ifg.uni-kiel.de. (b) Energy capacity with different temperature lifts.

2.1 THERMO-HYDRO-MECHANICAL ANALYSIS OF A TESTING MODULE FOR SYSTEM DEVELOPMENT

To quantify the spatial distribution of stresses caused by incompatible thermal strains originating from temperature gradients or jumps in material properties, a numerical simulation in the framework of coupled THM processes is employed, covering two aspects: (i) a thermo-hydro-mechanical analysis to locate potentially critical regions in terms of the mechanical response of a lab-scale testing set-up representative of a typical storage module. The results will form the basis for more detailed analyses of thermo-mechanical (TM) processes presented in later chapters; (ii) a thermo-hydro-mechanical analysis explicitly quantifying the effects of fluid pressure under drained and undrained conditions. This effort aims to answer the question whether the porous solid storage medium experiences excessive tensile stresses due to the thermal expansion of the water inside its pores or whether fluid pressures can dissipate quickly enough in relation to heat transport.

The governing equations with respect to coupled THM processes relevant in the present context are written as follows:

(i) The mass(volume) balance of the fluid-saturated porous medium

$$\operatorname{div} [(\mathbf{u}_S)'_S + \phi_F \mathbf{w}_{FS}] = \beta_{\text{Teff}} \vartheta'_S + \phi_F \beta_{TF} \operatorname{grad} \vartheta \cdot \mathbf{w}_{FS} \quad (1)$$

with

$$\phi_F \mathbf{w}_{FS} = -\frac{\kappa_F}{\mu_{FR}} (\operatorname{grad} p - \rho_{FR} \mathbf{g}) \quad (2)$$

and

$$\beta_{\text{Teff}} = \phi_S \beta_{TS} + \phi_F \beta_{TF} \quad (3)$$

(ii) The momentum balance of the fluid-saturated porous medium

$$\operatorname{div} \left(\sigma_S^E - p\mathbf{I} \right) + \rho_{\text{eff}}\mathbf{g} = \mathbf{0} \quad (4)$$

with the effective stresses σ_S^E and thermal strains ϵ_{th} given as

$$\sigma_S^E = \mathbf{C} : (\epsilon - \epsilon_{\text{th}}) \quad (5)$$

and

$$\epsilon_{\text{th}} = \alpha_{\text{TS}} \Delta \vartheta \quad (6)$$

(iii) The energy balance of the fluid-saturated porous medium

$$(\rho c_p)_{\text{eff}} \vartheta'_S + \phi_F \rho_{\text{FR}} c_{\text{pF}} \operatorname{grad} \vartheta \cdot \mathbf{w}_{\text{FS}} - \operatorname{div} (\lambda_{\text{eff}} \operatorname{grad} \vartheta) = 0 \quad (7)$$

with

$$(\rho c_p)_{\text{eff}} = \phi_S \rho_{\text{SR}} c_{\text{pS}} + \phi_F \rho_{\text{FR}} c_{\text{pF}} \quad (8)$$

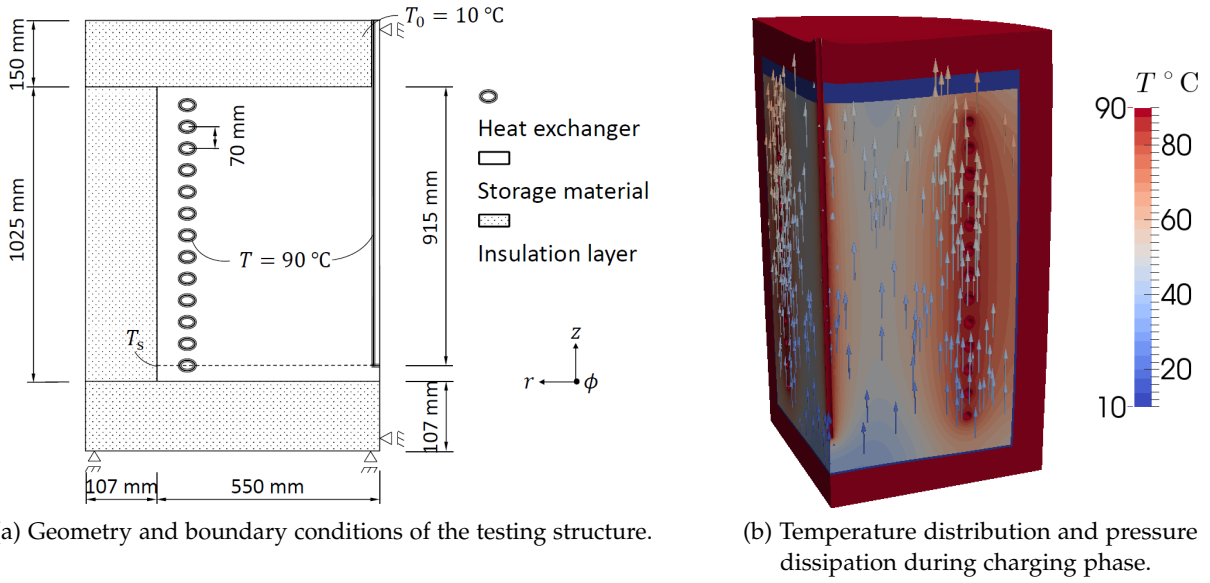
and

$$\lambda_{\text{eff}} = \phi_S \lambda_S + \phi_F \lambda_F \quad (9)$$

The governing equations are solved for the primary unknowns, the temperature, pressure, and displacement. A brief derivation of the governing equations is written in Appendix 2.1. The detailed description can refer [23] and [29].

An axisymmetric computational model (Figure 4a) is set up in the open-source finite element code OpenGeoSys [66, 67]. The detailed settings for the numerical computations, as well as material and geometrical properties of the storage medium and the heat exchangers, are described in Appendix 2.2. Figure 4b shows a snapshot of the heating process over the entire domain, in which the temperature distribution and the fluid flux $\phi_F \mathbf{w}_{\text{FS}}$ driven by the pressure gradient are demonstrated.

As the designed cementitious storage material is saturated with water to increase its heat storage capacity, the material permeability will largely determine the occurrence of critical pore pressures. They in turn can cause tensile effective stresses which potentially exceed the tensile strength of the material. Hence, pore water pressures and critical stresses in the system during the heating process are quantified based on the THM properties of the storage medium and the heat exchangers.



(a) Geometry and boundary conditions of the testing structure.

(b) Temperature distribution and pressure dissipation during charging phase.

Figure 4: (a) Settings of the lab-scale heat storage module in cross section; (b) Charging phase in an axisymmetric FEM model.

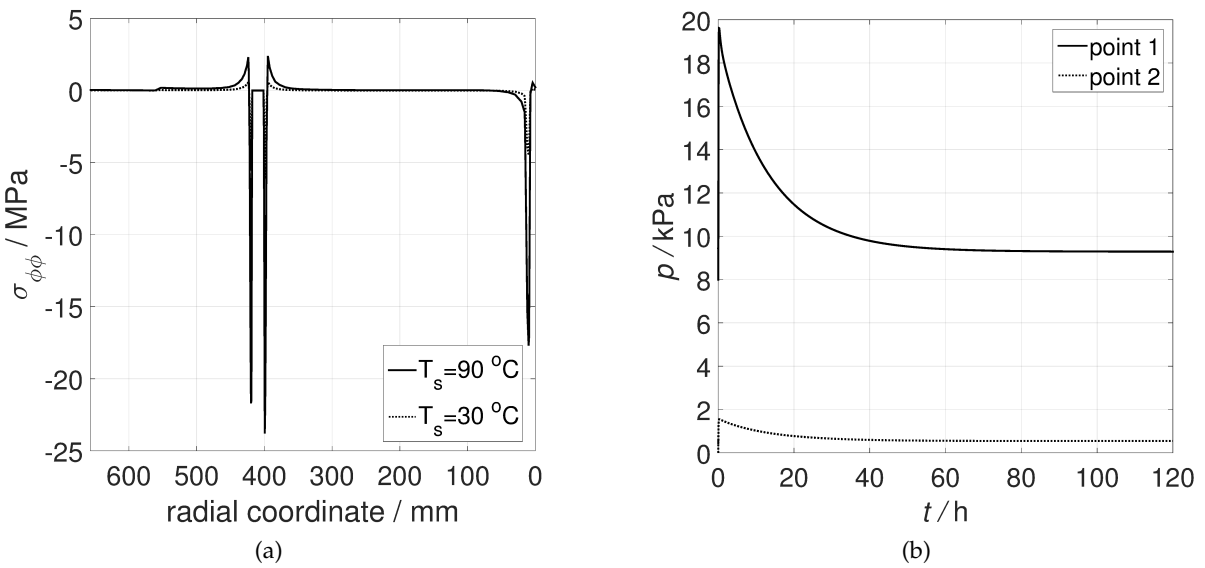


Figure 5: (a) Circumferential stress along the dashed radial line traversing the testing structure as indicated in Figure 4a. The stress profiles under two levels of the charging temperature clearly identify the heat exchanger-storage material interface as the main region of interest. (b) Variation of the fluid pressurisation during the charging period at two different locations (upper and lower, respectively) in the test structure.

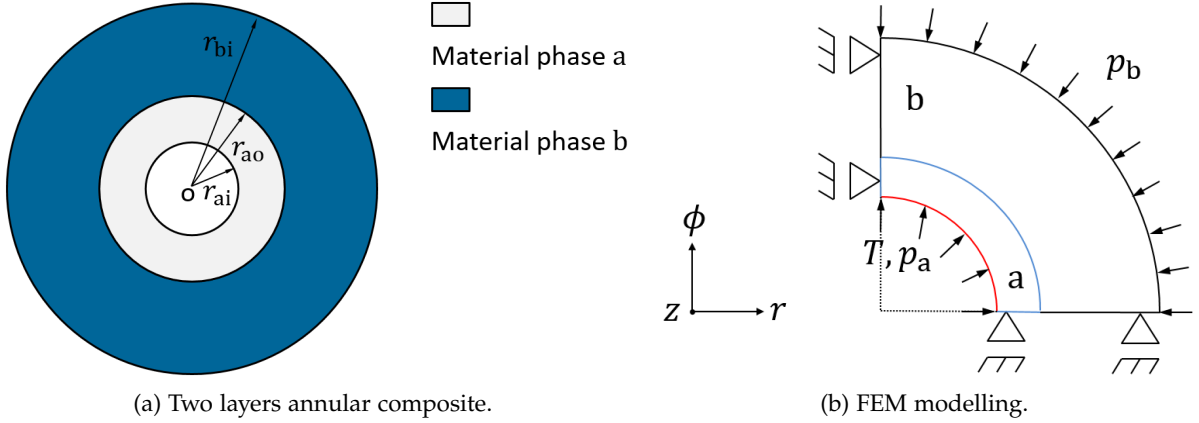


Figure 6: Schematic view and boundary conditions of a plane region characterising the vicinity of the heat exchanger. (a) Model assumption for analytical derivation; (b) Boundary conditions imposed onto the model domain.

Judging by the stress distribution plotted in Figure 5a, the region surrounding the heat exchanger can be identified as the critical region with the highest significance, see Figure 6a. The stresses caused by the presence of the heat exchangers far exceed those caused by internal fluid pressurisation. Since these stresses are characterised by very high gradients that require an exceedingly fine discretisation, the near field around the heat exchangers is studied separately and then numerical approach complemented by an analytical investigation. An analytical solution in cylindrical coordinates (Figure 6) from a thermo-mechanical perspective (Eq. (10) – Eq. (12)) is derived for the indicated critical region to examine the mechanical behaviour of the comprised solid storage medium and the heat exchanger. The derived analytical solution allows an efficient screening to the relevant material and geometrical quantities to identify their significances to the critical stresses. A detailed study of this part will be performed in Chapter 3. The mechanical model is depicted in Figure 6b with axisymmetric assumption to the boundaries.

$$\sigma_{rr}^i = \frac{A_i}{r^2} + 2C_i \quad (10)$$

$$\sigma_{\phi\phi}^i = -\frac{A_i}{r^2} + 2C_i \quad (11)$$

$$\sigma_{zz}^i = 4\bar{\nu}_i C_i - \bar{E}_i \bar{\alpha}_i \vartheta_i \quad (\text{plane strain}) \quad (12)$$

The integration constants $A_i(\bar{E}_i, \bar{\nu}_i, r_{io}, r_{ii}, p_i)$ and $C_i(\bar{E}_i, \bar{\nu}_i, r_{io}, r_{ii}, p_i)$ that combine the external loadings applied to the model, the relevant material and geometrical quantities of material components are stated in Appendix 2.2: Eq. (57) – Eq. (61).

Note that to what degree such stresses develop in the actual equipment depends both on interface friction and on the integration of the pipes in the overall set-up. Often, this stress will be relieved by intentionally creating a gap or a cushion between the heat exchanger and the storage material as tested by [102]. This issue is discussed in Appendix 2.2.

The boundary conditions assigned to the fluid domain determine the transport behaviour of the fluid through the porous storage medium. In the high-permeability case and under free-draining boundary conditions, no fluid pressurisation will occur. In the opposite extreme

case, the fluid cannot escape from the porous domain through any of its boundaries, thereby causing very high fluid pressures as a consequence of the high bulk modulus of most liquids. This extreme case can be described by an analytical solution for the fluid pressure created by the thermally induced volume expansion in a porous medium and serves as an upper bound for the numerical solutions.

The effective volumetric coefficient of thermal expansion from Eq. (3) is the basis for calculating the volumetric strain of the mixture

$$e_m = \beta_{\text{Teff}} \Delta\vartheta \quad (13)$$

Under externally load-free conditions, the fluid pressure is balanced only by effective stresses. Thus one finds

$$p = -K_S (e_m - e_{\text{th}}) = -K_S \phi_F (\beta_{\text{TF}} - \beta_{\text{TS}}) \Delta\vartheta \quad (14)$$

with

$$e_{\text{th}} = \beta_{\text{TS}} \Delta\vartheta \quad (15)$$

The fluid phase in the model is considered as water, with the volumetric coefficient of thermal expansion of $2.07 \times 10^{-4} \text{ K}^{-1}$.

Under undrained conditions, a freely expanding material undergoing a temperature increase by 80 K reaches a fluid pressure of 7.33 MPa. This pressure is balanced by tensile normal stresses of equal magnitude which exceeds typical tensile strength values of cementitious materials by far. This result illustrates that fluid pressurisation manifesting itself as tension in the solid skeleton has the potential to cause microcracks throughout the heated domain if the fluid cannot migrate out of the high-pressure zones quickly enough. It represents a potentially damaging effect in addition to the phenomena caused by the heat exchangers. The estimation based on Eq. (14) is an absolute upper bound which will be lowered not only by fluid migration ($\kappa_F > 0$) out of heated domains but also by a Biot coefficient lower than 1.

A quantitative estimation of fluid pressurisation under drained conditions representing the test module is achieved through numerical simulation. During the heating process, the fluid expands, locally causes pressure increases and exudes through the draining boundary at the top of the domain driven by pressure gradients, see Figure 4b. Two locations, one (point 1) towards the bottom of the testing structure and one (point 2) near the top, are selected to highlight the pressure transients during the charging period. It can be seen (Figure 5b) that the peak pressure arises during the initial stage of the heating process and drops off to a lower level as fluid is moved and eventually lost from the testing structure. Once the entire structure is heated up, fluid pressurisation has returned to levels very close to the original stratification (Appendix 2.2: Figure 6).

2.2 CONCLUSION

The THM numerical analysis reveals that hydraulically induced stresses are subcritical under drained conditions. Heat exchangers are identified as crucial elements for optimisation of a TES from a mechanical perspective. Because the fluid pressurisation is demonstrated not a critical field, more detailed analysis can proceed thermo-mechanically. In the framework

of linear thermo-elasticity, analytical solution is a powerful and versatile tool to study the dependence of stresses on materials properties and dimensions in a TES structure.

THERMO-MECHANICAL ANALYSIS OF HEAT EXCHANGER DESIGN FOR SOLID THERMAL ENERGY STORAGE SYSTEMS

In Chapter 2, the stress and fluid pressure states of a designed testing model for the IGLU solid-liquid SHS are examined through numerical simulations and analytical calculations. Results indicate that the heat exchangers play an important role not only in heat transfer, but also the thermo-mechanical and thermo-hydraulic performance of the surrounding storage medium. High tensile stresses in the near field of heat exchangers are observed (Chapter 2), implying a potentially functional unreliability of the designated TES system.

The multi-dimensional design of heat exchangers entails geometrical quantities, material pairings, the structural or spatial configuration, surface modifications, etc., cf. [100], all in the light of thermodynamic performance, thermo-mechanical and thermo-hydraulic integrity, cost, and other indicators. Currently, maximum thermal efficiency along with overall cost reduction is taken as the main and often the only optimisation objective [2, 9, 13, 25, 33, 37, 48, 62, 64, 78, 79, 97, 108, 112, 121].

As outlined in Chapter 2, the maximum tensile stress typically occurs within the storage material in the circumferential direction at the interface. As the maximum tensile stress is the most critical stress for commonly used brittle storage media such as cementitious or ceramic composites, it will be referred to as critical stress here for brevity. The stress fields within the cast SHS block around the heat exchangers, however, cannot be readily measured and only indirect experimental evidence on their effects is available [102]. Thus, it is the aim of this chapter to develop a theoretical model for the quantification of the mechanical behaviour in a two-phase annular structure. In this chapter, the study to heat exchangers focuses on improving the thermo-mechanical integrity of solid SHS structures, quantifying the dependence of significant stresses on key parameters of the heat exchanger and the storage material, and using that information for design optimisation. Specifically, the maximum tensile stresses around tubular heat exchangers embedded in a solid heat storage medium are quantified as an indicator for potential structural damage. As a further extension from Chapter 2, such thermally induced stress might quite possibly exceed the strength limits of the storage material for an inappropriate combination of geometrical sizes and material properties. The objective of the study in this chapter is twofold: (i) to examine the effects of geometrical/physical parameters of the heat exchanger to the mechanical performance of the solid SHS unit in detail by using the developed analytical approach; (ii) to show how this analytical approach can be modified and used to select a heat exchanger which is optimal from mechanical perspective and does not stand in contrast to thermodynamic requirements that are critical for the system's operation.

Generally, a designated solid SHS structure is characterised by the geometric layout of its heat exchangers as well as the selected storage material which must satisfy the thermal performance requirements as well as provide mechanical reliability. Particularly, the incompatibility of the heat exchanger with the storage material in terms of material properties dominates the stresses induced by thermal loadings.

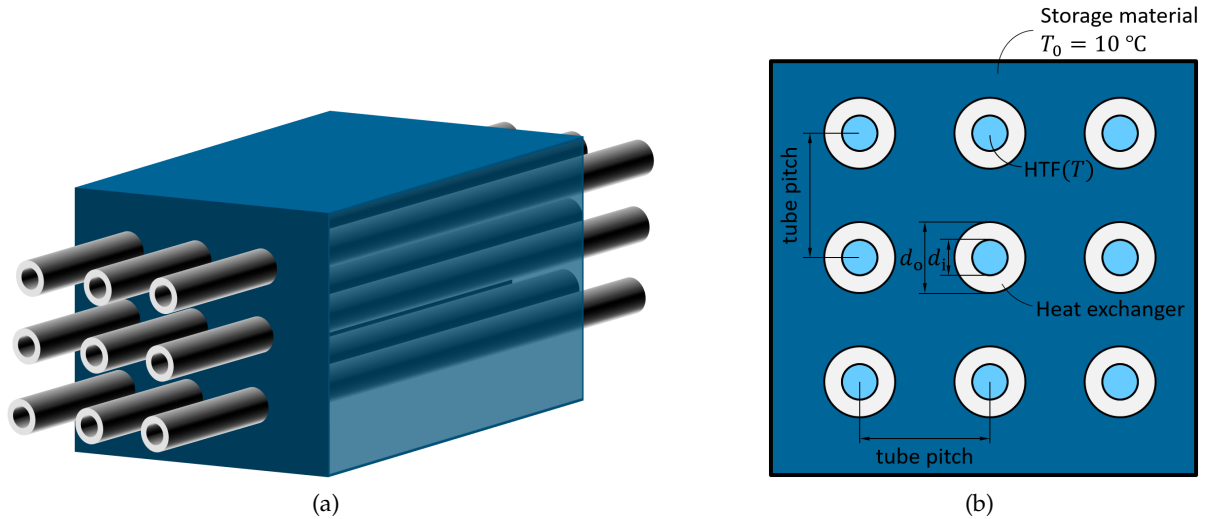


Figure 7: Schematic (a) and details (b) of standard tubular heat exchanger's geometric layout in a solid TES system. Note that in practical application, heat exchanger bundles are incorporated in such SHS module, and the number of the used pipes depends on the design power of a designated TES system.

The heat exchanger layout implemented in this study is based on a testing storage units of WESPE project [71, 72, 73, 105] and is illustrated in Figure 7a. To maintain a specific link to an ongoing project and to practically relevant parameter values, the baseline system parameters are set to values employed in the IGLU project (see Chapter 2). According to the results analysis presented in Appendix 2.2 of Chapter 2, and based on discussions on the available options with the design engineers, three quantities are considered as the main geometric design parameters in this study: the outer and inner diameters of the heat exchanger, and the tube pitch S which is defined as the centre-to-centre distance between two adjacent cylindrical heat exchangers, see Figure 7b. The above configuration aside, the proposed approach can apply to other configurations composed of piping bundles embedded within a solid storage medium as well, cf. [3, 59, 95, 114].

3.1 CHARACTERISATION OF PHYSICAL QUANTITIES ON THE MECHANICAL BEHAVIOUR OF SOLID THERMAL ENERGY STORAGE

The dependence of maximum stresses on the multiple parameters provides flexibility regarding possible technical solutions combining storage materials and heat exchangers in agreement with specific design requirements of a solid TES system. To simplify the analysis, all variables influencing the critical tensile stress are condensed into dimensionless quantities, and the assumptions made to arrive at an analytical solution can be found in Appendix 2.3. The derived analytical formulation is performed for the optimisation of the heat exchanger's layout from a mechanical perspective. In this respect, the sensitivity of the critical stress to

each parameter (see Appendix 2.3: Eq. (B.3) – Eq. (B.11)) can serve as a guide-line for the design of the tube-type solid TES. The sensitivities along with all their parameter and state dependencies can of course also be derived analytically.

A monotonic decrease of the maximum tensile stress (the stress field in the storage medium at the interface, see Figure 5a) is observed with the increase of the tube pitch in Figure 8. A dramatic impact of the scale of the tube pitch to the decrease of the stress arises in the initial increase of the tube pitch. Then the reducing rate of the stress decreases quickly with the further increase of the tube pitch, and asymptotically, a minimal stress can be obtained. To define an optimal value, the lowest achievable maximum/critical stress σ_{mp} is defined based on a threshold criterion as that stress where $|D_S| \leq \zeta$ (see Figure 8). In this study, D_S represents the gradient of the critical stress σ_{mp} with respect to the tube pitch S

$$D_S = \left. \frac{\partial \sigma_{mp}}{\partial S} \right|_{\text{interface}} \quad (16)$$

Simultaneously, this defines the optimal tube pitch that minimises the maximum stress. $\zeta = 0.01$ is used as a unilateral compromise on the thermal performance of the IGLU SHS. Because an engineered TES module requires an adequately tight packing of heat exchangers to achieve a high thermal power while maintaining high thermal capacity, evoking an optimum balance postulation, i.e. a compromise between a maximum spacing allowed from a thermal perspective and a minimum spacing required from a mechanical perspective. Both measures can be combined into an objective function for a comprehensive optimisation scheme. In this chapter, the focus is exclusively on the mechanical contribution.

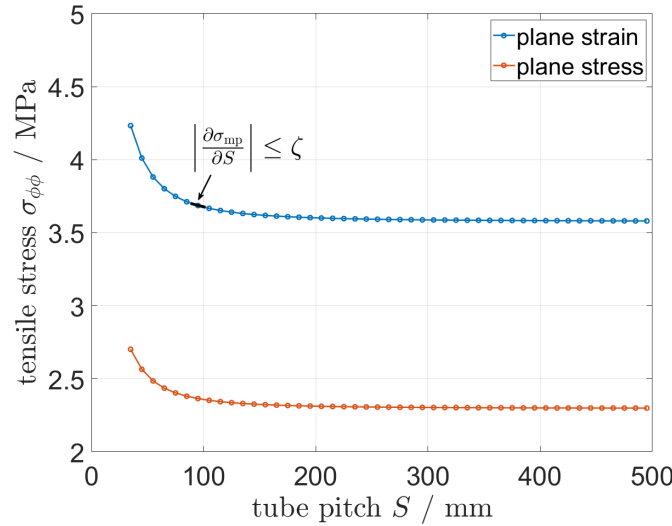


Figure 8: Maximum tensile stress varying with the tube pitch.

The first-order partial derivatives of the objective stress (the calculation equation of this stress is formulated in Eq. (11)) with regards to the specified parameters (Young's modulus, Poisson's ratio, thermal expansion coefficient, tube dimensions, tube pitch) are derived to describe the sensitivities of different quantities affecting the stress response, see Eq. (16) as an example.

As observed in Figure 9, extending the tube pitch can reduce the maximum tensile stress up to a threshold value of the tube pitch, beyond which the sensitivity is practically zero,

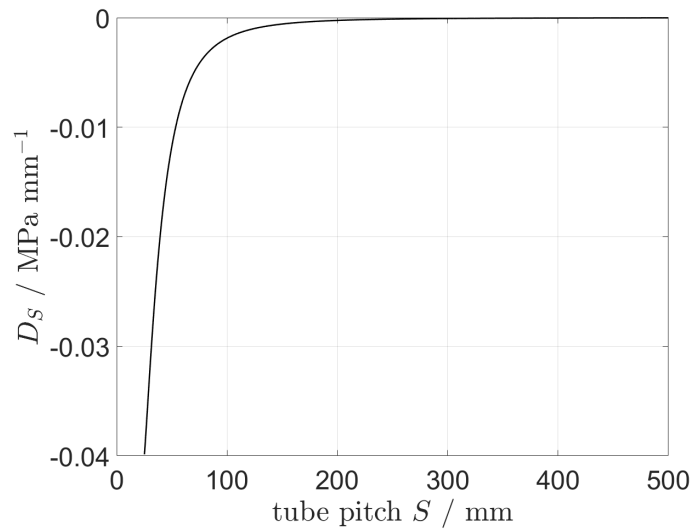


Figure 9: Sensitivity of the objective tensile stress with regards to the tube pitch.

i.e. a further increase in tube pitch has a negligible impact, which is consistent with the observation in Figure 8. The sensitivities to changes in other specific parameters can be found in Appendix 2.3, where a specific case study of solid SHS is demonstrated to show how to practically screen an optimal combination of dimensions and material properties to avoid potentially structural damage and provide required thermal performance characteristics.

3.2 CONCLUSION

The TM analytical analysis demonstrates that even under specified design constraints to a developing TES, e.g. fixed materials or dimensions of components, minimising the critical stress to reduce the risk of damaging in the solid storage medium can still be achieved by adjusting other related quantities based on the calculated sensitivities. Young's modulus and Poisson's ratio of the storage medium, dimensions of the heat exchanger have strong influence to the behaviour of objective stress, see Appendix 2.3: Figure B.4 – Figure B.5.

Part II

PHASE-FIELD APPROACH FOR CHARACTERISATION OF
FRACTURING IN SOLID THERMAL ENERGY STORAGE

The detailed study of this part is included in:

X.-Y. Miao, O. Kolditz, T. Nagel, Phase-field modeling of fracture in poroelastic solids for thermal energy storage. *Poromechanics VI: Proceedings of the Sixth Biot Conference on Poromechanics*, Paris, France, July 9-13, 2017, Pages 1976-1983.

X.-Y. Miao, T. Zheng, O. Kolditz, T. Nagel, Phase-field modeling of cracking processes in geomaterials for subsurface geotechnical engineering and energy storage. *Advance of Computer Methods in Geomechanics: Proceedings of the fifteenth International Conference of the International Association for Computer Methods and Advanced in Geomechanics*, Wuhan, China, October 19-23, 2017, accepted.

X.-Y. Miao, O. Kolditz, T. Nagel, Modelling thermal performance degradation of high and low-temperature solid thermal energy storage due to cracking processes using a phase-field approach. *Energy Conversion and Management*, Volume 180, January 2019, Pages 977-989.

PHASE-FIELD APPROACH FOR THE IDENTIFICATION OF
THERMO-MECHANICAL FRACTURING IN SOLID THERMAL ENERGY
STORAGE

Through Chapter 2 and Chapter 3, a comprehensive THM quantification study for hypothetically intact solid SHS structure has been achieved to elucidate areas likely prone to damage. This chapter goes one step further, in that a phase-field model for brittle fracturing [20, 32, 41, 51, 83, 85, 86, 87, 88, 107, 111, 113] is proposed to address the probable cracking progression in solid SHS structures, and determine how the thermal performance characteristics are affected due to the presence of open fractures.

Fracture mechanical simulations require sophisticated numerical tools due to the development of discontinuities along paths not known a priori. Phase-field modelling is a in continuum mechanical approach to fracture mechanics [55, 84, 89]. It can be implemented based on variational principles of brittle fracture [10, 45, 56] based in turn on energy minimisation [40]. Phase-field modelling in fracture mechanics has a number of attractive features [6, 7, 34, 65]. The principal highlight of this approach is that it smears the discontinuous crack by introducing a phase-indicator variable that smoothly transitions between the undamaged material phase and the crack domain, so that the crack can be described from a continuous configurational perspective [17, 18, 99, 120].

4.1 MODEL FORMULATION FOR BRITTLE FRACTURE IN THERMO-ELASTIC SOLIDS

4.1.1 *The concept of a diffusive crack*

Comparing to the modelling of a sharp (discontinuous) crack interface, a diffusive crack is defined in a continuous framework. In such a continuous setting, a varying phase-field variable (order parameter) d is introduced (see Fig. 10), and the regularised crack surface functional can be written as a volume integral using the crack-surface density γ as, cf. [19, 20, 40, 89]

$$\Gamma_\varepsilon(d) = \int_\Omega \gamma dV = \int_\Omega \left[\frac{1}{4\varepsilon} (1-d)^2 + \varepsilon \text{grad}d \cdot \text{grad}d \right] dV \quad (17)$$

4.1.2 *Constitutive equations of thermo-elasticity in thermodynamics*

The derivation of governing equations for phase-field modelling of fracture can be performed from various considerations including variational settings, irreversible thermodynamics, geometrical arguments, and configurational mechanics, respectively, cf. [32, 69, 89]. Under

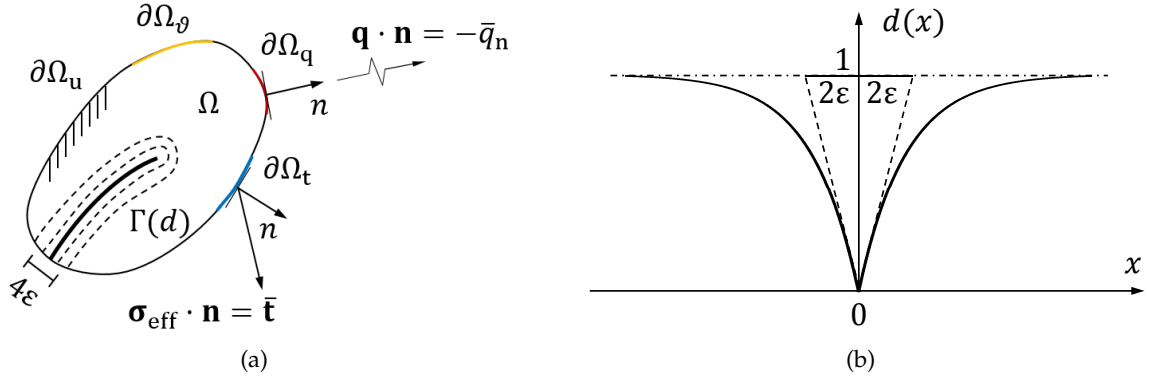


Figure 10: (a) A diffusive crack expression in an elastic body with a bidirectional smoothing path over a length-scale 2ϵ through $\Gamma(d)$. Here $\Omega \subset \mathcal{R}^D$, $D \in [2, 3]$ be a reference configuration of a material body and $\partial\Omega \subset \mathcal{R}^{D-1}$ its external boundary with $\partial\Omega_u \cup \partial\Omega_t = \partial\Omega$ and $\partial\Omega_\theta \cup \partial\Omega_q = \partial\Omega$, and with $\partial\Omega_u \cap \partial\Omega_t = \emptyset$ and $\partial\Omega_\theta \cap \partial\Omega_q = \emptyset$. (b) Schematic of the diffusive crack's exponential profile in 1D, characterised by a length-scale parameter 2ϵ , physical association with the characteristic length of material, cf. [34, 99, 107].

certain assumptions, all the three approaches lead to identical thermodynamically consistent results but highlight different conceptual perspectives. In this contribution, the constitutive equations of mechanical phase-field modelling coupled to heat transport (Fig. 10a) are derived from a thermodynamic perspective, whereas the more detailed derivation aspects from these three approaches are stated in Appendix 2.4.

The Clausius-Duhem inequality is first formulated, cf. [87] based on the first and second laws of thermodynamics

$$\begin{aligned} & \left(\sigma - \varrho \frac{\partial \bar{\psi}}{\partial \epsilon} \right) : \dot{\epsilon} - \varrho \left[\frac{\partial \bar{\psi}}{\partial d} - \text{div} \left(\frac{\partial \bar{\psi}}{\partial \text{grad} d} \right) \right] \dot{d} - \varrho \text{div} \left(\frac{\partial \bar{\psi}}{\partial \text{grad} d} \dot{d} \right) \\ & - \varrho \left(\eta + \frac{\partial \bar{\psi}}{\partial \theta} \right) \dot{\theta} - \varrho \frac{\partial \bar{\psi}}{\partial \text{grad} \theta} \cdot \text{grad} \dot{\theta} - \frac{1}{\theta} \mathbf{q} \cdot \text{grad} \theta \geq 0 \end{aligned} \quad (18)$$

where a specific Helmholtz free energy: $\bar{\psi}(\epsilon, d, \text{grad} d, \theta, \text{grad} \theta)$ is postulated for phase-field treatment.

The equilibrium formulation associated with mechanical, phase-field, and heat conduction arguments can be respectively derived from Eq. (18) yielding, for example, the following relations valid on Ω

$$\sigma = \varrho \frac{\partial \bar{\psi}}{\partial \epsilon} \quad (19)$$

$$\frac{\partial \bar{\psi}}{\partial d} - \text{div} \left(\frac{\partial \bar{\psi}}{\partial \text{grad} d} \right) = 0 \quad (20)$$

$$(\varrho c_p)_{\text{eff}} \frac{\partial \theta}{\partial t} - \text{div} (\lambda_{\text{eff}} \text{grad} \theta) = 0 \quad (21)$$

where additionally the momentum balance and energy balance have been used. The Helmholtz free energy density of a thermo-elastic solid can be given as the sum of mechanical, thermal and regularised surface-energy contribution

$$\psi(\epsilon, \vartheta) = \psi_m(\epsilon_{el}) + \psi_{th}(\vartheta) + \psi_{surf}(\gamma) \quad (22)$$

4.1.3 Degradation of elastic energy and heat conduction

The presence of new surface-energy (phase-field), thermal processes, and pore fluid phases bestows interactive effects to the system. Specifically, the presence of open fractures in the material body will lead to a degradation of elastic strain energy, cf. [8, 19, 32, 42, 65, 89], and the fluid medium contained in these fractures will affect the thermal properties, cf. [69, 87]. As a consequence, in a fractured body, an approximation of the Helmholtz free energy density can be formulated as, cf. [31]

$$\begin{aligned} \rho \bar{\psi}(\epsilon, d, \text{gradd}, \vartheta) = & (d^2 + k) \psi_{m0}^+(\epsilon, \vartheta) + G_c \left[\frac{1}{4\epsilon} (1-d)^2 + \epsilon \text{gradd} \cdot \text{gradd} \right] + \psi_{m0}^-(\epsilon, \vartheta) \\ & - (\rho c_p)_{\text{eff}} \left(\vartheta \ln \frac{\vartheta}{\vartheta_0} - \vartheta + \vartheta_0 \right) \end{aligned} \quad (23)$$

The thermal conductivity variation taking into account the changes due to open fluid-filled fractures is modelled here as

$$\mathbf{q} = - \left\{ \langle \text{tr}(\epsilon_{el}) \rangle_+ \left[(d^2 - 1) \lambda_S + (1-d)^2 \lambda_d \right] + \lambda_S \right\} \text{grad} \vartheta \quad (24)$$

The 'open' crack which degrades the mechanical and thermal functions of material body is identified by a positive volumetric elastic strain, see Eq. (23) and Eq. (24).

The numerical realisation of the continuum-mechanical phase-field model in OGS, as well as a series of tests for model verification, can be found in Appendices 2.4, 2.5, and 2.6. The source code is freely available at <https://github.com/ufz/ogs/tree/master/ProcessLib/ThermoMechanicalPhaseField>.

4.2 THERMAL FRACTURING IN SOLID SENSIBLE HEAT STORAGE

In this section, the thermal cracking processes are explored in two representative solid SHS units with low (90 °C) and high (390 °C) charging temperature, respectively. To achieve the expected functional performance, different material components (pore/crack-filling fluid) and heat exchanger configurations are designed for the two modules. As stated in Eq. (23) and Eq. (24), the charging temperature determines the driven force of cracking, the thermal attenuation of a TES depends on the thermal conductivity of the fluid phase. As the different materials, fluid media, and charging temperatures are utilised in the two modules, different structural damages and attenuations of the heat transfer performance are expected to be characterised or quantified in the following calculations.

The computational models applied in numerical simulations for capturing the paths of crack evolution are displayed in Figure 11. More detailed computational settings including solution strategy, element properties, simulation scenarios are presented in Appendix 2.6.

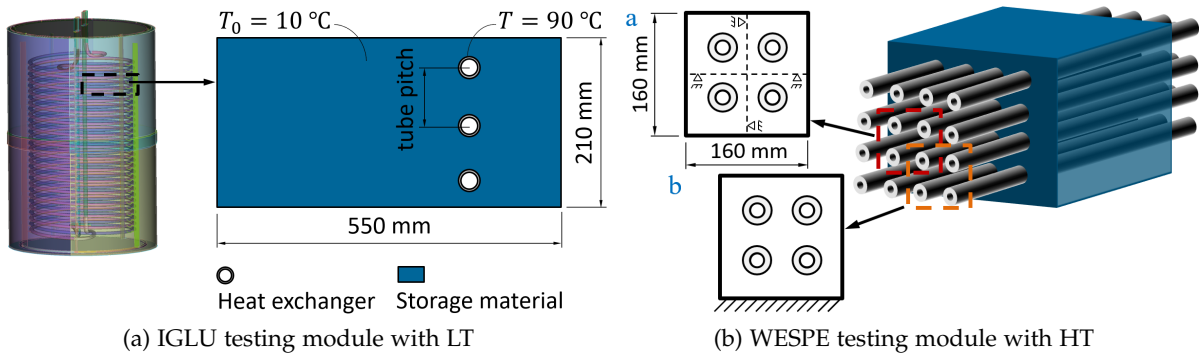


Figure 11: Axisymmetric model (a) and reference plane-strain models (b) extracted from respective single SHS module. The designed models in (b) cover four heat exchanger pipes with arrangement in a 2×2 configuration.

Fracture patterns observed in different sample models are demonstrated in Figure 12. Tangential cracks are initiated and driven by the incompatible thermal strains and the resulting tensile stresses in the circumferential direction that have been quantified in Chapter 2 and Chapter 3. The initial cracks develop along the material interface between the storage medium and heat exchangers, indicating potential breakage of the storage body, and in consequence, both the mechanical and thermal properties of the SHS will degrade. The nature of cracking highly depends on the stress induced by the mismatched thermal expansion between the two components and the response from the matrix boundaries, eventually leading to different fracture patterns.

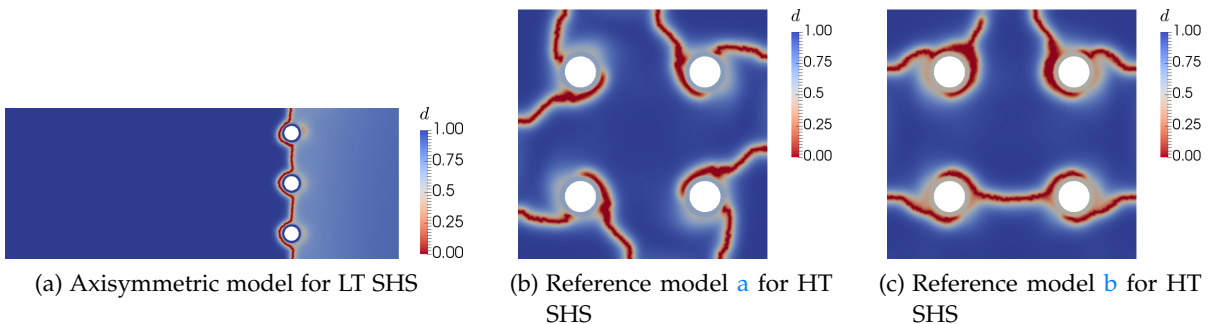


Figure 12: Cracking evolutions within the storage body in LT axisymmetry (a), HT model a (b), and HT model b (c).

Figure 13 – Figure 14 highlight the discrepancies of thermal performance between the assumed intact and actual fractured solid SHSs during subsequent heating cycles when distinct damaged zones (Figure 12) have been formed under the preceding heating processes. Particularly, heating power profiles of the two cases plotted in Figure 13 underline the performance loss because of fracturing. The loss levels of thermal performance depend on the type of filled fluid phases, as well as the input temperatures.

In principle, the developed cracks form a fluid-filled (usually water or air) space between the remaining storage body of two sides, which behaves as a barrier to heat transfer in the

storage body because of its relatively low thermal conductivity in the case of air, leading to high temperature gradients in the damaged regions, see Figure 14.

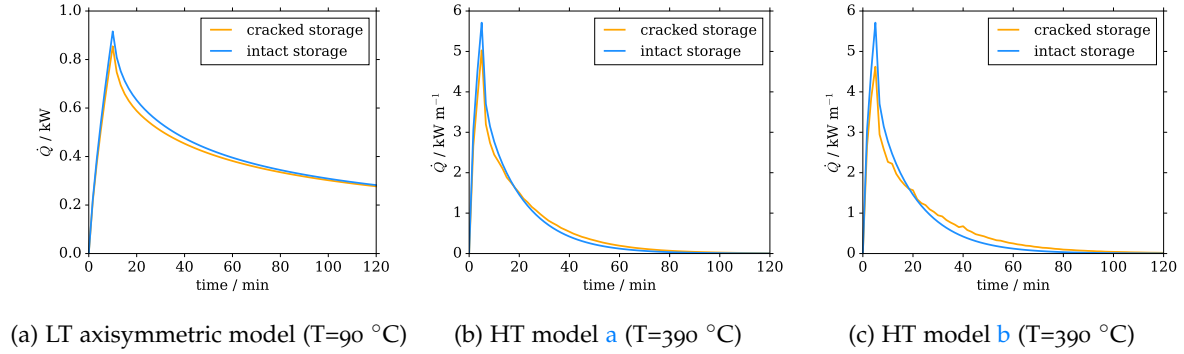


Figure 13: Heating power profiles of the intact and cracked SHS body over a heating period. The fluid medium filled in (a) is water, and in (b) and (c) is air.

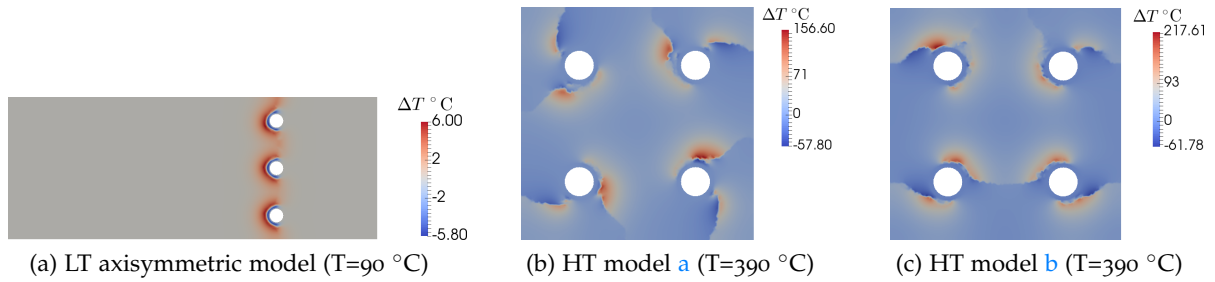


Figure 14: Temperature difference ($\Delta T = T_{\text{intact}} - T_{\text{damaged}}$) between the intact and cracked SHS body corresponding to the highest power difference over a charging phase.

4.3 CONCLUSION AND DISCUSSION

The TM fracturing analysis demonstrates that incompatible thermal deformation induced by temperature gradient during charging process of a solid TES can cause fractures in storage medium. Fluid phase filled in open fractures with relatively lower thermal conductivity results in greater thermal degradation of the fracturing material. Higher charging temperature induces larger thermal deformation, leading to more severe damage in the storage medium.

In the present study, the indispensable open fractures for heat transfer degradation are determined by volumetric expansion, see Eq. (24). However, the shear strain energy might also create open fractures. Thus using positive principal strains can be a more accurate judgement of the open fracture, which will be one of the future extensions of this model.

SUMMARY AND OUTLOOK

5.1 SUMMARY

The goal of this contribution is to study the coupled multiphysics processes in solid thermal energy storage (TES) with emphasis on mechanical damage and resulting thermal degradation. Multiphysics (thermo-(hydro-)mechanical (T(H)M)) modelling approach is presented starting from the analysis of a newly designed solid-fluid SHS system with a water-saturated cementitious storage medium. Because this contribution is intended to shed light on the mechanical behaviour of solid TES structures under multiphysics conditions, the focus is laid on the characterisation of critical stresses of the porous storage medium. Fluid pressure-driven forces are confirmed not a critical threat to this specific SHS. Thermally induced stresses behave in tension in storage medium around the heat exchanger, and exceed the tensile strength of the designed storage material, implying a fracturing potential in this region. Within this critical regions, an analytical solution of bimaterial system is derived in the framework of linear thermo-elasticity to perform more robust and extensive parametric analysis in relation to stress fields. More detailed description of the thermo-mechanically critical regions extends to more general solid TES configuration (TES with the integration of tubular heat exchangers), with taking into account material and geometric features. Optimal dimensions and spacing assignment of the heat exchangers for the purpose of minimising critical stresses of such TES structures are determined. To further identify the mechanical damage induced by critical stresses, quantify its extent and its impact, a continuum phase-field model of fracturing for the examination of brittle crack evolution in thermo-elastic solids under consideration of fluid phase in terms of effective properties is derived based on laws of thermodynamics. Fracturing induced by thermal-driven forces is found in two paradigmatic TES modules. The genesis and selective propagation of cracks driven by inherent material characteristics are qualitatively identified.

In particular, a Helmholtz free energy for a fractured body with the dependence of total strain, phase-field, and temperature is used, indicating three contributions from mechanics, surface-energy of fracturing, and heat conduction. The crack surface functional is written with regularisation treatment, presenting an exponential topology of the transition between damaged and intact material body. The constitutive equations are derived based on the Clausius-Duhem inequality. Dirichlet constraints to the phase-field argument are employed to ensure the irreversibility of fracturing process. The presence of fractures governs the effective thermal conductivity of the material body. Judging by the types of fluid media contained within the cracked volume (e.g. air, water), in general, the thermal performance of the damaged material will degrade. Herein, the heat conduction equation is modified with taking into

account the degradation of thermal conductivity within the cracked domain, as well as the recover once the crack is closed by external stimulations. This contribution demonstrates from a mechanical perspective the failure identification of solid TES structures by linking the thermal performance degradation to the progression of structural damage. The meaningful results and additional comparable tests prove the capability of the presented models in processing complex scenarios associated with multiphysics conditions.

5.2 OUTLOOK

In the present contribution, a numerical framework for phase-field formulation of fracturing in thermo-elastic solids is established. This feature outlines a powerful numerical orientation for the failure study in various applications subject to multiphysics processes. A phase-field model can be integrated with thermal, hydraulic, electric, and chemical processes to highlight different driven forces (e.g. temperature gradient [83, 87], fluid pressure [32, 85, 86], electric field [1, 88], crystallisation [91], chemical potential [82]) of fracturing. The corresponding constitutive equations can be derived from entropy inequality, among other approaches. An extension of the present phase-field model to thermo-hydraulic coupling could be achieved as the governing PDEs have been derived based on TPM in Appendix 2.4. In addition, the assumption of small deformations, isotropy, and brittle fracture might not be ensured in practical problems, the nonlinear, anisotropic, and inelastic features of solids should be also incorporated, cf. [7, 15, 16]. One challenge that hinders the extension development and application of phase-field formulation is the high computing consumption on account of the non-linear momentum balance equations that have to be solved, and the high level of mesh refinement. High-performance computing techniques are required for solving the discrete linearised system from multiphysics arguments and inherent high resolution. A higher computational power can be obtained from parallel computing techniques of employing multiple CPU cores ([68]). Particularly, multiscale finite element techniques can also reduce the computational efforts on the premise that cracking behaviour cannot be influenced by multiscale meshing treatment ([93]).

Furthermore, the utilisation of water-saturated cementitious material to enhance the heat capacity of storage medium opens a new design of using porous media for the development of economical and efficient solid-fluid TES. In this study, tubular heat exchangers with unique dimension are used in the discussed TES modules. A further extension on the configuration of heat exchangers can be the integration of mixed-dimension heat exchangers or non-tubular heat exchangers in solid TES systems to explore whether the thermal performance and the mechanical stability of such TES can be improved. A solid TES module is often exposed to a complex loading condition, the commercialisation of such TES technology puts forward high requirements on long-term efficiency and reliability of TES modules. Particularly, the reliability must be ensured over the expected operation life-time of TES units. From a mechanical perspective, cyclic fatigue effects can work on both the storage medium and the heat exchangers, and might cause fatigue failures in the two components. Thus life-time fatigue failures of metallic or non-metallic parts of a solid TES should be a further study to life assurance for such TES modules.

LIST OF FIGURES

Figure 1	Design and construction of solid TES systems for specific applications. (a) TES operating at low temperature for domestic applications. Due to the integration into the shallow subsurface, potential interactions with ground water need to be considered; (b) TES operating at high temperature for solar thermal power plants.	2
Figure 2	Thermal energy storage solutions based on different mechanisms.	2
Figure 3	(a) A single configured testing module. Images photographed by Mr M.Sc. Johannes Nordbeck, Department of Geosciences, Kiel University, johannes.nordbeck@ifg.uni-kiel.de . Material properties of the storage material are measured by Prof. Frank Wuttke's group, Chair of Geomechanics & Geotechnics, Kiel University, www.geotechnics.ifg.uni-kiel.de . (b) Energy capacity with different temperature lifts.	8
Figure 4	(a) Settings of the lab-scale heat storage module in cross section; (b) Charging phase in an axisymmetric FEM model.	10
Figure 5	(a) Circumferential stress along the dashed radial line traversing the testing structure as indicated in Figure 4a. The stress profiles under two levels of the charging temperature clearly identify the heat exchanger-storage material interface as the main region of interest. (b) Variation of the fluid pressurisation during the charging period at two different locations (upper and lower, respectively) in the test structure.	10
Figure 6	Schematic view and boundary conditions of a plane region characterising the vicinity of the heat exchanger. (a) Model assumption for analytical derivation; (b) Boundary conditions imposed onto the model domain.	11
Figure 7	Schematic (a) and details (b) of standard tubular heat exchanger's geometric layout in a solid TES system. Note that in practical application, heat exchanger bundles are incorporated in such SHS module, and the number of the used pipes depends on the design power of a designated TES system.	15
Figure 8	Maximum tensile stress varying with the tube pitch.	16
Figure 9	Sensitivity of the objective tensile stress with regards to the tube pitch.	17
Figure 10	(a) A diffusive crack expression in an elastic body with a bidirectional smoothing path over a length-scale 2ε through $\Gamma(d)$. Here $\Omega \subset \mathbb{R}^D$, $D \in [2, 3]$ be a reference configuration of a material body and $\partial\Omega \subset \mathbb{R}^{D-1}$ its external boundary with $\partial\Omega_u \cup \partial\Omega_t = \partial\Omega$ and $\partial\Omega_\theta \cup \partial\Omega_q = \partial\Omega$, and with $\partial\Omega_u \cap \partial\Omega_t = \emptyset$ and $\partial\Omega_\theta \cap \partial\Omega_q = \emptyset$. (b) Schematic of the diffusive crack's exponential profile in 1D, characterised by a length-scale parameter 2ε , physical association with the characteristic length of material, cf. [34, 99, 107].	21

Figure 11	Axisymmetric model (a) and reference plane-strain models (b) extracted from respective single SHS module. The designed models in (b) cover four heat exchanger pipes with arrangement in a 2×2 configuration.	23
Figure 12	Cracking evolutions within the storage body in LT axisymmetry (a), HT model a (b), and HT model b (c).	23
Figure 13	Heating power profiles of the intact and cracked SHS body over a heating period. The fluid medium filled in (a) is water, and in (b) and (c) is air.	24
Figure 14	Temperature difference ($\Delta T = T_{\text{intact}} - T_{\text{damaged}}$) between the intact and cracked SHS body corresponding to the highest power difference over a charging phase.	24
Figure 15	Rheological analogue of the LUBBY2 model.	38
Figure 16	Characteristic shape of the yield function and the plastic potential in the hydrostatic plane.	39

BIBLIOGRAPHY

- [1] Abdollahi, A., Arias, I., 2012. Phase-field modeling of crack propagation in piezoelectric and ferroelectric materials with different electromechanical crack conditions. *Journal of the Mechanics and Physics of Solids* 60 (12), 2100–2126.
- [2] Agyenim, F., Eames, P., Smyth, M., 2009. A comparison of heat transfer enhancement in a medium temperature thermal energy storage heat exchanger using fins. *Solar Energy* 83 (9), 1509–1520.
- [3] Agyenim, F., Eames, P., Smyth, M., 2010. Heat transfer enhancement in medium temperature thermal energy storage system using a multitube heat transfer array. *Renewable Energy* 35 (1), 198–207.
- [4] Agyenim, F., Hewitt, N., Eames, P., Smyth, M., 2010. A review of materials, heat transfer and phase change problem formulation for latent heat thermal energy storage systems (LHTESS). *Renewable and Sustainable Energy Reviews* 14 (2), 615–628.
- [5] Alonso, M., Vera-Agullo, J., Guerreiro, L., Flor-Laguna, V., Sanchez, M., Collares-Pereira, M., 2016. Calcium aluminate based cement for concrete to be used as thermal energy storage in solar thermal electricity plants. *Cement and Concrete Research* 82, 74–86.
- [6] Ambati, M., Gerasimov, T., De Lorenzis, L., 2015. A review on phase-field models of brittle fracture and a new fast hybrid formulation. *Computational Mechanics* 55 (2), 383–405.
- [7] Ambati, M., Kruse, R., De Lorenzis, L., 2016. A phase-field model for ductile fracture at finite strains and its experimental verification. *Computational Mechanics* 57 (1), 149–167.
- [8] Amor, H., Marigo, J.-J., Maurini, C., 2009. Regularized formulation of the variational brittle fracture with unilateral contact: numerical experiments. *Journal of the Mechanics and Physics of Solids* 57 (8), 1209–1229.
- [9] Azad, A. V., Amidpour, M., 2011. Economic optimization of shell and tube heat exchanger based on constructal theory. *Energy* 36 (2), 1087–1096.
- [10] Barenblatt, G. I., 1962. The mathematical theory of equilibrium cracks in brittle fracture. *Advances in Applied Mechanics* 7, 55–129.
- [11] Bauer, D., Marx, R., Nußbicker-Lux, J., Ochs, F., Drücker, H., Heidemann, W., 2013. Forschungsbericht zum BMU-Vorhaben Solarthermie2000plus: Wissenschaftlich-technische Begleitung des Förderprogramms Solarthermie2000plus zu solar unterstützter Nahwärme und Langzeit-Wärmespeicherung. Institut für Thermodynamik und Wärmetechnik, Univeisität Stuttgart.
- [12] Bauer, D., Marx, R., Nußbicker-Lux, J., Ochs, F., Heidemann, W., Müller-Steinhagen, H., 2010. German central solar heating plants with seasonal heat storage. *Solar Energy* 84 (4), 612–623.

-
- [13] Bergles, A. E., 2002. ExHFT for fourth generation heat transfer technology. *Experimental Thermal and Fluid Science* 26 (2), 335–344.
- [14] Bijarniya, J. P., Sudhakar, K., Baredar, P., 2016. Concentrated solar power technology in India: a review. *Renewable and Sustainable Energy Reviews* 63, 593–603.
- [15] Bleyer, J., Alessi, R., 2018. Phase-field modeling of anisotropic brittle fracture including several damage mechanisms. *Computer Methods in Applied Mechanics and Engineering* 336, 213–236.
- [16] Borden, M. J., Hughes, T. J., Landis, C. M., Anvari, A., Lee, I. J., 2016. A phase-field formulation for fracture in ductile materials: finite deformation balance law derivation, plastic degradation, and stress triaxiality effects. *Computer Methods in Applied Mechanics and Engineering* 312, 130–166.
- [17] Borden, M. J., Hughes, T. J., Landis, C. M., Verhoosel, C. V., 2014. A higher-order phase-field model for brittle fracture: formulation and analysis within the isogeometric analysis framework. *Computer Methods in Applied Mechanics and Engineering* 273, 100–118.
- [18] Borden, M. J., Verhoosel, C. V., Scott, M. A., Hughes, T. J., Landis, C. M., 2012. A phase-field description of dynamic brittle fracture. *Computer Methods in Applied Mechanics and Engineering* 217, 77–95.
- [19] Bourdin, B., Francfort, G. A., Marigo, J.-J., 2000. Numerical experiments in revisited brittle fracture. *Journal of the Mechanics and Physics of Solids* 48 (4), 797–826.
- [20] Bourdin, B., Francfort, G. A., Marigo, J.-J., 2008. The variational approach to fracture. *Journal of Elasticity* 91 (1-3), 5–148.
- [21] Cabeza, L. F., 2014. *Advances in thermal energy storage systems: methods and applications*. Elsevier.
- [22] Chu, S., Majumdar, A., 2012. Opportunities and challenges for a sustainable energy future. *Nature* 488 (7411), 294.
- [23] De Boer, R., 2006. *Trends in continuum mechanics of porous media*. Vol. 18. Springer Science & Business Media.
- [24] Dincer, I., Dost, S., Li, X., 1997. Performance analyses of sensible heat storage systems for thermal applications. *International Journal of Energy Research* 21 (12), 1157–1171.
- [25] Dizaji, H. S., Jafarmadar, S., Mobadersani, F., 2015. Experimental studies on heat transfer and pressure drop characteristics for new arrangements of corrugated tubes in a double pipe heat exchanger. *International Journal of Thermal Sciences* 96, 211–220.
- [26] Duffy, A., Rogers, M., Ayompe, L., 2015. *Renewable energy and energy efficiency: assessment of projects and policies*. John Wiley & Sons.
- [27] Eames, P., Norton, B., 1998. The effect of tank geometry on thermally stratified sensible heat storage subject to low reynolds number flows. *International Journal of Heat and Mass Transfer* 41 (14), 2131–2142.

-
- [28] Ehlers, W., 1995. A single-surface yield function for geomaterials. *Archive of Applied Mechanics* 65 (4), 246–259.
- [29] Ehlers, W., 2002. *Porous media: theory, experiments and numerical applications*. Springer Science & Business Media.
- [30] Ehlers, W., Avci, O., 2013. Stress-dependent hardening and failure surfaces of dry sand. *International Journal for Numerical and Analytical Methods in Geomechanics* 37 (8), 787–809.
- [31] Ehlers, W., Häberle, K., 2016. Interfacial mass transfer during gas-liquid phase change in deformable porous media with heat transfer. *Transport in Porous Media* 114 (2), 525–556.
- [32] Ehlers, W., Luo, C., 2017. A phase-field approach embedded in the Theory of Porous Media for the description of dynamic hydraulic fracturing. *Computer Methods in Applied Mechanics and Engineering* 315, 348–368.
- [33] Ermis, K., Erek, A., Dincer, I., 2007. Heat transfer analysis of phase change process in a finned-tube thermal energy storage system using artificial neural network. *International Journal of Heat and Mass Transfer* 50 (15), 3163–3175.
- [34] Farrell, P., Maurini, C., 2017. Linear and nonlinear solvers for variational phase-field models of brittle fracture. *International Journal for Numerical Methods in Engineering* 109 (5), 648–667.
- [35] Fernandes, D., Pitié, F., Cáceres, G., Baeyens, J., 2012. Thermal energy storage: “How previous findings determine current research priorities”. *Energy* 39 (1), 246–257.
- [36] Fernandez, A., Martínez, M., Segarra, M., Martorell, I., Cabeza, L., 2010. Selection of materials with potential in sensible thermal energy storage. *Solar Energy Materials and Solar Cells* 94 (10), 1723–1729.
- [37] Fesanghary, M., Damangir, E., Soleimani, I., 2009. Design optimization of shell and tube heat exchangers using global sensitivity analysis and harmony search algorithm. *Applied Thermal Engineering* 29 (5), 1026–1031.
- [38] Flueckiger, S. M., Iverson, B. D., Garimella, S. V., Pacheco, J. E., 2014. System-level simulation of a solar power tower plant with thermocline thermal energy storage. *Applied Energy* 113, 86–96.
- [39] Forster, M., 2004. Theoretical investigation of the system SnOx/Sn for the thermochemical storage of solar energy. *Energy* 29 (5), 789–799.
- [40] Francfort, G. A., Marigo, J.-J., 1998. Revisiting brittle fracture as an energy minimization problem. *Journal of the Mechanics and Physics of Solids* 46 (8), 1319–1342.
- [41] Freddi, F., Royer-Carfagni, G., 2010. Regularized variational theories of fracture: a unified approach. *Journal of the Mechanics and Physics of Solids* 58 (8), 1154–1174.
- [42] Gerasimov, T., De Lorenzis, L., 2016. A line search assisted monolithic approach for phase-field computing of brittle fracture. *Computer Methods in Applied Mechanics and Engineering* 312, 276–303.

-
- [43] Gil, A., Medrano, M., Martorell, I., Lazaro, A., Dolado, P., Zalba, B., Cabeza, L. F., 2010. State of the art on high temperature thermal energy storage for power generation. Part 1–Concepts, materials and modellization. *Renewable and Sustainable Energy Reviews* 14 (1), 31–55.
- [44] González-Portillo, L. F., Muñoz-Antón, J., Martínez-Val, J. M., 2017. An analytical optimization of thermal energy storage for electricity cost reduction in solar thermal electric plants. *Applied Energy* 185, 531–546.
- [45] Griffith, A. A., Eng, M., 1921. VI. The phenomena of rupture and flow in solids. *Philosophical Transactions of the Royal Society of London. Series A, Mathematical, Physical and Engineering Sciences* 221 (582-593), 163–198.
- [46] Gur, I., Sawyer, K., Prasher, R., 2012. Searching for a better thermal battery. *Science* 335 (6075), 1454–1455.
- [47] Hähnlein, S., Bayer, P., Ferguson, G., Blum, P., 2013. Sustainability and policy for the thermal use of shallow geothermal energy. *Energy Policy* 59, 914–925.
- [48] Han, H.-Z., Li, B.-X., Wu, H., Shao, W., 2015. Multi-objective shape optimization of double pipe heat exchanger with inner corrugated tube using RSM method. *International Journal of Thermal Sciences* 90, 173–186.
- [49] Hasnain, S., 1998. Review on sustainable thermal energy storage technologies, Part I: Heat storage materials and techniques. *Energy Conversion and Management* 39 (11), 1127–1138.
- [50] Hauer, A., Specht, M., Sterner, M., 2010. Energiespeicher-Steigerung der Energieeffizienz und Integration Erneuerbarer Energien. Report Themen, 110–114.
- [51] Heister, T., Wheeler, M. F., Wick, T., 2015. A primal-dual active set method and predictor-corrector mesh adaptivity for computing fracture propagation using a phase-field approach. *Computer Methods in Applied Mechanics and Engineering* 290, 466–495.
- [52] Herrmann, U., Kearney, D. W., 2002. Survey of thermal energy storage for parabolic trough power plants. *Journal of Solar Energy Engineering* 124 (2), 145–152.
- [53] Herrmann, U., Kelly, B., Price, H., 2004. Two-tank molten salt storage for parabolic trough solar power plants. *Energy* 29 (5), 883–893.
- [54] Hesarakı, A., Holmberg, S., Haghghat, F., 2015. Seasonal thermal energy storage with heat pumps and low temperatures in building projects—a comparative review. *Renewable and Sustainable Energy Reviews* 43, 1199–1213.
- [55] Hofacker, M., Miehe, C., 2012. Continuum phase field modeling of dynamic fracture: variational principles and staggered FE implementation. *International Journal of Fracture*, 1–17.
- [56] Irwin, G. R., 1958. Elasticity and plasticity: fracture. In: Flügge, S. (Ed.), *Encyclopedia of Physics*. Vol. 6. Springer, Berlin, Ch. 5, pp. 551–590.

-
- [57] Jacob, R., Belusko, M., Fernández, A. I., Cabeza, L. F., Saman, W., Bruno, F., 2016. Embodied energy and cost of high temperature thermal energy storage systems for use with concentrated solar power plants. *Applied Energy* 180, 586–597.
- [58] Jänchen, J., Ackermann, D., Stach, H., Brösicke, W., 2004. Studies of the water adsorption on zeolites and modified mesoporous materials for seasonal storage of solar heat. *Solar Energy* 76 (1), 339–344.
- [59] Jian, Y., Bai, F., Falcoz, Q., Xu, C., Wang, Y., Wang, Z., 2015. Thermal analysis and design of solid energy storage systems using a modified lumped capacitance method. *Applied Thermal Engineering* 75, 213–223.
- [60] Jian, Y., Falcoz, Q., Neveu, P., Bai, F., Wang, Y., Wang, Z., 2015. Design and optimization of solid thermal energy storage modules for solar thermal power plant applications. *Applied Energy* 139, 30–42.
- [61] John, E., Hale, M., Selvam, P., 2013. Concrete as a thermal energy storage medium for thermocline solar energy storage systems. *Solar Energy* 96, 194–204.
- [62] Kareem, Z. S., Abdullah, S., Lazim, T. M., Jaafar, M. M., Wahid, A. F. A., 2015. Heat transfer enhancement in three-start spirally corrugated tube: experimental and numerical study. *Chemical Engineering Science* 134, 746–757.
- [63] Khare, S., Dell’Amico, M., Knight, C., McGarry, S., 2013. Selection of materials for high temperature sensible energy storage. *Solar Energy Materials and Solar Cells* 115, 114–122.
- [64] Klemes, J. J., Arsenyeva, O., Kapustenko, P., Tovazhnyanskyy, L., 2015. Compact heat exchangers for energy transfer intensification: low grade heat and fouling mitigation. CRC Press.
- [65] Klinsmann, M., Rosato, D., Kamlah, M., McMeeking, R. M., 2015. An assessment of the phase field formulation for crack growth. *Computer Methods in Applied Mechanics and Engineering* 294, 313–330.
- [66] Kolditz, O., Bauer, S., Bilke, L., Böttcher, N., Delfs, J., Fischer, T., Görke, U., Kalbacher, T., Kosakowski, G., McDermott, C., et al., 2012. Opeengeosys: an open-source initiative for numerical simulation of thermo-hydro-mechanical/chemical (THM/C) processes in porous media. *Environmental Earth Sciences* 67 (2), 589–599.
- [67] Kolditz, O., Görke, U.-J., Shao, H., Wang, W., Bauer, S., 2016. Thermo-hydro-mechanical-chemical processes in fractured porous media: modelling and benchmarking: benchmarking initiatives. Springer.
- [68] Kolditz, O., Nagel, T., Shao, H., Wang, W., Bauer, S., 2018. Thermo-hydro-mechanical-chemical processes in fractured porous media: modelling and benchmarking: from benchmarking to tutoring. Springer.
- [69] Kuhn, C., 2013. Numerical and analytical investigation of a phase field model for fracture. Ph.D. thesis, Technische Universität Kaiserslautern.
- [70] Kuravi, S., Trahan, J., Goswami, D. Y., Rahman, M. M., Stefanakos, E. K., 2013. Thermal energy storage technologies and systems for concentrating solar power plants. *Progress in Energy and Combustion Science* 39 (4), 285–319.

-
- [71] Laing, D., Bahl, C., Bauer, T., Fiss, M., Breidenbach, N., Hempel, M., 2012. High-temperature solid-media thermal energy storage for solar thermal power plants. *Proceedings of the IEEE* 100 (2), 516–524.
- [72] Laing, D., Lehmann, D., Fiß, M., Bahl, C., 2009. Test results of concrete thermal energy storage for parabolic trough power plants. *Journal of Solar Energy Engineering* 131 (4), 041007.
- [73] Laing, D., Steinmann, W.-D., Tamme, R., Richter, C., 2006. Solid media thermal storage for parabolic trough power plants. *Solar Energy* 80 (10), 1283–1289.
- [74] Laing, D., Steinmann, W.-D., Viebahn, P., Gräter, F., Bahl, C., 2010. Economic analysis and life cycle assessment of concrete thermal energy storage for parabolic trough power plants. *Journal of Solar Energy Engineering* 132 (4), 041013.
- [75] Liu, M., Tay, N. S., Bell, S., Belusko, M., Jacob, R., Will, G., Saman, W., Bruno, F., 2016. Review on concentrating solar power plants and new developments in high temperature thermal energy storage technologies. *Renewable and Sustainable Energy Reviews* 53, 1411–1432.
- [76] Lizana, J., Chacartegui, R., Barrios-Padura, A., Valverde, J. M., 2017. Advances in thermal energy storage materials and their applications towards zero energy buildings: a critical review. *Applied Energy* 203, 219–239.
- [77] Mao, Q., 2016. Recent developments in geometrical configurations of thermal energy storage for concentrating solar power plant. *Renewable and Sustainable Energy Reviews* 59, 320–327.
- [78] Mavridou, S. G., Konstandinidis, E., Bouris, D. G., 2015. Experimental evaluation of pairs of inline tubes of different size as components for heat exchanger tube bundles. *International Journal of Heat and Mass Transfer* 90, 280–290.
- [79] Meng, J.-A., Liang, X.-G., Chen, Z.-J., Li, Z.-X., 2005. Experimental study on convective heat transfer in alternating elliptical axis tubes. *Experimental Thermal and Fluid Science* 29 (4), 457–465.
- [80] Mettawee, E.-B. S., Assassa, G. M., 2007. Thermal conductivity enhancement in a latent heat storage system. *Solar Energy* 81 (7), 839–845.
- [81] Michel, B., Mazet, N., Mauran, S., Stitou, D., Xu, J., 2012. Thermochemical process for seasonal storage of solar energy: characterization and modeling of a high density reactive bed. *Energy* 47 (1), 553–563.
- [82] Miehe, C., Dal, H., Schänzel, L.-M., Raina, A., 2016. A phase-field model for chemo-mechanical induced fracture in lithium-ion battery electrode particles. *International Journal for Numerical Methods in Engineering* 106 (9), 683–711.
- [83] Miehe, C., Hofacker, M., Schaezel, L.-M., Aldakheel, F., 2015. Phase field modeling of fracture in multi-physics problems. Part II. Coupled brittle-to-ductile failure criteria and crack propagation in thermo-elastic-plastic solids. *Computer Methods in Applied Mechanics and Engineering* 294, 486–522.

-
- [84] Miehe, C., Hofacker, M., Welschinger, F., 2010. A phase field model for rate-independent crack propagation: robust algorithmic implementation based on operator splits. *Computer Methods in Applied Mechanics and Engineering* 199 (45), 2765–2778.
- [85] Miehe, C., Mauthe, S., 2016. Phase field modeling of fracture in multi-physics problems. Part III. Crack driving forces in hydro-poro-elasticity and hydraulic fracturing of fluid-saturated porous media. *Computer Methods in Applied Mechanics and Engineering* 304, 619–655.
- [86] Miehe, C., Mauthe, S., Teichtmeister, S., 2015. Minimization principles for the coupled problem of Darcy–Biot-type fluid transport in porous media linked to phase field modeling of fracture. *Journal of the Mechanics and Physics of Solids* 82, 186–217.
- [87] Miehe, C., Schänzel, L.-M., Ulmer, H., 2015. Phase field modeling of fracture in multi-physics problems. Part I. Balance of crack surface and failure criteria for brittle crack propagation in thermo-elastic solids. *Computer Methods in Applied Mechanics and Engineering* 294, 449–485.
- [88] Miehe, C., Welschinger, F., Hofacker, M., 2010. A phase field model of electromechanical fracture. *Journal of the Mechanics and Physics of Solids* 58 (10), 1716–1740.
- [89] Miehe, C., Welschinger, F., Hofacker, M., 2010. Thermodynamically consistent phase-field models of fracture: variational principles and multi-field FE implementations. *International Journal for Numerical Methods in Engineering* 83 (10), 1273–1311.
- [90] Miró, L., Navarro, M. E., Suresh, P., Gil, A., Fernández, A. I., Cabeza, L. F., 2014. Experimental characterization of a solid industrial by-product as material for high temperature sensible thermal energy storage (TES). *Applied Energy* 113, 1261–1268.
- [91] Na, S., Sun, W., 2018. Computational thermomechanics of crystalline rock. Part I. A combined multi-phase-field/crystal plasticity approach for single crystal simulations. *Computer Methods in Applied Mechanics and Engineering*.
- [92] Ozger, O., Girardi, F., Giannuzzi, G., Salomoni, V., Majorana, C., Fambri, L., Baldassino, N., Di Maggio, R., 2013. Effect of nylon fibres on mechanical and thermal properties of hardened concrete for energy storage systems. *Materials & Design* 51, 989–997.
- [93] Patil, R., Mishra, B., Singh, I., 2018. An adaptive multiscale phase field method for brittle fracture. *Computer Methods in Applied Mechanics and Engineering* 329, 254–288.
- [94] Prasad, L., Muthukumar, P., 2013. Design and optimization of lab-scale sensible heat storage prototype for solar thermal power plant application. *Solar Energy* 97, 217–229.
- [95] Raju, M., Kumar, S., 2012. Optimization of heat exchanger designs in metal hydride based hydrogen storage systems. *International Journal of Hydrogen Energy* 37 (3), 2767–2778.
- [96] Rovira, A., Montes, M. J., Valdes, M., Martínez-Val, J. M., 2011. Energy management in solar thermal power plants with double thermal storage system and subdivided solar field. *Applied Energy* 88 (11), 4055–4066.
- [97] Şahin, A. Ş., Kılıç, B., Kılıç, U., 2011. Design and economic optimization of shell and tube heat exchangers using artificial bee colony (ABC) algorithm. *Energy Conversion and Management* 52 (11), 3356–3362.

-
- [98] Salomoni, V. A., Majorana, C. E., Giannuzzi, G. M., Miliozzi, A., Di Maggio, R., Girardi, F., Mele, D., Lucentini, M., 2014. Thermal storage of sensible heat using concrete modules in solar power plants. *Solar Energy* 103, 303–315.
- [99] Sargado, J. M., Keilegavlen, E., Berre, I., Nordbotten, J. M., 2018. High-accuracy phase-field models for brittle fracture based on a new family of degradation functions. *Journal of the Mechanics and Physics of Solids* 111, 458–489.
- [100] Shah, R. K., Sekulic, D. P., 2003. *Fundamentals of heat exchanger design*. John Wiley & Sons.
- [101] Sharma, A., Tyagi, V., Chen, C., Buddhi, D., 2009. Review on thermal energy storage with phase change materials and applications. *Renewable and Sustainable Energy Reviews* 13 (2), 318–345.
- [102] Skinner, J. E., Strasser, M. N., Brown, B. M., Selvam, R. P., 2014. Testing of high-performance concrete as a thermal energy storage medium at high temperatures. *Journal of Solar Energy Engineering* 136 (2), 021004.
- [103] Solar Millennium, A., 2013. *Die Parabolrinnen-Kraftwerke Andasol 1 bis 3—Die größten Solarkraftwerke der Welt*. Solar Millennium AG, Erlangen.
- [104] Soria, R., Lucena, A. F., Tomaschek, J., Fichter, T., Haasz, T., Szklo, A., Schaeffer, R., Rochedo, P., Fahl, U., Kern, J., 2016. Modelling concentrated solar power (CSP) in the Brazilian energy system: a soft-linked model coupling approach. *Energy* 116, 265–280.
- [105] Tamme, R., Laing, D., Steinmann, W.-D., 2004. Advanced thermal energy storage technology for parabolic trough. *Journal of Solar Energy Engineering* 126 (2), 794–800.
- [106] Tamme, R., Steinmann, W.-D., Laing, D., 2003. High temperature thermal energy storage technologies for power generation and industrial process heat. In: *Proceedings of FUTURE-STOCK 2003, 9th International Conference on Thermal Energy Storage*. Warsaw, Poland.
- [107] Tanné, E., Li, T., Bourdin, B., Marigo, J.-J., Maurini, C., 2018. Crack nucleation in variational phase-field models of brittle fracture. *Journal of the Mechanics and Physics of Solids* 110, 80–99.
- [108] Tiari, S., Qiu, S., 2015. Three-dimensional simulation of high temperature latent heat thermal energy storage system assisted by finned heat pipes. *Energy Conversion and Management* 105, 260–271.
- [109] Velraj, R., Seeniraj, R., Hafner, B., Faber, C., Schwarzer, K., 1999. Heat transfer enhancement in a latent heat storage system. *Solar Energy* 65 (3), 171–180.
- [110] Weinstein, L. A., Loomis, J., Bhatia, B., Bierman, D. M., Wang, E. N., Chen, G., 2015. Concentrating solar power. *Chemical Reviews* 115 (23), 12797–12838.
- [111] Wilson, Z. A., Landis, C. M., 2016. Phase-field modeling of hydraulic fracture. *Journal of the Mechanics and Physics of Solids* 96, 264–290.

-
- [112] Wong, J. Y., Sharma, S., Rangaiah, G., 2015. Design of shell-and-tube heat exchangers for multiple objectives using elitist non-dominated sorting genetic algorithm with termination criteria. *Applied Thermal Engineering*.
- [113] Wu, J.-Y., 2017. A unified phase-field theory for the mechanics of damage and quasi-brittle failure. *Journal of the Mechanics and Physics of Solids* 103, 72–99.
- [114] Wu, M., Li, M., Xu, C., He, Y., Tao, W., 2014. The impact of concrete structure on the thermal performance of the dual-media thermocline thermal storage tank using concrete as the solid medium. *Applied Energy* 113, 1363–1371.
- [115] Yang, Z., Garimella, S. V., 2013. Cyclic operation of molten-salt thermal energy storage in thermoclines for solar power plants. *Applied Energy* 103, 256–265.
- [116] Yuan, H., Shi, Y., Lu, C., Xu, Z., Ni, Y., Lan, X., 2015. Enhanced performance of high temperature aluminate cementitious materials incorporated with Cu powders for thermal energy storage. *Cement and Concrete Composites* 55, 139–144.
- [117] Zalba, B., Marín, J. M., Cabeza, L. F., Mehling, H., 2003. Review on thermal energy storage with phase change: materials, heat transfer analysis and applications. *Applied Thermal Engineering* 23 (3), 251–283.
- [118] Zhang, H., Baeyens, J., Caceres, G., Degreve, J., Lv, Y., 2016. Thermal energy storage: recent developments and practical aspects. *Progress in Energy and Combustion Science* 53, 1–40.
- [119] Zhang, H., Baeyens, J., Degrève, J., Cacères, G., 2013. Concentrated solar power plants: review and design methodology. *Renewable and Sustainable Energy Reviews* 22, 466–481.
- [120] Zhang, X., Vignes, C., Sloan, S. W., Sheng, D., 2017. Numerical evaluation of the phase-field model for brittle fracture with emphasis on the length scale. *Computational Mechanics* 59 (5), 737–752.
- [121] Zheng, N., Liu, W., Liu, Z., Liu, P., Shan, F., 2015. A numerical study on heat transfer enhancement and the flow structure in a heat exchanger tube with discrete double inclined ribs. *Applied Thermal Engineering* 90, 232–241.

APPENDIX

1 PROCESSES DEVELOPMENT IN OGS

1.1 A visco-elastic material model for simple-shear creep

A visco-elastic (LUBBY2) constitutive model is implemented in OGS-6 (An ongoing version of OpenGeoSys (OGS) platform, aiming to introduce new processes and solution techniques) to model the primary and secondary creep of rock salt. This material model is an extension of the generalised Burgers model, see Figure 15. A detailed model description can be found in Chapter 3.17 of [68].

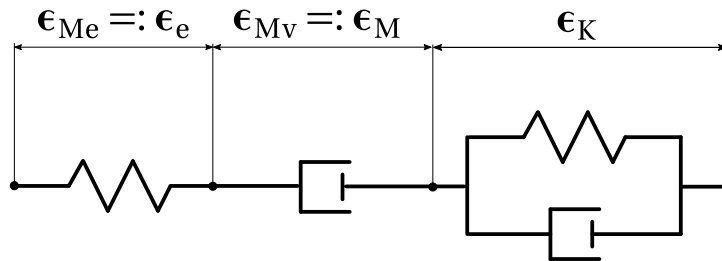


Figure 15: Rheological analogue of the LUBBY2 model.

Benchmark testing is stated in <https://www.opengeosys.org/docs/benchmarks/small-deformations/mechanics-lubby2-shear-traction/>, with input files available at <https://github.com/ufz/ogs-data/tree/master/Mechanics/Burgers>.

1.2 An elasto-plastic material model with hardening

A elasto-plastic material model is implemented in OGS-6 based on a seven-parametric yield function [28, 30], see Figure 16. It is used to simulate the non-linear mechanical behaviour of geomaterials. A detailed model description can be found in Chapter 3.18 of [68].

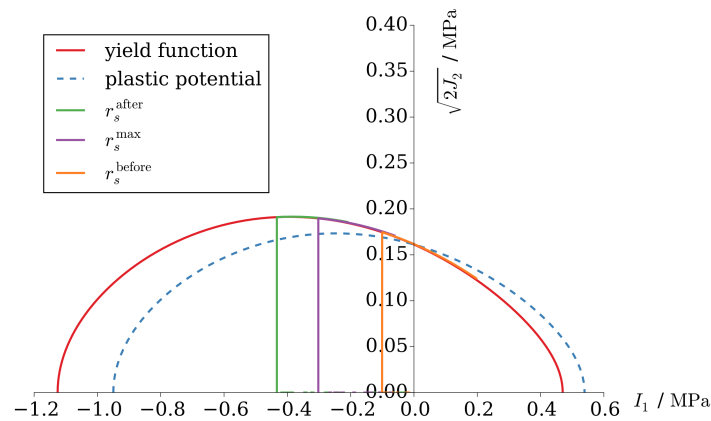


Figure 16: Characteristic shape of the yield function and the plastic potential in the hydrostatic plane.

Benchmark testing is described in <https://www.opengeosys.org/docs/benchmarks/small-deformations/mechanics-plasticity-single-surface/> and <https://www.opengeosys.org/docs/benchmarks/small-deformations/mechanics-plasticity-ehlers-specialcase-drucker-prager/>, with input files available for exercise and scientific research under <https://github.com/ufz/ogs-data/tree/master/Mechanics/Ehlers>.

1.3 A phase-field model of brittle fracture

A phase-field model for brittle fracture is implemented in OGS-6 to examine crack evolution in solids. It is a continuous numerical instrument which can be capable of describing the lower-dimensional crack boundaries using phase transition, see Figure 10. The concept explanation and detailed model derivation can be found in Appendix 2.4.

A numerical example is demonstrated in <https://www.opengeosys.org/docs/benchmarks/phase-field/phasefield/>. A series of benchmarks containing full input files can be found at <https://github.com/ufz/ogs-data/tree/master/PhaseField>.

1.4 A thermo-mechanical material model for elastic solids

A thermo-mechanical constitutive model is implemented in OGS-6 to evaluate mechanical response of elastic solids under non-isothermal conditions. Benchmark testing is displayed in <https://www.opengeosys.org/docs/benchmarks/thermo-mechanics/thermomechanics/>, with input files available at <https://github.com/ufz/ogs-data/tree/master/ThermoMechanics>.

1.5 A thermo-mechanical phase-field model of brittle fracture

A phase-field model of brittle fracture coupled with heat transport is implemented in OGS-6 to examine crack evolution driven by thermo-mechanical loading. It can be used to quantify the potential thermal performance degradation of a system associated with thermal engineering. The derivation of constitutive equations from entropy inequality is presented in this contribution. Benchmark testing and evaluation of model implementation are described in <https://www.opengeosys.org/docs/benchmarks/thermo-mechanical-phase-field/thermo-mechanical-phase-field/> (Appendix 2.5, Chapter 9.7 of [68]), with input files available

at <https://github.com/xingyuanmiao/ogs/tree/staggeredThermoMechanicalPhaseField/Tests/Data/ThermoMechanicalPhaseField>.

1.6 *A thermo-hydro-mechanical model for porous media*

A thermo-hydro-mechanical model is implemented in OGS-6 to simulate multi-field problems in porous media, e.g. the coupling between heat transport and biphasic consolidation in saturated porous media. A brief derivation of the governing equations is written in Appendix 2.1. The governing equations are assembled and solved monolithically. Benchmark testing and evaluation of model implementation are described in Chapter 10.4 of [68], with input files available at <https://github.com/ufz/ogs-data/tree/master/ThermoHydroMechanics>.

2 DETAILED DESCRIPTION OF MODELS DEVELOPMENT AND APPLICATIONS

2.1 Governing equations for fluid-saturated porous media

The mixture volume balance equation (Eq. (1)) can be obtained from the mass balance equations of the two constituents

$$\phi_S (\rho_{SR})'_S + (\phi_S)'_S \rho_{SR} + \rho_{SR} \phi_S \operatorname{div}(\mathbf{u}_S)'_S = 0 \quad (25)$$

$$\phi_F (\rho_{FR})'_F + (\phi_F)'_F \rho_{FR} + \rho_{FR} \phi_F \operatorname{div}(\mathbf{v}_F) = 0 \quad (26)$$

and the saturation condition

$$\phi_S + \phi_F = 1 \quad (27)$$

The material time derivative of the material density of each constituent can be written as

$$(\rho_{SR})'_S = \frac{\partial \rho_{SR}}{\partial \theta} \theta'_S = -\rho_{SR} \beta_{TS} \theta'_S \quad (28)$$

$$(\rho_{FR})'_F = \frac{\partial \rho_{FR}}{\partial \theta} \theta'_F = -\rho_{FR} \beta_{TF} \theta'_F \quad (29)$$

with

$$\beta_{SR} = -\frac{1}{\rho_{SR}} \frac{\partial \rho_{SR}}{\partial \theta} \quad (30)$$

$$\beta_{FR} = -\frac{1}{\rho_{FR}} \frac{\partial \rho_{FR}}{\partial \theta} \quad (31)$$

and

$$\theta'_F = \theta'_S + \operatorname{grad} \theta \cdot \mathbf{w}_{FS} \quad (32)$$

The material time derivative of the saturation condition with respect to the solid phase writes

$$(\phi_S)'_S + (\phi_F)'_S = (\phi_S)'_S + (\phi_F)'_F - \operatorname{grad} \phi_F \cdot \mathbf{w}_{FS} \quad (33)$$

Rearranging Eq. (25) and Eq. (26), and using Eq. (28) and Eq. (29), one writes

$$(\phi_S)'_S = \phi_S \beta_{TS} \theta'_S - \phi_S \operatorname{div}(\mathbf{u}_S)'_S \quad (34)$$

$$(\phi_F)'_F = \phi_F \beta_{TF} \theta'_F - \phi_F \operatorname{div}(\mathbf{v}_F) \quad (35)$$

The insertion of Eq. (34) and Eq. (35) into Eq. (33), and the employment of Eq. (32) yield the mixture volume balance equation.

The linear momentum balance equations of the two constituents write

$$\operatorname{div} \boldsymbol{\sigma}_S + \phi_S \rho_{SR} \mathbf{g} + \hat{\mathbf{p}}_S = \mathbf{0} \quad (36)$$

$$\operatorname{div} \boldsymbol{\sigma}_F + \phi_F \rho_{FR} \mathbf{g} + \hat{\mathbf{p}}_F = \mathbf{0} \quad (37)$$

with

$$\boldsymbol{\sigma}_S^E = \boldsymbol{\sigma}_S + \phi_S p \mathbf{I} \quad (38)$$

$$\boldsymbol{\sigma}_F^E = \boldsymbol{\sigma}_F + \phi_F p \mathbf{I} \quad (39)$$

The entropy inequality writes

$$\sigma_S^E : \epsilon_S + \sigma_F^E : \epsilon_F - \varrho_S (\bar{\psi}_S)'_S - \varrho_F (\bar{\psi}_F)'_F - \hat{\mathbf{p}}_F^E \cdot \mathbf{w}_{FS} \geq 0 \quad (40)$$

with

$$\hat{\mathbf{p}}_F = \hat{\mathbf{p}}_F^E + p \text{grad} \phi_F \quad (41)$$

and the dissipation inequality is sufficiently satisfied with (cf. [29])

$$\hat{\mathbf{p}}_F^E = -(\phi_F)^2 \mu_{FR} (\kappa_F)^{-1} \mathbf{w}_{FS} \quad (42)$$

The Darcy equation (Eq. (2)) can be obtained from the momentum balance of the fluid phase, i.e. Eq. (37). The substitution of Eq. (39) and Eq. (41) into Eq. (37) with neglecting the friction force $\text{div} \sigma_F^E$ incorporated in Eq. (37) yields the Darcy equation.

The mixture momentum balance equation (Eq. (4)) can be obtained from an additive combination of momentum balance equations of the two constituents given in Eq. (36) and Eq. (37).

The energy equations of the two constituents write

$$\varrho_{SR} c_{pS} \vartheta'_S - \text{div} (\lambda_S \text{grad} \vartheta) = 0 \quad (43)$$

$$\varrho_{FR} c_{pF} \vartheta'_F - \text{div} (\lambda_F \text{grad} \vartheta) = 0 \quad (44)$$

The mixture energy balance equation can be obtained by combining the energy equation of the solid and the fluid phase given in Eq. (43) and Eq. (44), with neglecting the work done by pressures changes, radiative effects, viscous dissipation. Particularly, the effective thermal properties that contain the contributions from the two constituents are introduced in the mixture energy equation, see Eq. (8) and Eq. (9).

Note that the balance equations are written under the assumptions that (a) all phases are assumed materially incompressible, i.e. $\varrho_{\alpha R} = \varrho_{\alpha R}(\vartheta)$; (b) the local temperatures of the two constituents are equal (local thermal equilibrium: $\vartheta_\alpha = \vartheta$); (c) no mass exchange occurs between the two constituents.

2.2 *Thermo-hydro-mechanical modelling of solid-fluid sensible heat storage*

X.-Y. Miao, C. Beyer, U.-J. Görke, O. Kolditz, H. Hailemariam, T. Nagel, Thermo-hydro-mechanical analysis of cement-based sensible heat stores for domestic applications. *Environmental Earth Sciences*, Volume 75, Issue 18, September 2016, Article:1293.

Thermo-hydro-mechanical analysis of cement-based sensible heat stores for domestic applications

Xing-Yuan Miao^{1,2} · Christof Beyer³ · Uwe-Jens Görke¹ · Olaf Kolditz^{1,2} · Henok Hailemariam³ · Thomas Nagel^{1,4}

Received: 21 January 2016 / Accepted: 13 September 2016
© Springer-Verlag Berlin Heidelberg 2016

Abstract The thermo-hydro-mechanical behaviour of a water-saturated cement-based heat store for domestic applications has been investigated. Numerical simulations have been employed to locate the critical regions during thermal loading, for which analytical solutions have been derived and validated by numerical simulations. The analytical solutions allow a fast screening of materials and design parameters in relation to the stresses induced by thermomechanical loading. Maximum stresses in the system have been quantified based on the thermomechanical properties of three heat exchanger materials selected by design engineers and of the filling material. Sensitivity analyses indicate that the stress distribution is very sensitive to the thermal expansion coefficients of the involved materials. The results of this study can serve as a guide line for the design of the present and similar heat storage systems. The analytical solution developed is a fast and robust method for the evaluation of stresses around heat exchangers embedded in a solid material and can serve as a tool for design optimisation.

Keywords Thermoelasticity · Sensible heat storage · Heat exchanger interface · Solar thermal systems · OpenGeoSys

Introduction

Thermal energy storage is a technology mainly used for mitigating demand and supply fluctuations in thermal power plants, for district heating, for domestic hot water production and space heating, as well as for increasing the efficiency of thermal processes in industry. It has recently gained interest in the renewable energy sector for seasonal, diurnal and short-cycle heat storage as well as for load management in the electricity grid. See, for example, Carson and Moses (1963), Braun et al. (1981), Neepser (2000), Khudhair and Farid (2004), Bauer et al. (2010) and Hesarakı et al. (2015).

Three main technologies are available for implementing thermal energy storage: sensible heat storage, latent heat storage and thermochemical storage. Sensible heat storage is widely used in practical applications mostly due its comparatively low cost and technical maturity (Dincer et al. 1997; Hasnain 1998; Duffy et al. 2015). It is based on directly storing the thermal energy by raising the temperature of liquid or solid media. Latent heat storage absorbs or releases energy primarily through a phase change of the storage material. This system can provide a higher storage density and can store significant amounts of heat in a narrow temperature range around the phase change temperature. Many investigations are conducted to improve the performance and viability of latent heat storage systems (Abhat 1983; Lane 1983; Kim and Drzal 2009; Sharma et al. 2009; Velraj et al. 1999; Zalba et al. 2003; Mettawee and Assassa 2007). Thermochemical storage converts and releases thermal energy by chemical reactions or

This article is part of a Topical Collection in Environmental Earth Sciences on “Subsurface Energy Storage”, guest edited by Sebastian Bauer, Andreas Dahmke, and Olaf Kolditz.

✉ Thomas Nagel
thomas.nagel@ufz.de

- ¹ Helmholtz Centre for Environmental Research – UFZ, Leipzig, Germany
- ² Technische Universität Dresden, Dresden, Germany
- ³ Christian-Albrechts-Universität zu Kiel, Kiel, Germany
- ⁴ Trinity College Dublin, Dublin, Ireland

adsorption processes (Nagel et al. 2016). Due to high storage densities, thermochemical heat stores can potentially be integrated into applications where space is limited and can store heat for extended periods of time in a chemical or physical potential. However, latent heat storage and especially thermochemical heat storage are still in a development stage. Besides, the performance and cycle stability of latent heat storage and thermochemical storage remain challenging issues (Mettawee and Assassa 2007; Sharma et al. 2009; Agyenim et al. 2010b; Forster 2004; Jänchen et al. 2004; Michel et al. 2012). Additionally, the costs associated with the complex heat transfer system components and integration into co-generation energy supply are much higher for latent and thermochemical heat storage than for sensible heat storage (Hasnain 1998; Velraj et al. 1999; Zalba et al. 2003; Agyenim et al. 2010a). Sensible heat storage therefore remains one of the most common and appropriate systems for many domestic and commercial applications.

Besides sensible heat storage using liquids such as water, thermal oils or molten salt, solid sensible heat storage can be used to capture the solar thermal power via storage media such as rocks, concrete and ceramics (Laing et al. 2006; Gil et al. 2010; Salomoni et al. 2014; Jian et al. 2015a, b). Research currently focuses on efficiency enhancement and economic optimisation of this solid medium thermal storage (Hasnain 1998; Laing et al. 2012; Prasad and Muthukumar 2013; Salomoni et al. 2014; Jian et al. 2015b). In the survey of thermal energy storage performed by Herrmann and Kearney (2002), concrete is mentioned as a promising solid medium for sensible heat storage. Laing et al. (2006) have comprehensively investigated the construction of solid media thermal storage systems. The study compared the performance of two solid storage materials in a parabolic trough test loop. As claimed in their investigation (Laing et al. 2006), high-temperature concrete exposed to a maximum temperature of 390 °C has been regarded as the preferred material for practical applications due to low investment costs and high operability. Consequently, specific research on concrete as a solid medium for storing sensible heat has been further studied by Laing et al. (2012). The thermal cycling stability and economics of this material have been validated by conducting module tests in parabolic trough solar thermal power plants. John et al. (2013) have developed a concrete mixture with the objective of reducing the cost for thermal storage in order to make it more competitive compared to traditional power generation. Meanwhile, Skinner et al. (2014) evaluated the heat transfer efficiency of different heat exchanger configurations embedded in concrete for thermal storage in a temperature regime of around 400 °C. They observed a strong propensity to cracking of the high-strength concrete used as a

consequence of thermally induced stresses. Relatively soft interface materials were confirmed to provide significant tensile stress relief by absorbing deformations of the heat exchangers and thus helped to prevent crack initiation and propagation in the concrete (Skinner et al. 2014).

A novel subsurface sensible heat store for the building sector

Economic heat storage is a key technology for domestic and commercial solar thermal applications. In current solid sensible heat storage, the most prevalent system is a storage tank with water (domestic) or molten salt (high-temperature applications for power generation) as heat storage media (Hasnain 1998; Herrmann et al. 2004; Kuravi et al. 2013).

However, this technology has the disadvantages of a large space demand, a complex process handling and tanks requiring expensive corrosion resistant materials (refer to the solar district heating “Am Ackermann-bogen” project (Munich, Germany) conducted by the Bavarian Centre for Applied Energy Research (Germany) (Hauer et al. 2010), and the parabolic trough power plant “Andasol” (Andalusia, Spain) developed by Solar Millennium AG (Germany) (Solar Millennium 2013) as examples). In order to increase the solar share in domestic applications, solar thermal or photovoltaic installations need to be combined with suitable storage technologies.

In the city of Rostock (Germany), for example, solar thermal installations are combined with an aquifer thermal energy storage (so-called ATES) system, where hot water is stored in a shallow aquifer during the summer season at about 50 °C and re-extracted in the heating period to support heating and warm water demand of a housing development area (Bauer et al. 2010, 2013). Seasonal borehole thermal energy storage (so-called BTES), where solar thermal heat is stored and regained from the subsurface via arrays of borehole heat exchangers, is used, for example, in Crailsheim and Neckarsulm (Germany) (Bauer et al. 2010) with maximum subsurface temperatures of up to 55 and 65 °C, respectively. Concerns on potentially negative impacts of such temperature increases on groundwater quality, however, currently restrict the approval of high-temperature ATES or BTES in the subsurface (Hähnlein et al. 2013). The IGLU project¹ aims at developing a solid sensible heat store with embedded heat exchangers through which a heat transfer medium, in the

¹ “Untersuchung, Modellierung und Bewertung eines intelligenten geothermischen Langzeitwärmespeichers mit umweltneutralem Verhalten”, or “Analysis, Modelling and assessment if an intelligent and environmentally neutral geothermal long-term heat storage system” is a project funded by the German Federal Ministry of Economy and Energy (BMWi).

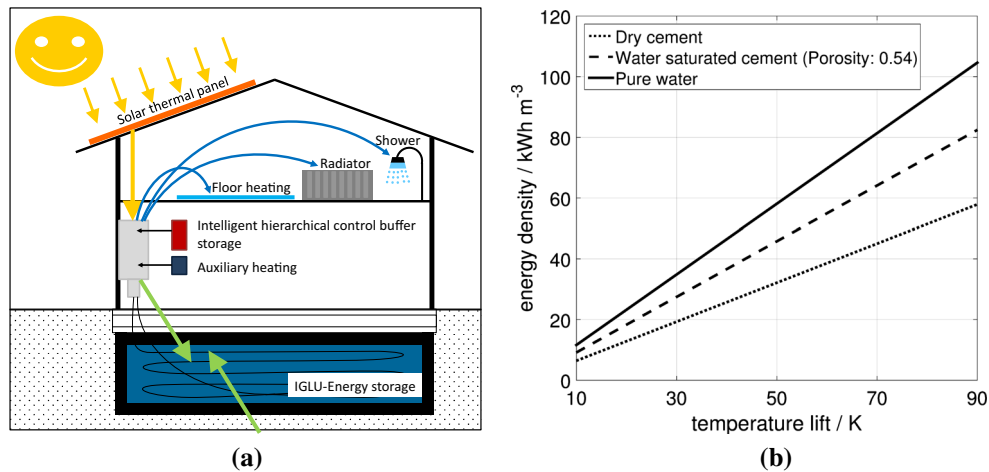


Fig. 1 Concept of the sensible heat store (*left*) and energy storage density (*right*). **a** Schematic of the system configuration investigated as part of the IGLU project. **b** Energy capacity with different temperature lifts

present case water, is flowing. This solution is considered an effective alternative to currently available storage systems for limiting vessel costs, process complexity and space requirements combined with easy handling and the general advantages of sensible heat storage. An inexpensive cement-based filling material is investigated as the storage medium, combined with easily available piping equipment for heat exchangers made of aluminium alloys or polyethylene which are regarded feasible options for domestic solar thermal energy storage in terms of performance and investment costs. The project IGLU is concerned with investigating and validating the modular design, the performance and the environmental impact of such a heat store.

The investigation of the environmental impact becomes necessary for the heat store considered here because of the inherent space saving concept which rests on two aspects: (1) the storage modules can be integrated not only into the basement of a house but also directly into the subsurface (see Fig. 1a); (2) compared to purely solid storage media, the energy storage capacity is increased by saturating the porous filling material with water.

Figure 1b shows the comparison of the energy density achievable with three types of the storage media depending on the temperature lift. It can be observed that compared to the dry cement, the water-saturated cement with porosity of 0.54 has a significantly increased storage capacity, approaching the values of water.

The thermal performance characteristics of the heat store will be investigated in a companion paper. This article focuses on the analysis of the thermo-hydro-mechanical (THM) behaviour of the filling material and the heat exchangers. In order to estimate the thermally induced stresses, both analytical and numerical approaches have been employed. The former have been developed to allow

design engineers an efficient screening of different combinations of heat exchanger materials with solid storage media. The results will be used to judge the mechanical integrity of the system under thermal loading and to determine whether any special treatment may be necessary during the construction phase.

Outline

The paper is organized as follows. In the “[Experimental procedures for determining material properties](#)” section, the experimental basics are briefly reviewed. A test heat store is analysed numerically in “[Numerical simulations of a test rig for system development](#)” to identify critical regions from a thermomechanical perspective. For this region, a novel analytical solution is developed in the section “[Analytical solution in the near field of the heat exchanger](#)” and validated against literature data as well as numerical models. The analytical solution is used in the “[Sensitivity analysis](#)” section to perform sensitivity analyses with respect to the most important material parameters. The paper closes with “[Conclusions and discussions](#)”.

Experimental procedures for determining material properties

In this section, a brief summary of the experimental protocols and results relevant for this paper will be provided.

The material properties of the composite heat exchanger are available through data sheets provided by the manufacturer.² Here, only the properties of the cement-based

² WAVIN®, <http://de.wavin.com>.

filling material³ were measured. The cement-based commercial materials were prepared with a water-to-solid ratio of 0.8 and stored under water for 28 days. Underwater storage ensures full saturation of samples and prevents cracks that may occur within 72 h during cement hydration after sample preparation. The thermal conductivity and specific heat capacity were measured with a Decagon KD2 Pro thermal needle probe, based on transient line source measurement in compliance with ASTM D5334-08 (ASTM 2008) and IEEE 442 standards (IEEE 1992). The KD2 Pro includes a linear heat source and a temperature sensor with a resolution of 0.001 °C. Based on the analyses presented in Carslaw and Jaeger (1959) and Kluitenberg et al. (1993), thermal needle probes SH-1 (dual needle), with a length of 30 mm, a diameter 1.3 mm and a 6-mm spacing of the probe needles, and TR-1 (single needle) with a length of 100 mm and a diameter of 2.4 mm, were used to measure the sample's specific heat capacity and thermal conductivity at room temperature and atmospheric pressure, respectively. The conceptual requirement of an infinitely long and thin heating source was satisfied by a sufficient length-to-diameter ratio of the probes. The measurement error recorded for all samples was maintained below 0.015 %. The thermal conductivity and thermal diffusivity can be obtained by using the following relations:

$$\lambda = \frac{Q(\ln t_2 - \ln t_1)}{4\pi(\Delta T_2 - \Delta T_1)} \tag{1}$$

with

$$\Delta T = \frac{-Q}{4\pi\lambda} \text{Ei}\left(\frac{-r^2}{4Dt}\right) \tag{2}$$

where λ represents the thermal conductivity, Q is the heat source, ΔT is the temperature response of the source over time, r is the distance between the heater and the sensor where the temperature would be measured, t is the amount of time that has passed during the heating process, Ei is the exponent integral (Abramowitz and Stegun 1972) and D represents the thermal diffusivity.

The specific heat capacity of the cement-based filling material was obtained using the dual needle thermal probe SH-1. Initially, the heat source was applied via the heating needle, and the respective temperature was measured in the monitoring needle at a distance of 6 mm. The same procedure was then applied during the cooling period following the heating stage. The readings were then processed by subtracting the ambient temperature at the initial time, multiplying by a factor of 4π and then dividing by the heat source per unit length.

³ Füllbinder L, SCHWENK Zement KG®, <http://www.schwenkzement.de/de/Produkte/Produktuebersicht-Zemente.php>.

$$T^* = \frac{4\pi(T - T_0)}{Q} \tag{3}$$

The experimental data were fitted with the following equations using a nonlinear least squares method:

- For the heating process

$$T^* = b_0t + b_1\text{Ei}\left(\frac{b_2}{t}\right) \tag{4}$$

- For the cooling process

$$T^* = b_0t + b_1\left\{\text{Ei}\left(\frac{b_2}{t}\right) - \text{Ei}\left(\frac{b_2}{t - t_h}\right)\right\} \tag{5}$$

where b_0 , b_1 and b_2 are the constants to be fitted.

After obtaining the three constants, the thermal conductivity, thermal diffusivity and the specific heat capacity can be expressed as:

$$\lambda = \frac{1}{b_1}, D = \frac{r^2}{4b_2}, c = \frac{\lambda}{\rho D} \tag{6}$$

A thermal expansion and conductivity meter was used to obtain the linear thermal expansion coefficient. The apparatus is composed of a top heating plate, a bottom cooling plate and a reference disc with a known thermal conductivity, see Fig. 2. The specimen was sandwiched between the top heating and reference plates. The two plates consist of the extremely thin PT 100 temperature sensors with an accuracy of 0.05 °C. The system measured sample deformation with a TRS-0050 linear transducer with an independent linearity of 0.15 % and a repeatability of 2 μm. Samples were prepared with a diameter of 50 mm and a sufficient length of 40 mm to produce a linear temperature variation during the heating process. The sample expansion tests were conducted under fully saturated conditions by heating the top plate with a constant rate of 2 K/min and in a temperature range of 22–75 °C.

For the system shown in Fig. 2, $T_1 > T_2 > T_3$ ensures that the heat flow was directed from the top surface via the sample and the reference disc to the bottom surface. Assuming that the temperature gradient within a homogeneous body is linear (Sass and Stegner 2012) one finds

$$\frac{T_1 - T_2}{\frac{S_p}{\lambda_p} + \frac{S_v}{\lambda_v}} = \frac{T_2 - T_3}{\frac{S_{23}}{\lambda_v}} \tag{7}$$

The average temperature in the sample can be obtained as:

$$T_{av} = \frac{1}{2} \left\{ T_1 + T_3 \left[1 + \frac{S_v(T_2 - T_3)}{T_3 S_{23}} \right] \right\} \tag{8}$$

where T_1 , T_2 and T_3 represent the temperature of the top plate, the reference disc and the bottom plate, respectively. T_{av} is the average temperature in the sample. λ_p and λ_v are the thermal conductivity of the sample and the reference

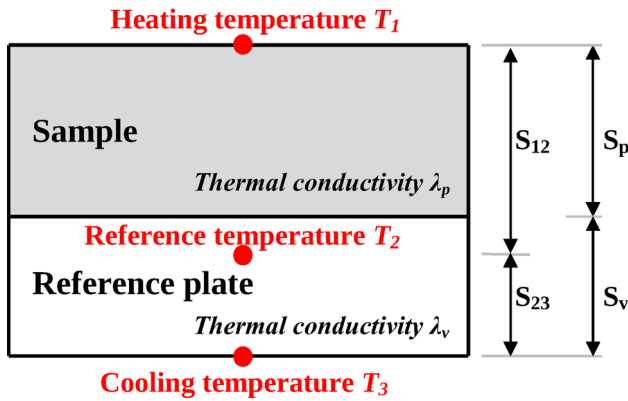


Fig. 2 The determination apparatus of the thermal expansion coefficient

disc, respectively. S_p , S_v and S_{23} are the distances plotted in Fig. 2.

The mean thermal expansion coefficient was calculated according to ASTM E831-06 (ASTM 2006):

$$\alpha_m = \frac{\Delta L_{sp} k}{L \Delta T} \tag{9}$$

and

$$k = \frac{\alpha_{ref} L_{ref} \Delta T_{ref}}{\Delta L_{ref}} \tag{10}$$

where α_m is the mean linear coefficient of thermal expansion of the sample; α_{ref} is the mean linear coefficient of thermal expansion of the reference material; k is the calibration coefficient; L is the specimen length at room temperature; ΔL_{sp} is the change of the specimen length; L_{ref} is the reference material length at room temperature; ΔL_{ref} is the change of the reference material length due to heating; ΔT is the temperature difference over which the change in the specimen length is measured; and ΔT_{ref} is the temperature difference over which the change in the reference material length is measured. Polyoxymethylene (POM) thermoplastic was selected as the reference material due to its low thermal conductivity, high stiffness, low friction, excellent dimensional stability and known linear thermal expansion coefficient.

The baseline correction was obtained using an inert or a low-expansion invar alloy. The accuracy of the measurement was verified by comparing the testing results of the thermal expansion coefficient of three metal samples (aluminium, stainless steel and brass) with the standard values, see Table 1. The maximum relative error between the measured and standard values was 4 %.

Figure 3 depicts the variations of the thermal expansion of the sample during the heating process with respect to the temperatures at the top surface and the average temperature of the specimen. The linear thermal expansion coefficient

Table 1 Comparison of the measured and standard values of the linear thermal expansion coefficient of three metals used as reference materials

Materials	Measured $\alpha_T / (\text{K}^{-1} \cdot 10^{-6})$	Standard $\alpha_T / (\text{K}^{-1} \cdot 10^{-6})$
Aluminium	23.77	23.60
Stainless steel	14.54	14.90
Brass	19.87	19.10

appears constant at first approximation in this temperature interval.

Numerical simulations of a test rig for system development

To test the basic charging and discharging behaviour of this type of heat store, and to validate thermal process models, a test set-up was built and analysed both experimentally and numerically. To perform numerical analyses, a computational model of this test rig has been developed. The geometry and boundary conditions of the test structure are illustrated in Fig. 4.

For these simulations, an aluminium–polyethylene composite pipe has been chosen as the heat exchanger. The multilayer composite designed for plumbing and heating applications consists of an internal cross-linked polyethylene tube, an outer tube made of high-density polyethylene and an aluminium tube in the middle. The material properties of the composite were taken according to company data sheets, see Table 2. As storage medium, the cementitious material Füllbinder L, manufactured by SCHWENK Zement KG®, was chosen as representative of a group of possible filling materials identified for this application, see Table 2 as well.

Based on previous research, the near field of the heat exchanger can be implied as a critical region in this type of structure (Skinner et al. 2014). During thermal loading and unloading, inhomogeneous temperature fields with strong gradients develop also in regions farther away from the heat exchangers. To identify whether these gradients lead to additional critical regions where stresses originate from incompatible thermal strains, a numerical simulation of the charging phase of the entire heat store was conducted. The numerical simulations in this section cover two aspects: (1) a thermomechanical analysis to locate potentially critical regions caused by incompatible thermal strains originating from temperature gradients or jumps in material properties. These results will form the basis of more detailed analyses of the thermomechanical processes presented in the later sections; (2) a thermo-

Fig. 3 Variation of the thermal expansion through the temperature at the top surface (left) and the average temperature (right) of the specimen

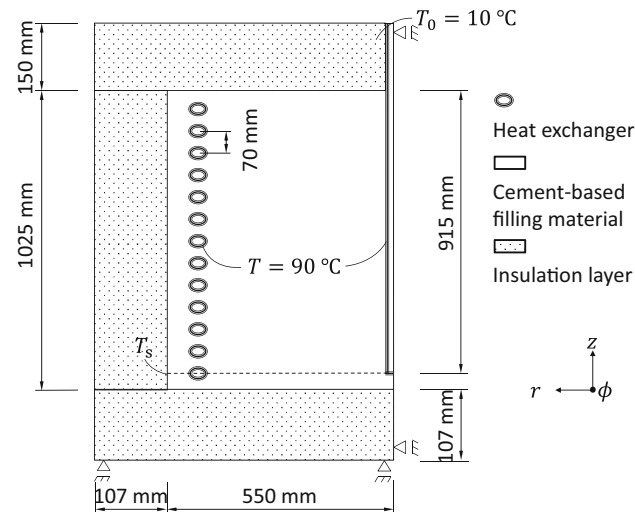
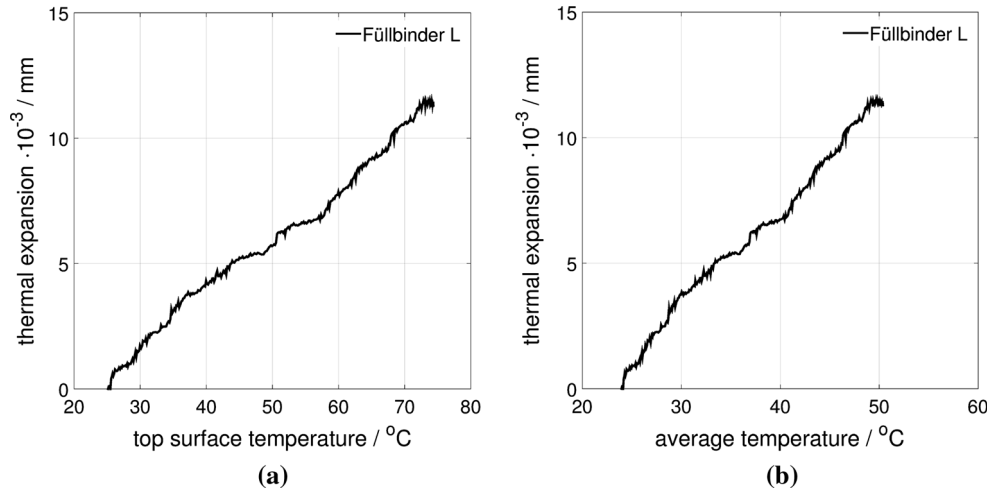


Fig. 4 Geometry and boundary conditions of the test structure

hydro-mechanical analysis explicitly accounting for the effects of fluid pressure under drained and undrained conditions. These analyses aim to answer the question whether the porous solid experiences excessive tensile

stresses due to the thermal expansion of the water inside its pores or whether fluid pressures can dissipate quickly enough in relation to heat transport.

As the basis of the subsequent numerical simulations, the governing equations with respect to the coupled thermo-hydro-mechanical processes relevant in the present context will be reviewed. They are given by:

- The mass balance of the entire mixture

$$\text{div}[(u_S)' + \phi_F w_{FS}] = \beta_T^{\text{eff}} T_S' + \phi_F \beta_{TF} \text{grad} T \cdot w_{FS} \tag{11}$$

with

$$\phi_F w_{FS} = -\frac{\kappa_F}{\mu_{FR}} [\text{grad} p - \rho_{FR} \mathbf{g}] \quad \text{and} \tag{12}$$

$$\beta_T^{\text{eff}} = \phi_F \beta_{TF} + 3(1 - \phi_F) \alpha_{TS}$$

- The momentum balance of the entire mixture

$$\text{div}[\sigma_S^E - \alpha_{BP} \mathbf{I}] + \rho^{\text{eff}} \mathbf{g} = \mathbf{0} \tag{13}$$

with the effective stresses σ_S^E and thermal strains ϵ^{th} given as

Table 2 Material properties of the heat exchanger and the filling material

Materials	Density $\rho / (\text{kg m}^{-3})$	Thermal conductivity $\lambda / (\text{W m}^{-1} \text{K}^{-1})$	Thermal expansion $\alpha_T / (\text{K}^{-1} \cdot 10^{-6})$	Heat capacity $c_p / (\text{J kg}^{-1} \text{K}^{-1})$	Young's modulus E / GPa
Heat exchanger					
Aluminium	2700	167.0	23.6	896	68.9
Polyethylene HD	960	0.4	120.0	2200	1.1
Alu-PE composite	1825	0.4	30.0	1261	68.9
Storage material					
Füllbinder L (saturated)	1583	0.96	10.7	2083	1.9
Insulation material					
Styrodur	50	0.034	10.0	1250	–

$$\sigma_S^E = \mathcal{C} : (\epsilon - \epsilon^{th}) \quad \text{and} \quad \epsilon^{th} = \alpha_{TS} \Delta T \quad (14)$$

- The energy balance of the entire mixture

$$(\rho c_p)^{eff} \frac{\partial T}{\partial t} + \phi_F \rho_{FR} c_{pF} \text{grad} T \cdot \mathbf{w}_{FS} - \text{div}[\lambda^{eff} \text{grad} T] \quad (15)$$

where α_{TS} is the linear coefficient of thermal expansion of the solid phase, β_{TF} is the volumetric coefficient of thermal expansion of the fluid phase, ϕ_F is the porosity, κ_F is the intrinsic permeability tensor, μ_{FR} is the fluid viscosity, α_B is the Biot coefficient chosen equal to one here, T is the absolute temperature, p is the pore pressure, λ^{eff} is the effective heat conductivity of the mixture and $(\bullet)'_\alpha$ denotes a material time derivative following the motion of the α^{th} constituent.

Thermomechanical analysis

When reducing the analysis to a purely thermomechanical model, the mixture mass balance does no longer need to be accounted for explicitly and $p = 0$, $\mathbf{w}_{FS} = \mathbf{0}$ can be set in the remaining relations of the above system of equations.

In this section, body forces were not considered. Due to the linearity assumption made throughout, stresses induced by gravity or an overburden can simply be added using the superposition principle. Gravity was considered in the thermo-hydro-mechanical analyses shown below.

An axisymmetric FEM model was implemented in the open-source finite element platform OpenGeoSys (Kolditz et al. 2012) to represent the coupled thermomechanical problem. The entire domain was discretized with 14,701 triangular elements. The simulated time was divided into 540 time steps with a constant time step size of 800 seconds. The initial temperature T_0 in the entire domain was 10 °C. Thermal boundary conditions at the inside walls of the heat exchanger pipes were set to a temperature of 90 °C. The resulting stress distribution was evaluated at different times during the charging phase corresponding to two different surface temperatures T_s of 30 and 90 °C (compare Fig. 4).

Based on the stress distribution illustrated in Fig. 5, the region surrounding the heat exchanger can be identified as the critical region with the highest significance. As expected, peak stresses were observed in this region. It also became apparent that a very fine resolution is required to accurately resolve the gradients and stress jumps at the heat exchanger–cement interface quickly increasing the required computational resources.

Significantly elevated stresses in other regions of the heat store caused by heterogeneous temperature distributions during the charging phase were not observed (Fig. 5).

Note, that due to the axisymmetric analysis, the constraint of the pipe expansion also led to the prediction of high stresses in the axial direction of the pipe (circumferential direction of the test rig, Fig. 5b). To what degree such stresses develop in the actual equipment depends both on interface friction and on the integration of the pipes in the overall set-up. Often, if no fins are attached to the heat exchangers, this stress will be relieved by interface slip as evidenced by typically occurring damage patterns. This issue will be discussed further in “Analytical solution in the near field of the heat exchanger” section.

Thermo-hydro-mechanical analysis

The fluid pressures predicted from thermo-hydro-mechanical analyses naturally depend significantly on the boundary conditions imposed on the fluid domain. In the extreme, fluid cannot escape the porous domain through any of its boundaries, thereby causing very high fluid pressures as a consequence of the high bulk modulus of most liquids. This extreme case can be described by an analytical solution for the fluid pressure created by the thermally induced volume expansion in a porous medium.

The effective volumetric coefficient of thermal expansion from Eq. (12) is the basis for calculating the volumetric strain of the mixture

$$e_M = \beta_{TM} \Delta T \quad (16)$$

Under externally load-free conditions, the fluid pressure is balanced only by effective stresses. Thus, on finds

$$p = -K_S (e_M - e^{th}) \quad (17)$$

$$= -K_S \phi_F (\beta_{TF} - \beta_{TS}) \Delta T \quad (18)$$

The fluid phase in the model is considered as water, with the volumetric coefficient of thermal expansion of $2.07 \cdot 10^{-4} \text{ K}^{-1}$.

Under undrained conditions, a freely expanding material with the properties from Table 2 undergoing a temperature increase by 80 K reaches a fluid pressure of 7.33 MPa. This pressure is balanced by tensile normal stresses of equal magnitude which exceeds typical tensile strength values of cementitious materials by far.

This result illustrates that fluid pressurization manifesting itself as tension in the solid skeleton has the potential to cause microcracks throughout the heated domain if the fluid cannot migrate out of the high-pressure zones quickly enough. It represents a potentially damaging effect in addition to the phenomena caused by the heat exchangers. The estimate based on Eq. (18) is an absolute upper bound which will be lowered not only by fluid migration ($\kappa_F > 0$) out of heated domains but also by a Biot coefficient lower than 1.

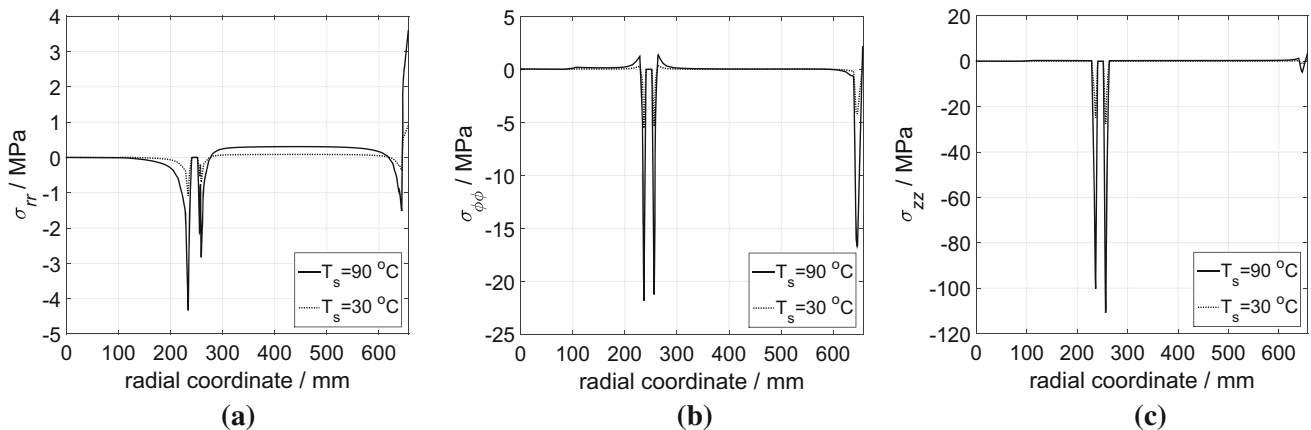
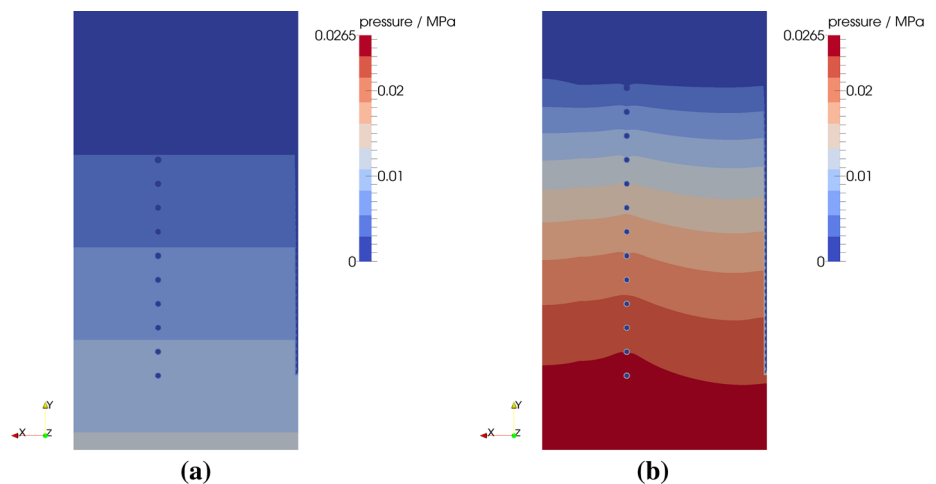


Fig. 5 Radial, circumferential and axial stresses along the dashed radial line traversing the test rig as indicated in Fig. 4. The stress profiles clearly identify the heat exchanger–cement interface as the

main region of interest. **a** Stress component σ_{rr} . **b** Stress component $\sigma_{\phi\phi}$. **c** Stress component σ_{zz}

Fig. 6 Excess fluid pressure distribution when fluid is allowed to drain through the unsealed top surface. **a** Fluid pressure profile due to gravity before and after heating. **b** Peak fluid pressurization during the charging of the heat store



To obtain a quantitative estimate of fluid pressurization for the boundary conditions representative of the test rig studied here, a numerical simulation of the test rig under drained conditions was conducted.

The fluid is assumed to drain through the unsealed top boundary. Based on laboratory measurements, an isotropic permeability of 10^{-14} m^2 was assigned to the cement. The other boundary conditions remained as described in the previous section.

Figure 6 highlights two characteristic states of fluid pressurization. In Fig. 6a, the excess fluid pressurization before heating shows the characteristic stratification with depth resulting from gravity. During the heating process, fluid expands, locally causes pressure increases and exudes through the draining boundary at the top of the domain. The intrinsic permeability of 10^{-14} m^2 was sufficient to maintain a low excess fluid pressurization on the order of 20 kPa, compare Fig. 6b. Two locations, one towards the bottom of the heat store and one near the

top, were selected to illustrate the pressure transients in the different regions of the heat store during the charging period. It can be seen clearly (Fig. 7) that the peak pressure arises during the initial stage of the heating process and drops off to a lower level as fluid is moved and eventually lost from the heat store. Once the entire heat store is heated up, fluid pressurization has returned to levels very close to the original stratification (Figs. 6a, 7).

Analytical solution in the near field of the heat exchanger

As shown in “Numerical simulations of a test rig for system development”, spatial stresses occur around the heat exchanger pipes and are characterized by strong gradients. A detailed analysis can be achieved numerically, albeit with a high-resolution grid, or analytically. The latter has

Fig. 7 Variation of the fluid pressurization during the charging period at two different locations in the heat store. **a** Variation of the fluid pressure in two locations. **b** The illustration of the two locations in the test rig

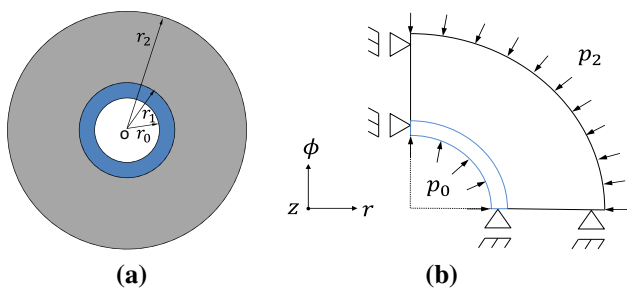
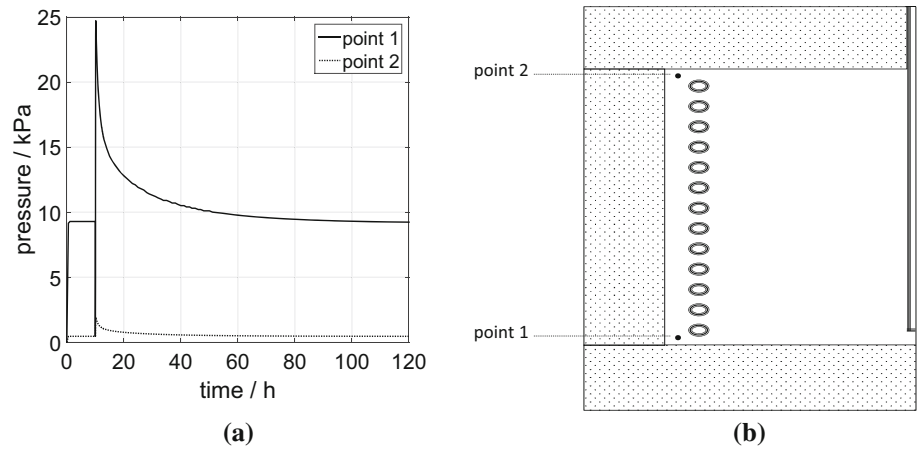


Fig. 8 Schematic view and boundary conditions of a plane region characterizing the vicinity of the heat exchanger. **a** Geometry of the annular region around the heat exchanger. **b** Boundary conditions imposed onto the model domain

the advantage of illustrating the process more clearly, of being faster, easier to use and more robust.

An analytical solution was therefore derived for the mentioned critical region comprising the heat exchanger and the surrounding filling material assuming the region around the pipes to be axisymmetric (see Fig. 8). As seen in the “Numerical simulations of a test rig for system development” section, the cement is approximately under plane stress conditions in most parts as indicated by the low circumferential stresses (axial stresses in the detailed model) in Fig. 5b. As mentioned previously, depending on the actual constraints imposed onto the system the ideal plane stress setting can be disturbed. Thus, analytical solutions were developed for both plane strain and plane stress conditions which can be considered as limiting cases.

The specific model description including geometry and boundary conditions is plotted in Fig. 8. The derivation is based on cylindrical coordinates (radius r , polar angle ϕ , axial coordinate z).

Basic equations

All materials have been assumed to behave linearly elastic. Stresses predicted can then be compared to strength or

yield criteria as appropriate for the given materials in a straight forward manner. If the elastic solution exceeds such a criterion, local failure of the structure can be inferred. The thermoelastic problem can be derived by the following equations:

The assumption of axisymmetry entails the conditions

$$\sigma_{r\phi} = \sigma_{rz} = \sigma_{\phi z} = 0 \tag{19}$$

$$\epsilon_{r\phi} = \epsilon_{rz} = \epsilon_{\phi z} = 0 \tag{20}$$

$$u_{\phi} = 0 \tag{21}$$

$$(\bullet)_{,\phi} = 0 \tag{22}$$

where the comma operator means the partial derivative of a quantity $(\bullet)_{,a} = \partial(\bullet)/\partial a$.

The kinematic relationship $\epsilon = \text{sym grad } \mathbf{u}$ simplifies under the above conditions to the following nonzero strain coordinates

$$\epsilon_{rr} = u_{r,r} \tag{23}$$

$$\epsilon_{\phi\phi} = \frac{u_r}{r} \tag{24}$$

$$\epsilon_{zz} = u_{z,z} \neq 0 \text{ and } \sigma_{zz} = 0 \text{ for plane stress} \tag{25}$$

$$\epsilon_{zz} = 0 \text{ and } \sigma_{zz} \neq 0 \text{ for plane strain} \tag{26}$$

Local quasistatic mechanical equilibrium in the absence of body forces is given by $\text{div } \boldsymbol{\sigma} = \mathbf{0}$. Under the above assumptions, the following relations remain:

$$0 = \sigma_{rr,r} + \frac{1}{r}(\sigma_{rr} - \sigma_{\phi\phi}) = 0 \tag{27}$$

$$0 = \sigma_{zz,z} \tag{28}$$

The latter relation shows that the axial stress is constant throughout the thickness for plane strain conditions.

Stresses and strains as well as temperature changes are linked via constitutive relationships, given in the present case by the linear thermoelastic relation

$$\boldsymbol{\sigma} = \mathbf{C} : (\boldsymbol{\epsilon} - \boldsymbol{\alpha}\vartheta) \tag{29}$$

where C is the fourth order stiffness tensor and α is the tensor of linear thermal expansion and $\vartheta = \Delta T = T(r) - T_0$ the temperature difference with respect to a reference temperature T_0 . Assuming isotropy, we find for axisymmetric conditions:

Plane strain:

$$\epsilon_{rr} = \frac{1}{\bar{E}} (\sigma_{rr} - \bar{\nu}\sigma_{\phi\phi}) + \bar{\alpha}\vartheta \tag{30}$$

$$\epsilon_{\phi\phi} = \frac{1}{\bar{E}} (\sigma_{\phi\phi} - \bar{\nu}\sigma_{rr}) + \bar{\alpha}\vartheta \tag{31}$$

$$\epsilon_{zz} = 0 \tag{32}$$

$$\sigma_{zz} = \frac{\bar{E}\nu [(\epsilon_{rr} + \epsilon_{\phi\phi}) - 2\bar{\alpha}\vartheta]}{1 - \bar{\nu}} - E\alpha\vartheta \tag{33}$$

Plane stress:

$$\epsilon_{rr} = \frac{1}{E} (\sigma_{rr} - \nu\sigma_{\phi\phi}) + \alpha\vartheta \tag{34}$$

$$\epsilon_{\phi\phi} = \frac{1}{E} (\sigma_{\phi\phi} - \nu\sigma_{rr}) + \alpha\vartheta \tag{35}$$

$$\epsilon_{zz} = -\frac{\nu}{E} (\sigma_{rr} + \sigma_{\phi\phi}) + \alpha\vartheta \tag{36}$$

$$\sigma_{zz} = 0 \tag{37}$$

where $\bar{E} = \frac{E}{1-\nu^2}$, $\bar{\nu} = \frac{\nu}{1-\nu}$, $\bar{\alpha} = (1+\nu)\alpha$ represent material properties under plane strain conditions. Furthermore, E is the Young's modulus, ν is the Poisson's ratio, and α is the linear thermal expansion coefficient.

Based on the above, the stress compatibility equation can be obtained:

$$\nabla^2 (\sigma_{rr} + \sigma_{\phi\phi}) = 0 \tag{38}$$

where $\Delta = \nabla^2 = \nabla \cdot \nabla = \frac{\partial^2}{\partial r^2} + \frac{1}{r} \frac{\partial}{\partial r} + \frac{1}{r^2} \frac{\partial^2}{\partial \phi^2}$ is the potential operator in polar coordinates.

Expressing the stress coordinates by a scalar valued so-called Airy stress function φ (Kreißig and Benedix (2013)) via

$$\sigma_{rr} = \frac{1}{r} \varphi_{,r} + \frac{1}{r^2} \varphi_{,\phi\phi} \tag{39}$$

$$\sigma_{\phi\phi} = \varphi_{,rr} \tag{40}$$

$$\sigma_{zz} = \nu \left(\frac{1}{r} \varphi_{,r} + \varphi_{,rr} + \frac{1}{r^2} \varphi_{,\phi\phi} \right) - E\alpha\vartheta \tag{41}$$

$$\sigma_{r\phi} = - \left(\frac{1}{r} \varphi_{,\phi} \right)_{,r} \tag{42}$$

allows the stress compatibility equation to be rewritten as a bipotential equation.

$$\Delta\Delta\varphi = 0, \tag{43}$$

For axisymmetric problems under either plane strain or plane stress, the stress function φ is only dependent on r . Equation (43) therefore becomes an ordinary differential equation of the form

$$\left\{ r \left[\frac{1}{r} (r\varphi_{,r})_{,r} \right]_{,r} \right\}_{,r} = 0. \tag{44}$$

Boundary and interface conditions

Considering a two-layered ring composed of two linear thermoelastic materials, the outer material has an outer radius r_2 and an inner radius r_1 , and the inner has an outer radius r_1 and an inner radius r_0 (see Fig. 8a). The boundary value problem is completed by two boundary conditions and two continuity requirements at the interface expressed as

$$u_r^1|_{r_1} = u_r^2|_{r_1} \tag{45}$$

$$\sigma_{rr}^1|_{r_1} + \sigma_{rr}^2|_{r_1} = 0 \tag{46}$$

$$\sigma_{rr}^1|_{r_0} = -p_0 \tag{47}$$

$$\sigma_{rr}^2|_{r_2} = -p_2 \tag{48}$$

where superscripts 1, 2 indicate the inner and outer material of the model, respectively.

Stress and displacement expressions

The solution will be derived for the plane strain case. The result can be easily transformed to plane stress conditions as will be shown later.

Substituting the general solution of Eq. (44) into Eqs. (39)–(42), and involving the radial momentum balance for axisymmetric conditions from Eq. (27), the stress components can be written as:

For $r_0 < r < r_1$ (inner ring):

$$\sigma_{rr}^1 = \frac{A_1}{r^2} + 2C_1 \tag{49}$$

$$\sigma_{\phi\phi}^1 = -\frac{A_1}{r^2} + 2C_1 \tag{50}$$

$$\sigma_{zz}^1 = 4\bar{\nu}_1 C_1 - E_1 \bar{\alpha}_1 \vartheta_1 \tag{51}$$

For $r_1 < r < r_2$ (outer ring):

$$\sigma_{rr}^2 = \frac{A_2}{r^2} + 2C_2 \tag{52}$$

$$\sigma_{\phi\phi}^2 = -\frac{A_2}{r^2} + 2C_2 \tag{53}$$

$$\sigma_{zz}^2 = 4\bar{\nu}_2 C_2 - E_2 \bar{\alpha}_2 \vartheta_2 \tag{54}$$

Then, substituting Eqs. (49)–(51) and (52)–(54) into Eqs. (30)–(33) yields strain components. Finally, using the

kinematic relationships, the radial displacement u_r can be obtained:

$$u_r^1 = \frac{1}{\bar{E}_1} \left[-(1 + \bar{\nu}_1) \frac{A_1}{r} + 2(1 - \bar{\nu}_1) C_1 r \right] + \bar{\alpha}_1 (\psi_1(r) - T_0 r)$$

with $r_0 \leq r \leq r_1$ (55)

$$u_r^2 = \frac{1}{\bar{E}_2} \left[-(1 + \bar{\nu}_2) \frac{A_2}{r} + 2(1 - \bar{\nu}_2) C_2 r \right] + \bar{\alpha}_2 (\psi_2(r) - T_0 r)$$

with $r_1 \leq r \leq r_2$ (56)

where $\psi(r) = \int T(r) dr$.

Based on the continuity and boundary conditions expressed in Eqs. (45)–(48), the four undetermined constants A_1, A_2, C_1, C_2 can be determined,

$$A_1 = \frac{\bar{E}_2(1 - \bar{\nu}_1)r_0^2r_1^2r_2^2p_0 + \bar{E}_1r_0^2[-r_1^2r_2^2p_2 - R_1(r_1^2 + r_2^2)] + \bar{E}_1\bar{\nu}_2r_0^2[r_1^2r_2^2p_2 + R_1(r_1^2 - r_2^2)]}{\bar{E}_1r_0^2R_0[r_2^2 + r_1^2 + \bar{\nu}_2(r_2^2 - r_1^2)] - \bar{E}_2r_2^2[r_0^2 + r_1^2 + \bar{\nu}_1(r_0^2 - r_1^2)]} \tag{57}$$

$$+ \frac{\bar{E}_1\bar{E}_2r_0^2r_1r_2^2[\bar{\alpha}_2(\psi_2(r)|_{r_1} - r_1T_0) - \bar{\alpha}_1(\psi_1(r)|_{r_1} - r_1T_0)]}{\bar{E}_1r_0^2R_0[r_2^2 + r_1^2 + \bar{\nu}_2(r_2^2 - r_1^2)] - \bar{E}_2r_2^2[r_0^2 + r_1^2 + \bar{\nu}_1(r_0^2 - r_1^2)]} \tag{58}$$

$$A_2 = R_0A_1 + R_1 \tag{59}$$

$$C_1 = -\frac{1}{2} \left(p_0 + \frac{A_1}{r_0^2} \right) \tag{60}$$

$$C_2 = -\frac{1}{2} \left(p_2 + \frac{A_2}{r_2^2} \right) \tag{61}$$

where $R_0 = \frac{r_2^2(r_0^2 - r_1^2)}{r_0^2(r_1^2 - r_2^2)}$ and $R_1 = -\frac{r_1^2r_2^2(p_0 + p_2)}{r_1^2 - r_2^2}$.

Substituting E, ν, α for $\bar{E}, \bar{\nu}, \bar{\alpha}$, the stress components and the radial displacement for plane stress conditions can be obtained.

Comparison of analytical and numerical solution

First, the analytical plane strain solution is compared with the results presented in Skinner et al. (2014). All required parameters were taken directly from that reference. The heat exchanger and filling material were both heated to 300, 400 and 500 °C, respectively.

The maximum tensile stress in dependence of the temperature lift is shown in Fig. 9. It can be seen that the analytical solution recovers the results shown in Skinner et al. (2014) with merely small differences.

The analytical solution is now compared against numerical results obtained using OpenGeoSys.

Values of geometric dimensions and temperature values have been based on the test rig described in the section “Numerical simulations of a test rig for system

development” and were set to $r_2 = 35$ mm, $r_1 = 12.5$ mm, $r_0 = 10$ mm. The ambient temperature is 10 °C and was taken as the reference value T_0 . The heat exchanger and the filling material were both heated to 90 °C. Arbitrary values were chosen for the boundary pressures and are only relevant to test the analytical solution in its entirety. They were set to $p_0 = 2$ MPa and $p_2 = 1$ MPa. Material properties are given in Table 2. Meshes with 2301 (Fig. 10a) and 1390 (Fig. 10b) quadrilateral biquadratic isoparametric elements were used for numerical models. The time step size was set to 60 s.

Figure 11 shows the stress and displacement distribution along the radial direction of the model for plane strain conditions. It can be seen that on account of the different

physical properties of the two materials, changes in the slope appear for radial stress and displacement, while a jump in the curve for the circumferential and axial stress appears at the interface. Maximum tensile stresses occur in the circumferential direction within the filling material at the interface due to the expansion of the pipe within the filling material caused by the difference of thermal expansion coefficients between both materials. Maximum compressive stresses occur at the inner boundary of the heat exchanger. Overall, the analytical and numerical solutions fit very well.

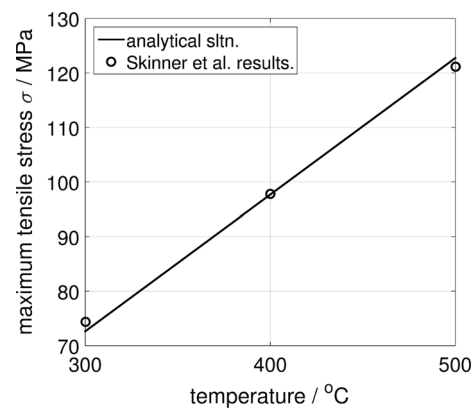


Fig. 9 Comparison of the maximum tensile stress. The horizontal coordinate represents temperature which the test model must be heated to. The reference temperature is 10 °C

Fig. 10 Finite element discretization of the numerical models. **a** Plane strain model. **b** Axisymmetric model

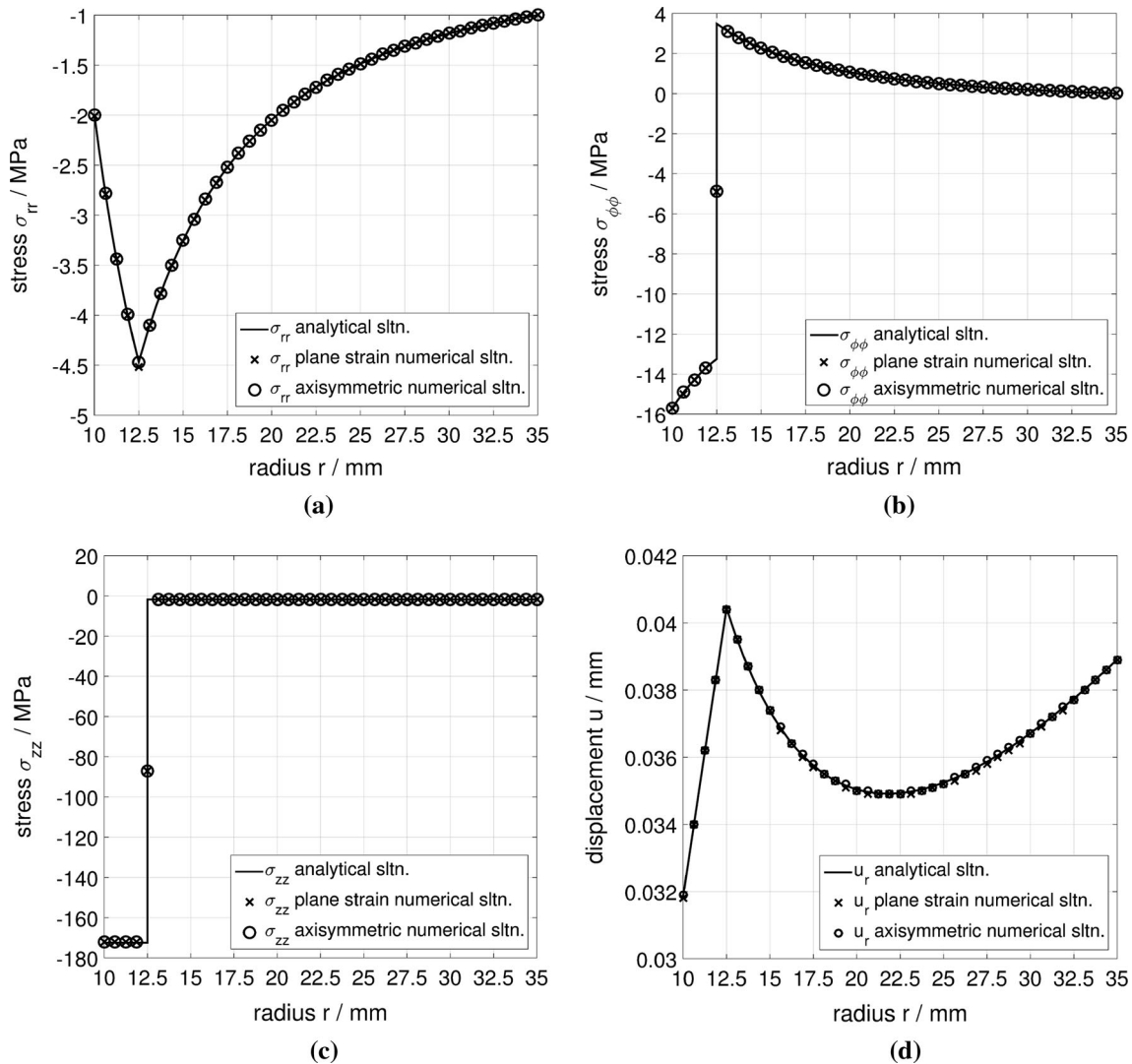
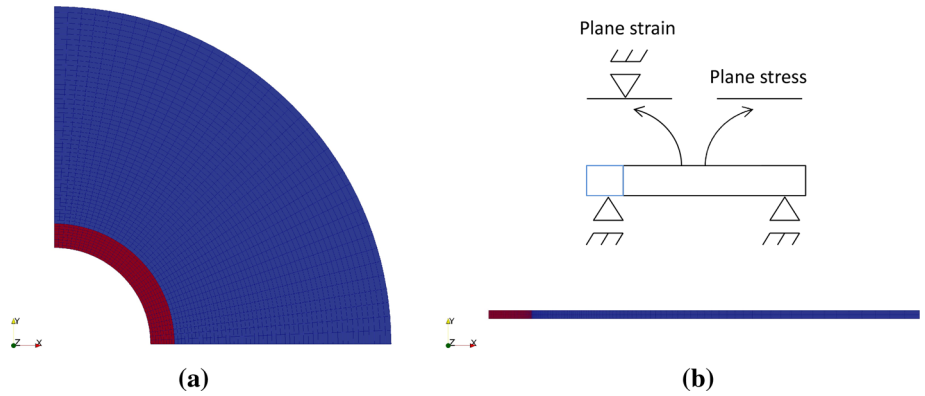


Fig. 11 Principal stress distribution and radial displacement along the radius for plane strain. The aluminium–polyethylene composite pipe is used as the heat exchanger. **a** Radial stress distribution. **b** Circumferential stress distribution. **c** Axial stress distribution. **d** Radial displacement

For comparison, a plane stress analysis has been implemented under the same loading conditions (see Fig. 12). While the analytical solution assumes perfect plane stress conditions for both material regions corresponding to

frictionless contact between the layers, the plane stress state is disturbed due to the glued interface in the numerical model. Therefore, a soft continuum-element layer, with the thickness of 0.1 mm, an elastic modulus 100 times lower

than that of the filling material and a Poisson’s ratio of 0.45, was placed at the interface of the heat exchanger and the filling material to provide stress relief and decrease stress oscillations. The results in Fig. 12a highlight that the layer has the desired effect and the numerical model is very close to plane stress conditions. As an additional confirmation, the simulation was repeated with a numerical model in which the interface was represented by frictionless sliding contact formulation which reproduced plane stress conditions very accurately (data not shown). As the soft layer acts as a cushion, there is a displacement drop between inside and outside ring (Fig. 12b).

Sensitivity analysis

In the actual system, the thermal and mechanical properties of materials will vary due to manufacturing variability and due to a possible deterioration during service life. The sensitivity analyses are aimed at investigating the impact of key material parameters on the development of peak stresses. The thermal expansion coefficient and Young’s modulus of the filling material are taken into account in combination with the three heat exchanger materials examined in the IGLU project. The sensitivity analyses are based on the analytical solution developed in “Analytical solution in the near field of the heat exchanger”.

Pipe material

In order to determine the influence of the heat exchanger material on the peak stresses occurring in the system, three possible materials were selected and compared regarding

their effect on the stress distribution. Physical properties for the heat exchanger and the filling material are listed in Table 2.

The calculation results are provided in Table 3 for a temperature lift of $\Delta T = 80$ K, no pressures imposed on the boundaries, while the thermal expansion coefficient of the filling material was varied by setting it to the following values: $\alpha_c = 10 \cdot 10^{-6}$, $15 \cdot 10^{-6}$, $20 \cdot 10^{-6}$, $30 \cdot 10^{-6}$.

Zero values in Table 3 infer that if the cement expands faster than the heat exchanger, contact is lost and no stresses are created. Based on the available data, the high-density polyethylene heat exchanger causes the highest stresses in both plane strain and plane stress conditions. Stresses can be observed to decrease with the increase in the thermal expansion coefficient of the filling material. The influence of the thermomechanical properties of the cement on the peak stresses will be investigated further in the next section.

Filling material

As stated in Table 3, the thermal expansion coefficient has a significant influence on the stress distribution. The Young’s modulus of the filling material is another determinant of the stress state and will be included in the sensitivity analysis here. The analysis is performed for the three heat exchanger materials considered as options in the IGLU project.

The thermal expansion coefficient of the filling material was varied in a constant region from zero up to the values of the different heat exchanger materials at which point contact is lost under plane stress conditions.

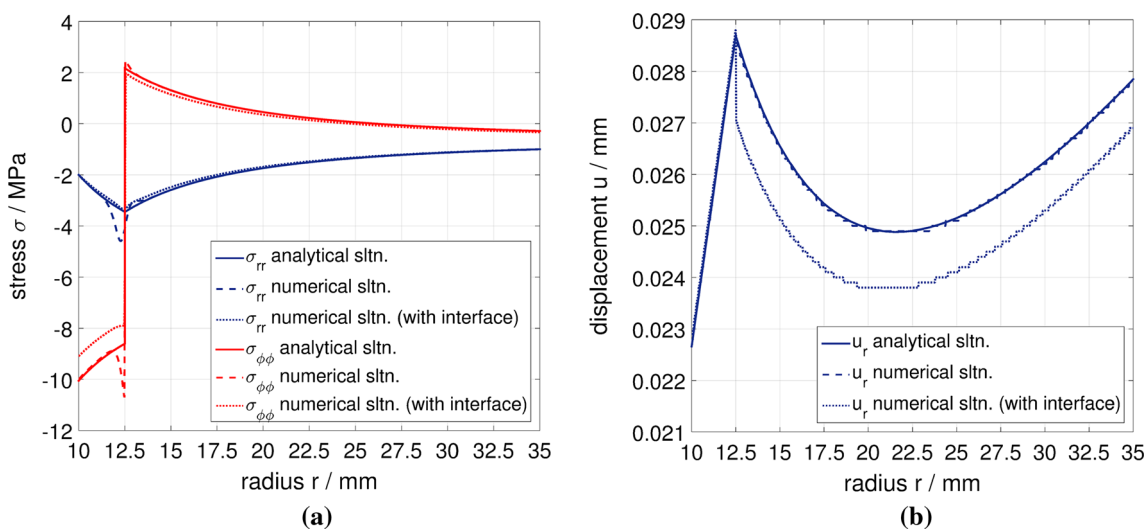


Fig. 12 Principal stress distribution and radial displacement along the radius for plane stress. The aluminium–polyethylene composite pipe is used as the heat exchanger. **a** Stress distribution. **b** Radial displacement

Table 3 Results for maximum compressive (heat exchanger) and maximum tensile (cement) stresses for three different heat exchanger materials and a range of thermal expansion coefficients of the cement

α_c / K^{-1}	Peak compressive stresses/MPa				Peak tensile stresses/MPa			
	$10 \cdot 10^{-6}$	$15 \cdot 10^{-6}$	$20 \cdot 10^{-6}$	$30 \cdot 10^{-6}$	$10 \cdot 10^{-6}$	$15 \cdot 10^{-6}$	$20 \cdot 10^{-6}$	$30 \cdot 10^{-6}$
Plane strain								
Aluminium	-11.05	-7.85	-4.66	0	2.57	1.83	1.08	0
Polyethylene HD	-18.62	-17.92	-17.23	-15.83	4.33	4.17	4.01	3.68
Alu-PE composite	-16.66	-13.44	-10.23	-3.79	3.88	3.13	2.38	0.88
Plane stress								
Aluminium	-7.53	-4.84	-2.15	0	1.75	1.12	0.5	0
Polyethylene HD	-10.76	-10.27	-9.78	-8.80	2.50	2.39	2.28	2.05
Alu-PE composite	-10.77	-8.08	-5.38	0	2.50	1.88	1.25	0

α_c represents the thermal expansion coefficient of the cement

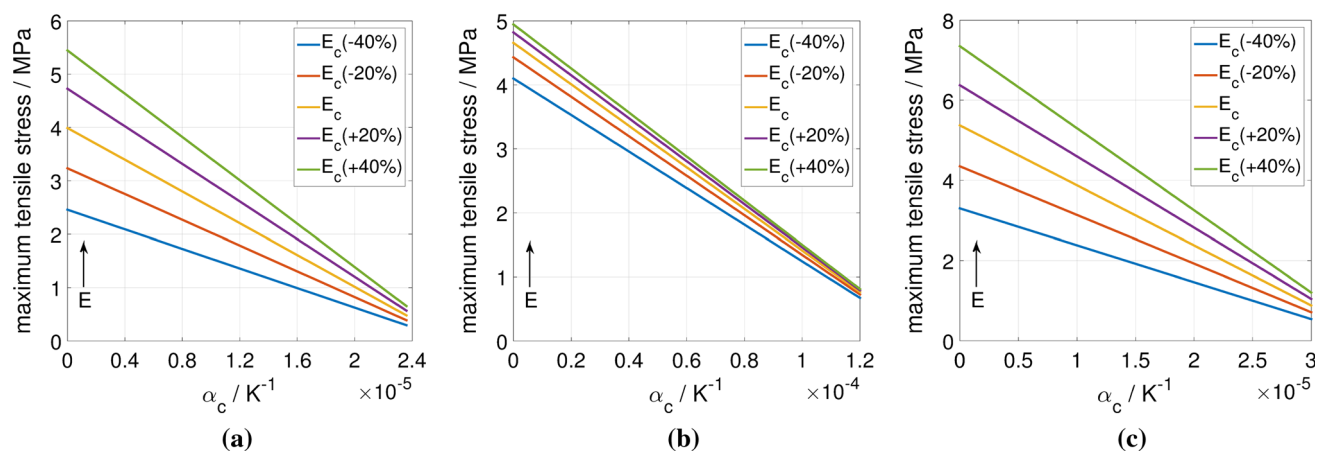


Fig. 13 Maximum tensile stress in the cement under plane strain conditions. α_c is the thermal expansion coefficient of the cement. In Figs. 13, 14, 15 and 16, the black arrow always points into the

direction of increasing elastic modulus. **a** $\alpha_{\text{Alu}} = 23.6 \cdot 10^{-6} \text{K}^{-1}$. **b** $\alpha_{\text{PE}} = 120 \cdot 10^{-6} \text{K}^{-1}$. **c** $\alpha_{\text{Alu-PE}} = 30 \cdot 10^{-6} \text{K}^{-1}$

The Young's moduli were varied by ± 20 and ± 40 % based on the reference value given in Table 2. Figures 13, 14, 15 and 16 show that stresses vary linearly with the thermal expansion coefficient across a significant range. Generally, stresses decrease with increasing the thermal expansion coefficient of the filling material. Similarly, stresses increase with increasing the elastic modulus of the filling material. Both results are expected for a linear thermoelastic material. In addition to these general features, one aspect presented in Figs. 13, 14, 15 and 16 is worth noting: The Young's modulus has a less drastic effect in the scenario where the polyethylene pipe was chosen as the heat exchanger material. It also becomes clear that an accurate estimate of the stress distribution requires accurate values for the thermal expansion coefficients. The stiffer the cement, the more will inaccuracies of α affect the stress result.

Conclusions and discussions

In this paper, a novel sensible heat store based on water-saturated cement was studied by thermo-hydro-mechanical modeling using the open-source finite element platform OpenGeoSys. Based on a numerical assessment of the fully coupled THM process, it could be shown that fluid pressure-induced stresses can reach very high magnitudes if the fluid cannot escape or cannot escape quickly enough. For the permeability values of the cement studied here, this problem does not arise, as evidenced by maximum excess pressures on the order of tens of kPa. Therefore, the subsequent analyses were restricted to thermomechanical problems where the fluid phase was accounted for only via the effective properties but not as a kinematically independent phase.

An analytical solution was derived to estimate the thermally induced stresses in a cement-based sensible heat

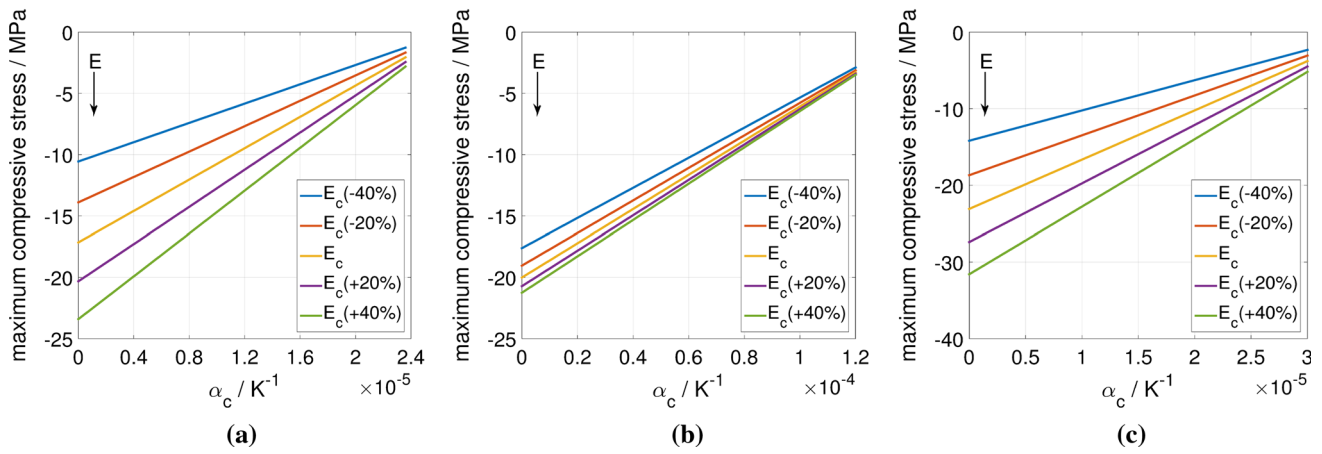


Fig. 14 Maximum compressive stress in the pipe for plane strain conditions. **a** $\alpha_{Alu} = 23.6 \cdot 10^{-6} K^{-1}$. **b** $\alpha_{PE} = 120 \cdot 10^{-6} K^{-1}$. **c** $\alpha_{Alu-PE} = 30 \cdot 10^{-6} K^{-1}$

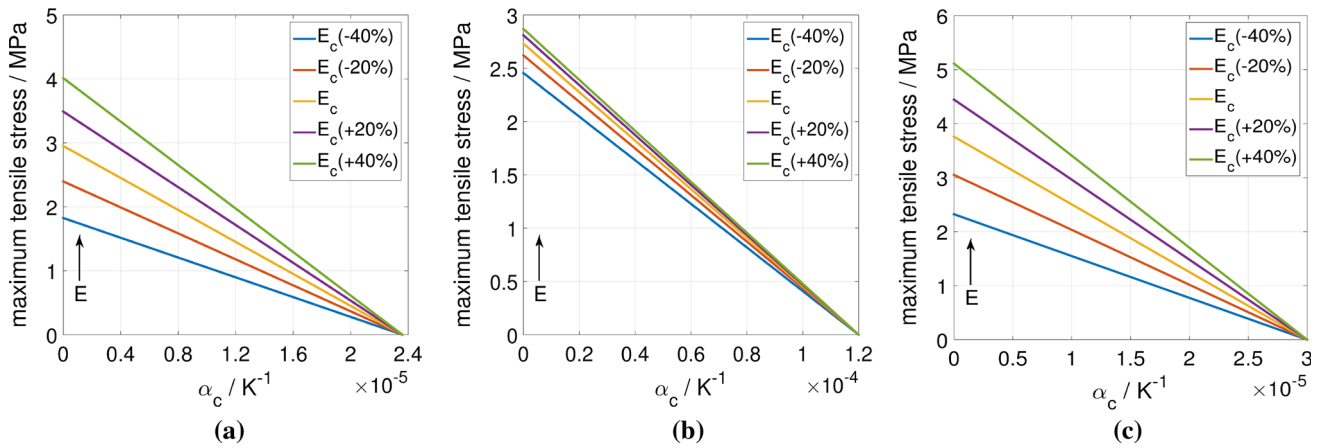


Fig. 15 Maximum tensile stress in the cement for plane stress conditions. **a** $\alpha_{Alu} = 23.6 \cdot 10^{-6} K^{-1}$. **b** $\alpha_{PE} = 120 \cdot 10^{-6} K^{-1}$. **c** $\alpha_{Alu-PE} = 30 \cdot 10^{-6} K^{-1}$

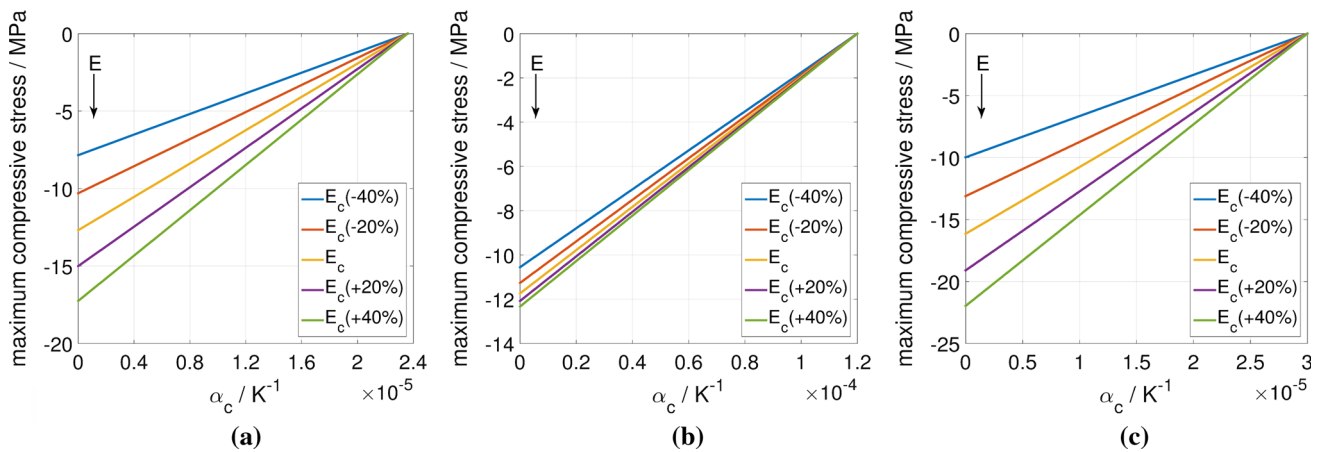


Fig. 16 Maximum compressive stress in the pipe for plane stress conditions. **a** $\alpha_{Alu} = 23.6 \cdot 10^{-6} K^{-1}$. **b** $\alpha_{PE} = 120 \cdot 10^{-6} K^{-1}$. **c** $\alpha_{Alu-PE} = 30 \cdot 10^{-6} K^{-1}$

store, especially, in the critical region around the heat exchangers. The critical region was justified by a simulation of the charging phase of the entire heat store which revealed these critical regions as the most likely to fail. The analytical solution is a robust method which can quickly provide a basic screening of materials and design parameters in relation to the stresses. The analytical solution was verified by numerical simulations. The analytical solution was used to quantify peak stresses, which can be compared to strength criteria of the used materials to predict whether local failure is likely to occur. Both plane strain and plain stress conditions were analysed. The relevance of either of those idealizations depends on the actual constraints imposed onto the system, or the actual interfacial contact conditions prevalent on the interface between the pipe and the cement. Based on the numerical simulation of the charging phase, the cement was observed to experience near-plane stress conditions in most parts for the set-up studied here.

In addition, a sensitivity analysis was performed to determine the main factors affecting the stress distribution. Stresses decreased with either increasing the thermal expansion coefficient or decreasing the elastic modulus of the filling material. The sensitivity analysis can also provide basic criteria for selecting materials that compromise between mechanical and economic considerations or for optimising heat exchanger layouts. The significance of the thermal expansion coefficient on the stress magnitudes implies that the quality of the predictions made based on a thermomechanical analysis particularly depends on the accuracy with which the thermal expansion coefficients of the involved materials have been determined experimentally.

Although high stresses occur when using a heat exchanger made of aluminium–polyethylene composite, for long-term application, aluminium–polyethylene composite may remain an option. Not only does it have a more stronger corrosion resistance against electrochemical insults by the environment, but it also combines other advantages of the pure aluminium alloy and polyethylene pipes, such as specific strength. Due to the low tensile strength of the filling material considered here, cracks are likely to form surrounding the heat exchangers. Technically, the excessive tensile stress can be relieved by pre-processing the surrounding filling material during the construction phase. For that purpose, the system would be heated up while the cement is still curing, thus plastically deforming the cement and allowing the pipes to expand freely during operational heating cycles. If the gap this procedure would create between the pipe and the cement would be filled by water it would not limit the thermal performance severely. Since the prescribed water-saturated cement is used as the filling material, the energy storage capacity is maintained at a high level. Currently, the

analyses are extended to the optimisation of heat exchanger layouts as well as to inelastic effects occurring in the filling material and multiphase flow within the pore space.

Acknowledgments Funding was provided by the Federal Ministry of Economic Affairs and Energy under Grant no. 0325547C (IGLU project) and is gratefully acknowledged.

References

- Abhat A (1983) Low temperature latent heat thermal energy storage: heat storage materials. *Sol Energy* 30(4):313–332
- Abramowitz M, Stegun IA (1972) Handbook of mathematical functions. ninth printing
- Agyenim F, Eames P, Smyth M (2010a) Heat transfer enhancement in medium temperature thermal energy storage system using a multitube heat transfer array. *Renew Energy* 35(1):198–207
- Agyenim F, Hewitt N, Eames P, Smyth M (2010b) A review of materials, heat transfer and phase change problem formulation for latent heat thermal energy storage systems (lhtess). *Renew Sustain Energy Rev* 14(2):615–628
- ASTM (2006) ASTM E831-06, Standard test method for linear thermal expansion of solid materials by thermomechanical analysis. ASTM E831-06
- ASTM (2008) ASTM D5334-08, Standard test method for determination of thermal conductivity of soil and soft rock by thermal needle probe procedure. ASTM D5334-08
- Bauer D, Marx R, Nußbicker-Lux J, Ochs F, Heidemann W, Müller-Steinhagen H (2010) German central solar heating plants with seasonal heat storage. *Sol Energy* 84(4):612–623
- Bauer D, Marx R, Nußbicker-Lux J, Ochs F, Drücker H, Heidemann W (2013) Forschungsbericht zum BMU-Vorhaben Solarthermie2000plus: Wissenschaftlich-technische Begleitung des Förderprogramms Solarthermie2000plus zu solar unterstützter Nahwärme und Langzeit-Wärmespeicherung. Institut für Thermodynamik und Wärmetechnik, Universität Stuttgart, Stuttgart
- Braun JE, Klein S, Mitchell J (1981) Seasonal storage of energy in solar heating. *Sol Energy* 26(5):403–411
- Carlsaw HS, Jaeger JC (1959) Conduction of heat in solids, 2nd edn. Clarendon Press, Oxford
- Carson J, Moses H (1963) The annual and diurnal heat-exchange cycles in upper layers of soil. *J Appl Meteorol* 2(3):397–406
- Dincer I, Dost S, Li X (1997) Performance analyses of sensible heat storage systems for thermal applications. *Int J Energy Res* 21(12):1157–1171
- Duffy A, Rogers M, Ayompe L (2015) Renewable energy and energy efficiency: assessment of projects and policies. Wiley, New York
- Forster M (2004) Theoretical investigation of the system SnO_2/Sn for the thermochemical storage of solar energy. *Energy* 29(5):789–799
- Gil A, Medrano M, Martorell I, Lazaro A, Dolado P, Zalba B, Cabeza LF (2010) State of the art on high temperature thermal energy storage for power generation. Part 1—concepts, materials and modellization. *Renew Sustain Energy Rev* 14(1):31–55
- Hähnlein S, Bayer P, Ferguson G, Blum P (2013) Sustainability and policy for the thermal use of shallow geothermal energy. *Energy Policy* 59:914–925
- Hasnain S (1998) Review on sustainable thermal energy storage technologies, part i: heat storage materials and techniques. *Energy Convers Manag* 39(11):1127–1138
- Hauer A, Specht M, Sterner M (2010) Energiespeicher—steigerung der energieeffizienz und integration erneuerbarer energien. Report Themen, pp 110–114

- Herrmann U, Kearney DW (2002) Survey of thermal energy storage for parabolic trough power plants. *J Sol Energy Eng* 124(2):145–152
- Herrmann U, Kelly B, Price H (2004) Two-tank molten salt storage for parabolic trough solar power plants. *Energy* 29(5):883–893
- Hesaraki A, Holmberg S, Haghightat F (2015) Seasonal thermal energy storage with heat pumps and low temperatures in building projects—a comparative review. *Renew Sustain Energy Rev* 43:1199–1213
- IEEE (1992) IEEE 442, Guide for soil thermal resistivity measurements. Institute of Electrical and Electronics Engineers. Inc., New York
- Jänchen J, Ackermann D, Stach H, Brösicke W (2004) Studies of the water adsorption on zeolites and modified mesoporous materials for seasonal storage of solar heat. *Sol Energy* 76(1):339–344
- Jian Y, Bai F, Falcoz Q, Xu C, Wang Y, Wang Z (2015a) Thermal analysis and design of solid energy storage systems using a modified lumped capacitance method. *Appl Therm Eng* 75:213–223
- Jian Y, Falcoz Q, Neveu P, Bai F, Wang Y, Wang Z (2015b) Design and optimization of solid thermal energy storage modules for solar thermal power plant applications. *Appl Energy* 139:30–42
- John E, Hale M, Selvam P (2013) Concrete as a thermal energy storage medium for thermocline solar energy storage systems. *Sol Energy* 96:194–204
- Khudhair AM, Farid MM (2004) A review on energy conservation in building applications with thermal storage by latent heat using phase change materials. *Energy Convers Manag* 45(2):263–275
- Kim S, Drzal LT (2009) High latent heat storage and high thermal conductive phase change materials using exfoliated graphite nanoplatelets. *Sol Energy Mater Sol Cells* 93(1):136–142
- Kluitenberg G, Ham J, Bristow KL (1993) Error analysis of the heat pulse method for measuring soil volumetric heat capacity. *Soil Sci Soci Am J* 57(6):1444–1451
- Kolditz O, Görke UJ, Shao H, Wang W (2012) Thermo-hydro-mechanical-chemical processes in porous media: benchmarks and examples, vol 86. Springer Science & Business Media, New York
- Kreißig R, Benedix U (2013) Höhere technische Mechanik: Lehr-und Übungsbuch. Springer, New York
- Kuravi S, Trahan J, Goswami DY, Rahman MM, Stefanakos EK (2013) Thermal energy storage technologies and systems for concentrating solar power plants. *Prog Energy Combust Sci* 39(4):285–319
- Laing D, Steinmann WD, Tamme R, Richter C (2006) Solid media thermal storage for parabolic trough power plants. *Sol Energy* 80(10):1283–1289
- Laing D, Bahl C, Bauer T, Fiss M, Breidenbach N, Hempel M (2012) High-temperature solid-media thermal energy storage for solar thermal power plants. *Proc IEEE* 100(2):516–524
- Lane GA (1983) Solar heat storage: Latent heat materials, vol. i, background and scientific principles. CRC Press, Boca Raton
- Mettawee EBS, Assassa GM (2007) Thermal conductivity enhancement in a latent heat storage system. *Sol Energy* 81(7):839–845
- Michel B, Mazet N, Mauran S, Stitou D, Xu J (2012) Thermochemical process for seasonal storage of solar energy: characterization and modeling of a high density reactive bed. *Energy* 47(1):553–563
- Nagel T, Beckert S, Lehmann C, Gläser R, Kolditz O (2016) Multi-physical continuum models of thermochemical heat storage and transformation in porous media and powder beds—a review. *Appl Energy* 178:323–345
- Neeper D (2000) Thermal dynamics of wallboard with latent heat storage. *Sol Energy* 68(5):393–403
- Prasad L, Muthukumar P (2013) Design and optimization of lab-scale sensible heat storage prototype for solar thermal power plant application. *Sol Energy* 97:217–229
- Salomoni VA, Majorana CE, Giannuzzi GM, Miliozzi A, Di Maggio R, Girardi F, Mele D, Lucentini M (2014) Thermal storage of sensible heat using concrete modules in solar power plants. *Sol Energy* 103:303–315
- Sass I, Stegner J (2012) Coupled measurements of thermophysical and hydraulic properties of unsaturated and unconsolidated rocks. In: Proceedings, 37th Workshop on Geothermal Reservoir Engineering Stanford University, vol 30
- Sharma A, Tyagi V, Chen C, Buddhi D (2009) Review on thermal energy storage with phase change materials and applications. *Renew Sustain Energy Rev* 13(2):318–345
- Skinner JE, Strasser MN, Brown BM, Selvam RP (2014) Testing of high-performance concrete as a thermal energy storage medium at high temperatures. *J Sol Energy Eng* 136(2):021,004
- Solar Millennium A (2013) Die parabolrinnen-kraftwerke andasol 1 bis 3-die größten solarkraftwerke der welt. Solar Millennium AG, Erlangen
- Velraj R, Seeniraj R, Hafner B, Faber C, Schwarzer K (1999) Heat transfer enhancement in a latent heat storage system. *Sol Energy* 65(3):171–180
- Zalba B, Marín JM, Cabeza LF, Mehling H (2003) Review on thermal energy storage with phase change: materials, heat transfer analysis and applications. *Appl Therm Eng* 23(3):251–283

2.3 *Thermo-mechanical modelling of solid thermal energy storage with integrated heat exchangers*

X.-Y. Miao, T. Zheng, U.-J. Görke, O. Kolditz, T. Nagel, Thermo-mechanical analysis of heat exchanger design for thermal energy storage systems. *Applied Thermal Engineering*, Volume 114, March 2017, Pages 1082-1089.



Thermo-mechanical analysis of heat exchanger design for thermal energy storage systems



Xing-Yuan Miao ^{a,b}, Tianyuan Zheng ^{a,b}, Uwe-Jens Görke ^a, Olaf Kolditz ^{a,b}, Thomas Nagel ^{a,c,*}

^a Department of Environmental Informatics, Helmholtz Centre for Environmental Research – UFZ, Permoserstr. 15, 04318 Leipzig, Germany

^b Applied Environmental Systems Analysis, Technische Universität Dresden, Germany

^c Department of Mechanical and Manufacturing Engineering, School of Engineering, Trinity College Dublin, College Green, Dublin, Ireland

HIGHLIGHTS

- Analytical solution in the near field of the heat exchanger for extensive sensitivity analyses.
- Optimisation of thermal energy stores from a thermo-mechanical perspective.
- Case studies for typical heat exchanger materials and geometries.
- Analysis of water-saturated cement heat store.

ARTICLE INFO

Article history:

Received 23 September 2016

Revised 28 November 2016

Accepted 6 December 2016

Available online 19 December 2016

Keywords:

Sensible heat storage

Solid storage media

Thermo-mechanics

Heat exchanger design

Water-saturated cement

ABSTRACT

Significant tensile stresses inside solid thermal energy storage media are induced due to incompatible thermal expansion characteristics. These stresses can cause damage to the often brittle storage material which is associated with a performance loss of thermal properties or the partial loss of long-term mechanical stability. In the present paper, a previously introduced analytical approach is extended to estimate the effects of the dominant physical and geometrical quantities on critical tensile stresses around tubular heat exchangers. Results are presented in terms of three composite dimensionless parameters representing the geometrical and material parameters of the system. Analytical sensitivities furthermore provide a direct quantification of how these sensitivities depend on selected system parameters, thus giving clues regarding the most promising optimisation handles. A representative case study was performed and can serve as a guide-line for making design decisions from a mechanical perspective as a complement to the typically performed thermodynamic design.

© 2016 Elsevier Ltd. All rights reserved.

1. Introduction

Driven by the purpose of saving fossil resources and reducing air pollution, alternative technologies are being developed to capture and use renewable sources of energy, such as solar, wind and hydro power, or geothermal heat. In this context, thermal energy storage (TES) is a technology that is primarily used for alleviating the mismatch between energy demand and supply at varying temperature conditions [5] and allows a better management of the intermittent renewable energy; cf., for example, Braun et al. [4], Herrmann and Kearney [8], Hesaraki et al. [10].

Among the numerous technologies available, this article is concerned with sensible heat storage in solid media, which is extensively used in various heat storage applications [9,15,3,7,14,6,12]. This mature technology is cost-effective and can be qualified for most domestic and commercial applications while being environmentally benign.

The continuing development of TES systems is accompanied by specific requirements for heat exchangers. Not only does the heat exchanger need to be designed to achieve a high heat transfer efficiency [24], but also the thermo-mechanical and thermo-hydraulic performance of the heat exchanger and the surrounding storage media must be improved to maintain functional reliability during the operational life.

As there are numerous aspects implied in the multi-disciplinary design of a heat exchanger for solid sensible TES, presenting a comprehensive optimum may not be the most efficient and economical

* Corresponding author at: Department of Environmental Informatics, Helmholtz Centre for Environmental Research – UFZ, Permoserstr. 15, 04318 Leipzig, Germany.
E-mail address: thomas.nagel@ufz.de (T. Nagel).

Nomenclature

$\alpha_{1/2}$	linear thermal expansion coefficient of the heat exchanger/the storage material	ϑ	temperature difference with respect to T_0
\mathbf{C}	fourth-order stiffness tensor	A_i, C_i	integration constants
ϵ	small strain tensor	$E_{1/2}$	Young's modulus of the heat exchanger/the storage material
$\boldsymbol{\sigma}$	Cauchy stress tensor	$p_{0/2}$	pressure applied on the inner/outer boundary
$\nu_{1/2}$	Poisson's ratio of the heat exchanger/the storage material	$r_{0/1}$	inner/outer radius of the tube
$\sigma_{\phi\phi}^{1/2}$	circumferential stress in the heat exchanger/the storage material	S	tube pitch ($S = 2r_2$)
$\sigma_{rr}^{1/2}$	radial stress in the heat exchanger/the storage material	T_0	homogeneous reference temperature
φ	Airy stress function	T_u	ultimate storage temperature

procedure [2], and is not a uniquely posed problem. Accordingly, it is more reasonable to concentrate on those factors that have been identified as the most dominant in a given specific kind of TES system. Most existing studies focus on improving heat transfer performance along with overall cost reduction. Although, the analyses of mechanical fields for TES materials were presented in literature (cf., for example [20,23,22]), to the authors' knowledge, there are few studies taking into account thermo-mechanical effects in the solid TES with heat exchangers, such as critical stresses inside solid sensible TES during thermal cycling as well as quantifying the dependence of these stresses on key parameters of the heat exchanger and the storage material and using that information for design optimisation.

In this paper, we focus on estimating peak tensile stresses around tubular heat exchangers embedded in a solid heat storage medium as an indicator for the thermo-mechanical integrity of the heat store. The specific motivation for this problem comes from the observation of significant tensile stress within the storage material which is typically an affordable building material with a relatively low tensile strength [19,17]. Thus, such thermally induced stresses might quite possibly exceed the material's strength limits for an inappropriate combination of operating conditions, geometry and material. The purpose of the present study is twofold: (i) to investigate the effects of geometrical/physical parameters of the heat exchanger on the thermo-mechanical performance of the heat store unit in detail by using a previously developed analytical approach; (ii) to show how this analytical approach can be modified and used to select a heat exchanger which is optimal from a mechanical perspective and does not stand in contrast to thermodynamic requirements that are critical for the system's operation as a heat store.

Generally, a designated TES system is characterised by the geometric layout of its heat exchanger as well as the selected storage material which must satisfy the thermal performance requirements as well as provide long-term reliability. Mechanically, the incompatibility of the heat exchanger with the storage material in terms of material properties dominates the stresses induced by thermo-mechanical loads.

The heat exchanger layout investigated here is based on Laing et al. [16] and illustrated in Fig. 1a. According to the analytical solution presented in Miao et al. [17], three quantities were considered as the main geometric design parameters in the analysis: the outer and inner diameters of the heat exchanger, and the tube pitch which is defined as the centre-to-centre distance between two adjacent cylindrical heat exchangers, see Fig. 1b. The above configuration aside, our approach applies to other configurations composed of piping bundles embedded within a solid storage material as well (for example [1,18,21,11]).

This paper is organised as follows. In Section 2, the analytical solution used in the analysis is briefly reviewed. Dimensionless geometrical/physical quantities are derived to reduce the number of free parameters and to simplify the illustration of the analysis. In Section 3, result are presented for the optimal layout of a specific system based on the identification of dominant thermo-mechanical aspects in extensive sensitivity analyses Section B. The main conclusions of this paper are stated in Section 4.

2. Theoretical modelling

Heat transport models of the heat store were validated by distributed thermo-couple measurements [data not shown]. The stress fields within the cast cement block around the heat exchangers, however, cannot be readily measured and only indirect experimental evidence on their effects is available [19]. This motivated us to use theoretical modelling as the apparently most feasible way for their quantification. An extensively validated and simple linear thermo-elastic theory was employed and material parameters measured in the laboratory [17] were used.

To keep the approach simple and broadly applicable, it is based on a well-established engineering theory. The model describes a cylindrical region comprising the heat exchanger and the surrounding storage material and allows for an internal pressure as well as an external pressure acting on the cylinder walls.

The following assumptions were made to arrive at an analytical solution:

- (i) All materials are assumed to behave linearly elastic and to be isotropic.
- (ii) Body forces are not considered.
- (iii) Axisymmetry of geometry and loading is assumed.
- (iv) Radial displacement and radial stress are continuous at the interface.

Assumption (iv) carries the implicit assumption that $\alpha_1 \geq \alpha_2$, which is fulfilled in most practical cases.

The basic constitutive equation with respect to stresses, strains and temperature changes is written based on the thermo-elastic relation

$$\boldsymbol{\sigma} = \mathbf{C} : (\boldsymbol{\epsilon} - \alpha\vartheta\mathbf{I}) \quad (1)$$

Introducing a scalar valued stress function φ [13], the biharmonic equation

$$\Delta\Delta\varphi = 0 \quad (2)$$

can be shown to hold. Due to axisymmetry, Eq. (2) can be expressed as an ordinary differential equation

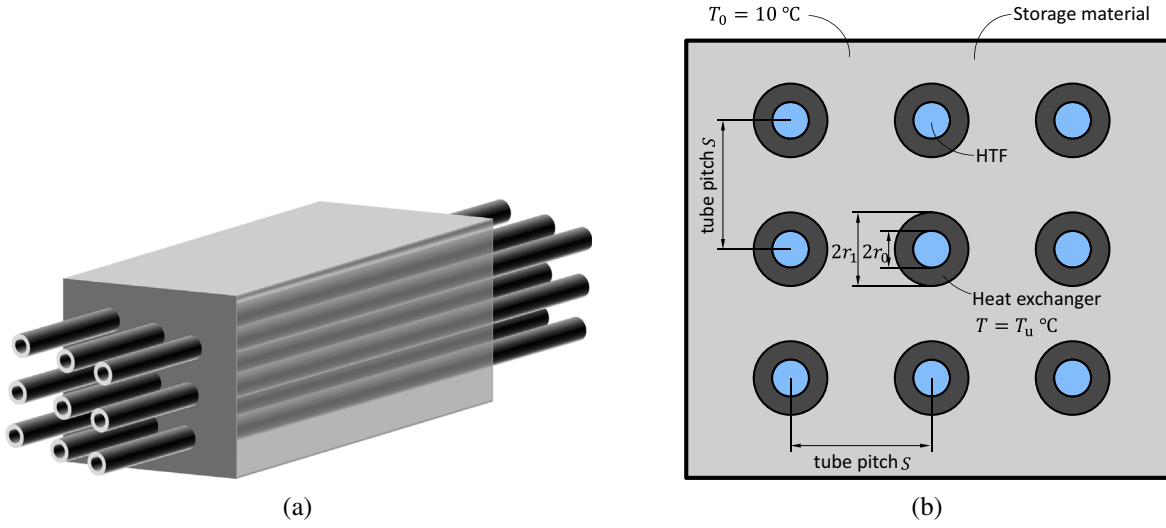


Fig. 1. Schematic and details of standard tubular heat exchanger's geometrical layout.

$$\frac{d}{dr} \left\{ r \frac{d}{dr} \left[\frac{1}{r} \frac{d}{dr} \left(r \frac{d\varphi}{dr} \right) \right] \right\} = 0 \quad (3)$$

As outlined in Miao et al. [17], a solution of Eq. (3) yields the following expressions for the stresses

$$\sigma_{rr}^i = \frac{A_i}{r^2} + 2C_i \quad (4)$$

$$\sigma_{\phi\phi}^i = -\frac{A_i}{r^2} + 2C_i \quad (5)$$

$$\sigma_{zz}^i = 4v_i C_i - E_i \alpha_i \vartheta_i \quad (6)$$

The integration constants A_i, C_i can be determined by the continuity and boundary conditions and are listed in Appendix A. For further details on the derivation as well as a comparison to numerical modelling results, see Miao et al. [17].

2.1. Dimensionless peak tensile stress

As outlined in Miao et al. [17], the peak tensile stress typically occurs within the storage material in the circumferential direction at the interface:

$$\sigma_{\phi\phi}^2 \Big|_{r_1} = -\frac{A_2}{r_1^2} + 2C_2 \quad (7)$$

As the peak tensile stress is the most critical stress for commonly used brittle storage media such as cementitious or ceramic materials, it will also be referred to as critical stress. For ease of notation, in the sequel we will simply write $\sigma_{\phi\phi}$ when referring to this quantity. To simplify the analysis, all variables influencing the critical tensile stress $\sigma_{\phi\phi}$ will be condensed into dimensionless quantities.

Suppose that negligible pressures are imposed on the boundaries, i.e., $p_0 = 0$ and $p_2 = 0$, and $T_u = \text{const.}$, i.e., the heat store is fully charged and at maximum homogeneous temperature which was confirmed to be the mechanically most critical practically occurring state by full transient heat transport simulations [17]. Then, A_2 can be rewritten as

$$A_2 = \frac{R_0 E_1 E_2 r_0^2 r_1^2 r_2^2 (\alpha_2 - \alpha_1) \vartheta}{E_1 r_0^2 R_0 [r_2^2 + r_1^2 + v_2 (r_2^2 - r_1^2)] - E_2 r_2^2 [r_0^2 + r_1^2 + v_1 (r_0^2 - r_1^2)]} \quad (8)$$

By introducing the dimensionless quantities

$$(r_0^*, r_1^*) = \frac{1}{r_2} (r_0, r_1), \quad R_0^* = \frac{1 - \frac{r_1^2}{r_0^2}}{r_1^{*2} - 1}, \quad (9)$$

$$E^* = \frac{E_1}{E_2}, \quad \vartheta^* = (\alpha_2 - \alpha_1) \vartheta \quad (10)$$

$$v_1^* = \frac{1 + v_1}{1 + v_2}, \quad v_2^* = \frac{1 - v_1}{1 - v_2}, \quad M^* = \frac{v_2^*}{E^*}, \quad (11)$$

the critical tensile stress normalised by the Young's modulus of the storage material can be written as:

$$\frac{\sigma_{\phi\phi}}{E_2} = -\frac{E^* \vartheta^* R_0^* (r_0^{*2} + r_1^{*2})}{r_0^{*2} (1 + v_2) (E^* R_0^* - v_1^*) + r_1^{*2} (1 - v_2) (E^* R_0^* r_0^{*2} - v_2^*)} \quad (12)$$

The dimensionless parameter R_0^* includes geometric sizes characteristic of the analytical solution, such as the inner and outer pipe radii as well as the tube pitch $S = 2r_2$. M^* indicates the stiffness of the storage material in comparison to that of the heat exchanger. The higher M^* is, the stiffer the storage material gets relatively. ϑ^* represents the difference in thermal strain between both materials at maximum ΔT .

The three quantities R_0^*, M^* and ϑ^* contain all ten parameters influencing the solution. In the following, the solution is used to obtain an optimum tube pitch, perform sensitivity analyses as well as a case study on how to select a suitable heat exchanger from a mechanical perspective.

3. Results

3.1. Sensitivity-based optimisation criterion

The dependence of the peak stress on multiple parameters provides flexibility regarding possible technical solutions satisfying specific design requirements of the heat store. Sensitivity analyses (see Appendix B) can serve as a guide-line for the design of the tube-type thermal storage in this respect.

As seen in Appendix B, increasing the tube pitch can lower the peak stress at the material interface up to a threshold value of S , beyond which a further increase of S has no effect (Fig. B.5c).

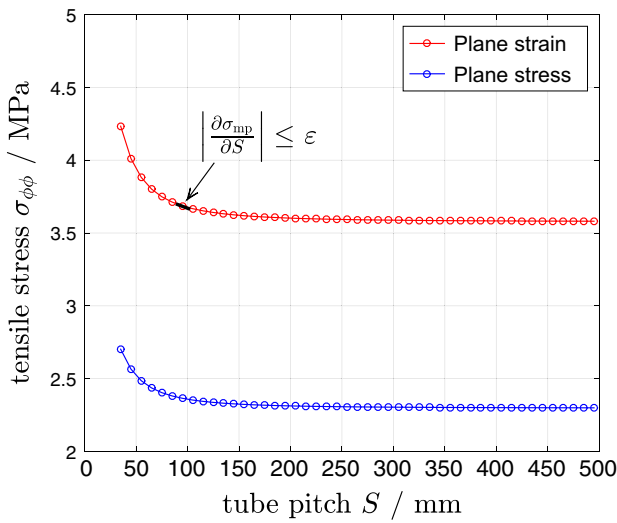


Fig. 2. Critical tensile stress $\sigma_{\phi\phi}$ varying with the tube pitch S .

Following that, Fig. 2 illustrates the peak tensile stress as it varies with the tube pitch.

After a sharp decline, the stress achieves asymptotically a constant value consistent with the observations in Appendix B. From an economic point of view, it is not necessary to extend the tube pitch any further as it does not lead to lower peak stresses. In combination with the observation that a fast heat input into the heat store and an equally fast heat extraction from it, i.e., a high thermal power, require a sufficiently tight packing of heat exchanger tubes or bundles, a certain optimum balance can be postulated: There is a maximum spacing allowed from a thermal perspective and a minimum spacing required from a mechanical perspective. Both measures can be combined into an objective function for a comprehensive optimisation. Here, the focus is exclusively on the mechanical contribution.

To define an optimal value, the lowest achievable peak stress σ_{mp} is here defined based on a threshold criterion as that stress where $|D_S| \leq \epsilon$ (see Fig. 2). Simultaneously, this defines the optimal tube pitch S_{mp} as that value of S that minimises the peak stress. S_{mp} is considered as a design parameter and an optimisation criterion. In this article, $\epsilon = 1\%$ has been used.

3.2. Optimal tube-pitch in a novel heat store

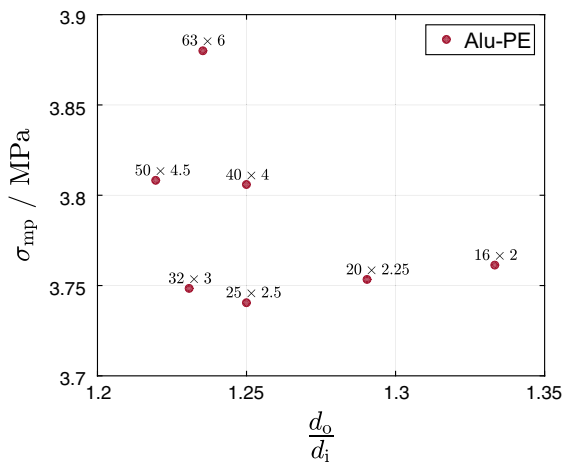
All sensitivities investigated above change monotonically, except for those with respect to the inner and outer radii of the heat exchanger, which show a more complex variation, see Fig. B.5a and b. To further study the effects of the radii on the peak stress and the tube pitch, a case study with prescribed geometrical sizes of the heat exchanger used in the present project [17] is conducted. Since the heat exchanger material has been selected to be an aluminium-polyethylene composite, M^* can be considered fixed and so can θ^* for a given maximum storage temperature of 90 °C.

Fig. 3a illustrates the minimum peak tensile stress values achievable (σ_{mp}) with the given heat exchanger for the available pipe geometries according to the $|D_S| \leq 1\%$ criterion. Corresponding to these stress values, Fig. 3b plots the optimised tube pitch values at which the lowest critical stress values are achieved. A comparison of both figures indicates the complex interactions between the peak stress, the tube pitch and the dimensions of the heat exchanger. The appropriate dimension which leads to the minimal peak stress does not coincide with the minimal tube pitch, see Fig. 3a and b.

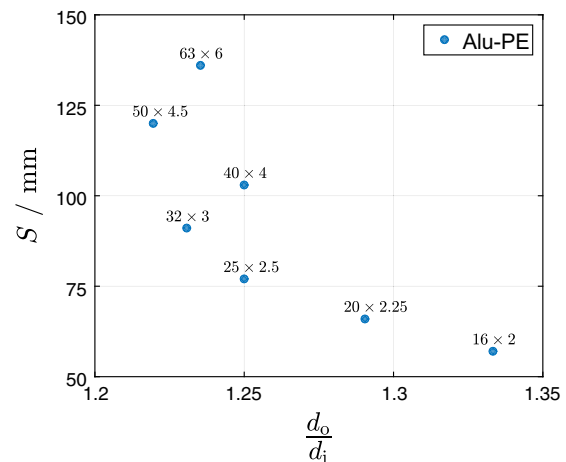
Considering the results, a good compromise may be to choose the 25 × 2.5 pipe, as it yields the lowest stress value of all pipes at a tube spacing of 75 mm, which—as confirmed by numerical studies not shown here—also provides the required thermal performance characteristics.

4. Conclusions

In this paper, a new analytical approach for aiding design choices in solid thermal energy storage with tubular heat exchangers was proposed based on thermo-mechanical arguments. It captured the dominant factors that affect the mechanical integrity of the heat store, and allowed the identification of optimal properties in the sense of minimal induced stresses while maintaining thermal performance requirements. Sensitivity analyses indicated the flexibility of selecting the appropriate heat exchanger for satisfying the design requirements mechanically or thermally. Additionally, analytical sensitivities directly yield their dependence on all relevant parameters, which is a significant benefit of the analytical over a numerical approach. By studying a currently developed system it was shown how a specific design choice regarding the optimal tube pitch can be made.



(a) Minimal peak stress.



(b) Optimal tube pitch.

Fig. 3. The peak stress and the tube pitch based on different dimensions of the heat exchanger made from an aluminium-polyethylene composite.

Acknowledgements

Funding was provided by the Federal Ministry of Economic Affairs and Energy under Grant No. 0325547C (“Analysis, modelling and assessment of an intelligent and environmentally neutral geothermal long-term heat storage system”, project acronym IGLU) and is gratefully acknowledged.

Appendix A. Integration constants

The integration constants required for Eqs. (4)–(6) are given by

$$A_1 = \frac{E_2(1 - \nu_1)r_0^2r_1^2r_2^2p_0 + E_1r_0^2[-r_1^2r_2^2p_2 - R_1(r_1^2 + r_2^2)] + E_1\nu_2r_0^2[r_1^2r_2^2p_2 + R_1(r_1^2 - r_2^2)]}{E_1r_0^2R_0[r_2^2 + r_1^2 + \nu_2(r_2^2 - r_1^2)] - E_2r_2^2[r_0^2 + r_1^2 + \nu_1(r_0^2 - r_1^2)]} + \frac{E_1E_2r_0^2r_1r_2^2[\alpha_2(\psi_2(r)|_{r_1} - r_1T_0) - \alpha_1(\psi_1(r)|_{r_1} - r_1T_0)]}{E_1r_0^2R_0[r_2^2 + r_1^2 + \nu_2(r_2^2 - r_1^2)] - E_2r_2^2[r_0^2 + r_1^2 + \nu_1(r_0^2 - r_1^2)]} \quad (A.1)$$

$$A_2 = R_0A_1 + R_1 \quad (A.2)$$

$$C_1 = -\frac{1}{2}\left(p_0 + \frac{A_1}{r_0^2}\right) \quad (A.3)$$

$$C_2 = -\frac{1}{2}\left(p_2 + \frac{A_2}{r_2^2}\right) \quad (A.4)$$

where $R_0 = \frac{r_2^2(r_0^2 - r_1^2)}{r_0^2(r_1^2 - r_2^2)}$ and $R_1 = -\frac{r_1^2r_2^2(p_0 + p_2)}{r_1^2 - r_2^2}$.

Appendix B. Sensitivity analyses

To determine the dominant physical parameters affecting the peak stress, sensitivity analyses were performed. To maintain physical intuition and facilitate interpretation, the dimensions of the problem are maintained. The values and trends of the sensitivities will strongly depend on the reference state, i.e., the point in the parameter space at which the derivatives will be taken. In order to maintain a specific link to an ongoing project and to practically relevant parameter values, the baseline system parameters were set to values employed in the IGLU project, compare Table B.1 and Fig. 3, and the maximum storage temperature of 90 °C was used aligned with domestic requirements. For a more detailed description of the prototype, the interested reader is referred to Miao et al. [17].

To simplify the following expressions, we define

$$G(E_1, E_2, \alpha_1, \alpha_2, r_0, r_1, r_2) = E_1E_2R_0r_0^2(r_1^2 + r_2^2)(\alpha_2 - \alpha_1)\vartheta \quad (B.1)$$

$$F(E_1, E_2, \nu_1, \nu_2, r_0, r_1, r_2) = E_1R_0r_0^2[r_2^2 + r_1^2 + \nu_2(r_2^2 - r_1^2)] - E_2r_2^2[r_0^2 + r_1^2 + \nu_1(r_0^2 - r_1^2)] \quad (B.2)$$

The first-order partial derivatives of the circumferential tensile stress in the storage material at the interface $\sigma_{\phi\phi}$ with respect to the independent material parameters ($E_1, E_2, \nu_1, \nu_2, \alpha_1, \alpha_2$) and the tube pitch ($S = 2r_2$) as well as the tube dimensions (r_0, r_1) can be found as

$$\mathcal{D}_{E_1} = \frac{\partial \sigma_{\phi\phi}}{\partial E_1} \Big|_{r_1} = -\frac{E_2R_0r_0^2(r_1^2 + r_2^2)(\alpha_2 - \alpha_1)\vartheta F - GR_0r_0^2[r_2^2 + r_1^2 + \nu_2(r_2^2 - r_1^2)]}{F^2} \quad (B.3)$$

$$\mathcal{D}_{E_2} = \frac{\partial \sigma_{\phi\phi}}{\partial E_2} \Big|_{r_1} = -\frac{E_1R_0r_0^2(r_1^2 + r_2^2)(\alpha_2 - \alpha_1)\vartheta F + Gr_2^2[r_0^2 + r_1^2 + \nu_1(r_0^2 - r_1^2)]}{F^2} \quad (B.4)$$

$$\mathcal{D}_{\nu_1} = \frac{\partial \sigma_{\phi\phi}}{\partial \nu_1} \Big|_{r_1} = \frac{GE_2r_2^2(r_1^2 - r_0^2)}{F^2} \quad (B.5)$$

$$\mathcal{D}_{\nu_2} = \frac{\partial \sigma_{\phi\phi}}{\partial \nu_2} \Big|_{r_1} = \frac{GE_1R_0r_0^2(r_2^2 - r_1^2)}{F^2} \quad (B.6)$$

$$\mathcal{D}_{\alpha_1} = \frac{\partial \sigma_{\phi\phi}}{\partial \alpha_1} \Big|_{r_1} = \frac{E_1E_2R_0r_0^2(r_1^2 + r_2^2)\vartheta}{F} \quad (B.7)$$

$$\mathcal{D}_{\alpha_2} = \frac{\partial \sigma_{\phi\phi}}{\partial \alpha_2} \Big|_{r_1} = -\frac{E_1E_2R_0r_0^2(r_1^2 + r_2^2)\vartheta}{F} \quad (B.8)$$

$$\mathcal{D}_{r_0} = \frac{\partial \sigma_{\phi\phi}}{\partial r_0} \Big|_{r_1} = -\frac{2GF - G\{E_1R_02r_0^2[r_2^2 + r_1^2 + \nu_2(r_2^2 - r_1^2)] - E_2r_2^22r_0^2(1 + \nu_1)\}}{r_0F^2} \quad (B.9)$$

$$\mathcal{D}_{r_1} = \frac{\partial \sigma_{\phi\phi}}{\partial r_1} \Big|_{r_1} = -\frac{E_1E_2R_0r_0^22r_1(\alpha_2 - \alpha_1)\vartheta F - G\{E_1R_0r_0^22r_1(1 - \nu_2) - E_2r_2^22r_1(1 - \nu_1)\}}{F^2} \quad (B.10)$$

$$\mathcal{D}_S = \frac{\partial \sigma_{\phi\phi}}{\partial S} \Big|_{r_1} = -\frac{E_1E_2R_0r_0^2S(\alpha_2 - \alpha_1)\vartheta F - G\{E_1R_0r_0^2S(1 + \nu_2) - E_2S[r_0^2 + r_1^2 + \nu_1(r_0^2 - r_1^2)]\}}{F^2} \quad (B.11)$$

These sensitivities represent the gradient of $\sigma_{\phi\phi}$ in the cement at the interface with respect to the specified parameters. Note, that only one parameter is changed at a time, all other parameters remaining fixed.

Eqs. (B.7) and (B.8) imply that the relation between the peak stress and the thermal expansion coefficient is linear, i.e. the sensitivity \mathcal{D} is independent of the parameter itself. \mathcal{D}_{α_1} is positive while \mathcal{D}_{α_2} is negative. In the reference state, $\mathcal{D}_{\alpha_1} = 125$ GPa K and

Table B.1

Material properties of the specific heat exchangers and the storage material used in IGLU project.

Materials	Density ρ_{SR} (kg m ⁻³)	Thermal conductivity λ_{TS} (W m ⁻¹ K ⁻¹)	Thermal expansion α_{TS} (K ⁻¹ ·10 ⁻⁶)	Heat capacity c_{TS} (J kg ⁻¹ K ⁻¹)	Elastic modulus E (GPa)
<i>Heat exchanger</i>					
Alu-PE composite	1825	0.4	30	2200	68.9
<i>Storage material</i>					
Füllbinder L	1583	0.96	10.7	2083	1.9

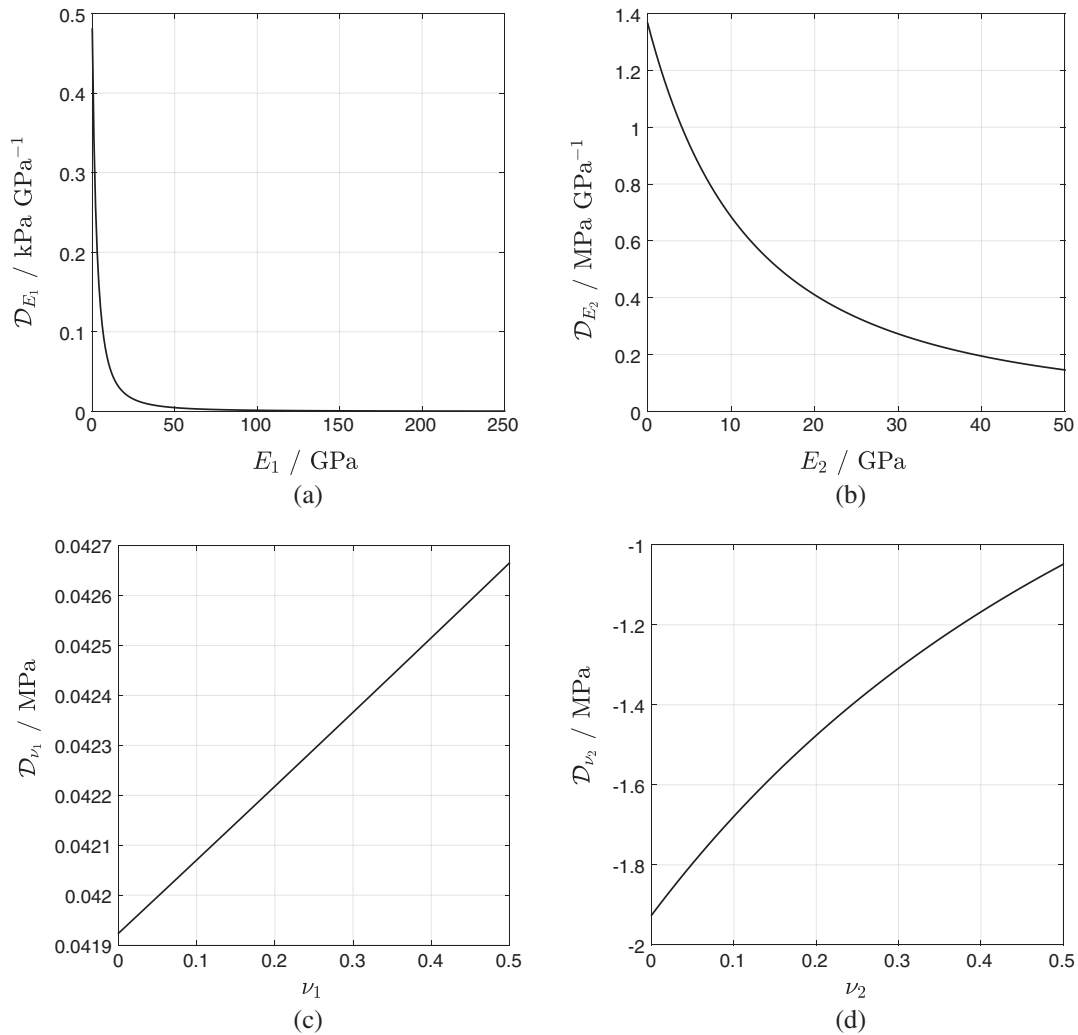


Fig. B.4. Sensitivity of the objective tensile stress with respect to the material parameters. (a)/(b): Young's modulus of the heat exchanger/the storage material; (c)/(d): Poisson's ratio of the heat exchanger/the storage material.

$\mathcal{D}_{\alpha_2} = -125 \text{ GPa K}$. This is reminiscent of the fact that due to the inherent assumption of $\alpha_1 \geq \alpha_2$ a decrease in stress can be brought about by a decrease of $\alpha_1 - \alpha_2$, which can be achieved either by increasing α_2 or by decreasing α_1 .

As shown in Fig. B.4a and b, the sensitivity to changes in the Young's modulus of the storage material is about three orders of magnitude higher than that of the heat exchanger. Generally, the sensitivities decrease with an increase in the Young's moduli. This trend levels off for higher Young's moduli. As the stiffness of the pipe increases to very high values in comparison to the filler it completely dominates the deformation in the cement to the point where small changes in E_1 have little effect. At the reference state, the sensitivities are approximately $2.56 \text{ kPa GPa}^{-1}$ (E_1) and 1.2 MPa GPa^{-1} (E_2). Both sensitivities are positive, i.e. an increase in any Young's modulus causes an increase in stresses.

The effect of the Poisson's ratio on the peak stress is sublinearly increasing, and the one of the storage material again has a stronger influence than that of the heat exchanger, see Fig. B.4c and d. The sensitivity with respect to the Poisson's ratio is higher than the one with respect to changes in the Young's moduli. At the reference state, the sensitivities are approximately 0.04 MPa (ν_1) and -1.53 MPa (ν_2). In particular $\mathcal{D}_{\nu_1} > 0$ and $\mathcal{D}_{\nu_2} < 0$ highlight the

qualitatively opposite impact of both parameters. Increasing the Poisson's ratio of the storage material can have a significant reducing effect on the peak stress.

The influence of the geometrical configuration of the heat exchanger is more polymorph. The sensitivity of the inner diameter is positive and exhibits a comparatively dominant influence in the region where the thickness of the heat exchanger is high, while the outer diameter has negative sensitivity when the thickness is extremely low. As the thickness increases, the sensitivity is positive and exhibits a peak value. In the reference state, the sensitivities are approximately $0.014 \text{ MPa mm}^{-1}$ (r_0) and $0.003 \text{ MPa mm}^{-1}$ (r_1). Under standard conditions, the sensitivities of r_0 and r_1 have approximately the same order of magnitude as one of S with respect to the peak stress.

The first-order partial derivative of the peak stress with respect to the tube pitch in Fig. B.5c shows the existence of a threshold value above which the sensitivity is practically zero, i.e., a further increase in tube pitch has no impact. At the reference state, the sensitivity is $-0.005 \text{ MPa mm}^{-1}$, i.e. increasing the tube pitch will lower the peak tensile stress.

So far, the effect of each parameter was studied in isolation. In practical applications, an independent choice may not always be possible.

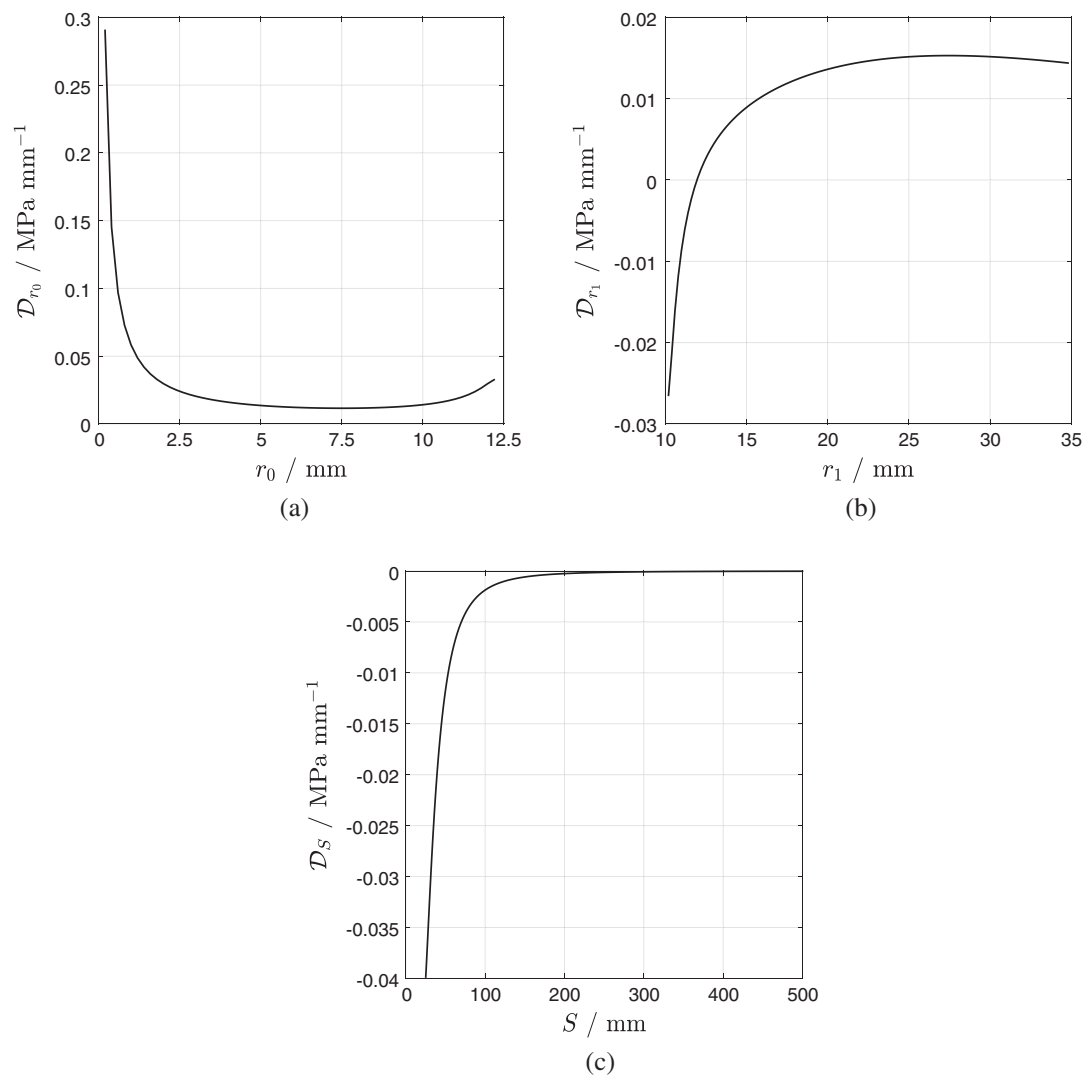


Fig. B.5. Sensitivity of the objective tensile stress with respect to the geometrical parameters, (a)/(b) the inner/outer radius of the heat exchanger, (c) the tube pitch.

References

- [1] F. Agyenim, P. Eames, M. Smyth, Heat transfer enhancement in medium temperature thermal energy storage system using a multitube heat transfer array, *Renew. Energy* 35 (1) (2010) 198–207.
- [2] Z. Bao, F. Yang, Z. Wu, S.N. Nyamsi, Z. Zhang, Optimal design of metal hydride reactors based on cfd–taguchi combined method, *Energy Convers. Manage.* 65 (2013) 322–330.
- [3] D. Bauer, R. Marx, J. Nußbicker-Lux, F. Ochs, W. Heidemann, H. Müller-Steinhagen, German central solar heating plants with seasonal heat storage, *Solar Energy* 84 (4) (2010) 612–623.
- [4] J.E. Braun, S. Klein, J. Mitchell, Seasonal storage of energy in solar heating, *Solar Energy* 26 (5) (1981) 403–411.
- [5] L.F. Cabeza, *Advances in Thermal Energy Storage Systems: Methods and Applications*, Elsevier, 2014.
- [6] A. Duffy, M. Rogers, L. Ayompe, *Renewable Energy and Energy Efficiency: Assessment of Projects and Policies*, John Wiley & Sons, 2015.
- [7] A. Gil, M. Medrano, I. Martorell, A. Lázaro, P. Dolado, B. Zalba, L.F. Cabeza, State of the art on high temperature thermal energy storage for power generation. Part 1–Concepts, materials and modellization, *Renew. Sustain. Energy Rev.* 14 (1) (2010) 31–55.
- [8] U. Herrmann, D.W. Kearney, Survey of thermal energy storage for parabolic trough power plants, *J. Solar Energy Eng.* 124 (2) (2002) 145–152.
- [9] U. Herrmann, B. Kelly, H. Price, Two-tank molten salt storage for parabolic trough solar power plants, *Energy* 29 (5) (2004) 883–893.
- [10] A. Hesaraki, S. Holmberg, F. Haghighat, Seasonal thermal energy storage with heat pumps and low temperatures in building projects—a comparative review, *Renew. Sustain. Energy Rev.* 43 (2015) 1199–1213.
- [11] Y. Jian, F. Bai, Q. Falcoz, C. Xu, Y. Wang, Z. Wang, Thermal analysis and design of solid energy storage systems using a modified lumped capacitance method, *Appl. Therm. Eng.* 75 (2015) 213–223.
- [12] Y. Jian, Q. Falcoz, P. Neveu, F. Bai, Y. Wang, Z. Wang, Design and optimization of solid thermal energy storage modules for solar thermal power plant applications, *Appl. Energy* 139 (2015) 30–42.
- [13] R. Kreißig, U. Benedix, *Höhere technische Mechanik: Lehr- und Übungsbuch*, Springer-Verlag, 2013.
- [14] D. Laing, C. Bahl, T. Bauer, M. Fiss, N. Breidenbach, M. Hempel, High-temperature solid-media thermal energy storage for solar thermal power plants, *Proc. IEEE* 100 (2) (2012) 516–524.
- [15] D. Laing, W.-D. Steinmann, M. Fiß, R. Tamme, T. Brand, C. Bahl, Solid media thermal storage development and analysis of modular storage operation concepts for parabolic trough power plants, *J. Solar Energy Eng.* 130 (1) (2008) 011006.
- [16] D. Laing, W.-D. Steinmann, R. Tamme, C. Richter, Solid media thermal storage for parabolic trough power plants, *Solar Energy* 80 (10) (2006) 1283–1289.
- [17] X.-Y. Miao, C. Beyer, U.-J. Görke, O. Kolditz, H. Hailemariam, T. Nagel, Thermo-hydro-mechanical analysis of cement-based sensible heat stores for domestic applications, *Environ. Earth Sci.* 75 (18) (2016) 1293.
- [18] M. Raju, S. Kumar, Optimization of heat exchanger designs in metal hydride based hydrogen storage systems, *Int. J. Hydrogen Energy* 37 (3) (2012) 2767–2778.
- [19] J.E. Skinner, M.N. Strasser, B.M. Brown, R.P. Selvam, Testing of high-performance concrete as a thermal energy storage medium at high temperatures, *J. Solar Energy Eng.* 136 (2) (2014) 021004.
- [20] J. Su, L. Ren, L. Wang, Preparation and mechanical properties of thermal energy storage microcapsules, *Colloid Polym. Sci.* 284 (2) (2005) 224–228.

- [21] M. Wu, M. Li, C. Xu, Y. He, W. Tao, The impact of concrete structure on the thermal performance of the dual-media thermozone thermal storage tank using concrete as the solid medium, *Appl. Energy* 113 (2014) 1363–1371.
- [22] H.-W. Yuan, C.-H. Lu, Z.-Z. Xu, Y.-R. Ni, X.-H. Lan, Mechanical and thermal properties of cement composite graphite for solar thermal storage materials, *Solar Energy* 86 (11) (2012) 3227–3233.
- [23] G.H. Zhang, C.-Y. Zhao, Thermal and rheological properties of microencapsulated phase change materials, *Renew. Energy* 36 (11) (2011) 2959–2966.
- [24] N. Zheng, W. Liu, Z. Liu, P. Liu, F. Shan, A numerical study on heat transfer enhancement and the flow structure in a heat exchanger tube with discrete double inclined ribs, *Appl. Therm. Eng.* 90 (2015) 232–241.

2.4 *Phase-field modelling of fracture in poroelastic solids*

X.-Y. Miao, O. Kolditz, T. Nagel, Phase-field modeling of fracture in poroelastic solids for thermal energy storage. *Poromechanics VI: Proceedings of the Sixth Biot Conference on Poromechanics*, Paris, France, July 9-13, 2017, Pages 1976-1983.

Phase-field modeling of fracture in poroelastic solids for thermal energy storage

Xing-Yuan Miao^{1,2}, Olaf Kolditz^{1,2}, Thomas Nagel^{1,3}

¹Department of Environmental Informatics, Helmholtz Centre for Environmental Research – UFZ, Permoserstr. 15, 04318 Leipzig, Germany; PH (341) 235-1882; email: xing-yuan.miao@ufz.de

²Applied Environmental Systems Analysis, Technische Universität Dresden, Germany

³Department of Mechanical and Manufacturing Engineering, School of Engineering, Trinity College Dublin, College Green, Dublin, Ireland

ABSTRACT

The development of a continuum phase-field model of brittle fracture for poroelastic solids is presented. Three treatments for deriving the evolution equation of the phase-field are compared. The phase-field approach transforms the discontinuous crack interface into a continuous diffusive setting. The diffuseness is controlled by a length scale parameter which is also associated with the stress state in the process zone. A one-dimensional beam model with an analytical solution is provided for the verification of the current numerical implementation.

INTRODUCTION

The phase-field approach is a promising numerical treatment for addressing crack evolution. The principal highlight of this approach is to tackle the crack interface from a continuous configurational perspective. The fracture surfaces are no longer tracked and instead are represented by smooth phase transition boundaries that are interposed between the fully damaged and undamaged zones. The diffusive crack topology is characterised by a length scale parameter which also affects the stress state in the process zone. In the context of Γ -convergence, such a continuous diffusive crack converges to a discontinuous sharp crack with a Griffith-type surface energy.

The phase-field characterisation is proposed to patch the insufficient descriptions for the crack evolution in the framework of classical theory of brittle fracture. In this contribution, the specific motivation of exploring crack initiation and propagation in porous media comes from the observation of critical tensile stresses within a water-saturated material which is used in a novel thermal energy store, cf., Miao (2016), Miao (2017). Measurements on the material samples indicate that the material has a relatively low tensile strength and fails in a brittle manner.

Not only for this specific material, but also for other brittle storage materials, as well as geotechnical and geological materials, these critical stresses can cause damage and subsequently fracture which is associated with the partial loss of long-term mechanical stability of the structures they compose. Furthermore, the induced cracks can

increase the permeability of the storage material and alter its water-retention properties. Driven by the purpose of providing a numerical implementation based on a general theoretical concept for various research projects, however, the main objective is to summarise a recent implementation into the open-source finite element platform Open-GeoSys, as well as different theoretical access routes to the topic.

NUMERICAL TREATMENT

Basic equations

In the framework of isotropic linear elasticity, the undamaged elastic energy density is

$$\psi_e(\epsilon_{el}) = \frac{1}{2} \lambda \text{tr}(\epsilon_{el})^2 + \mu \epsilon_{el} : \epsilon_{el} \tag{1}$$

where λ and μ are the Lamé constants.

The approximation of the Helmholtz free energy functional of a fractured body could have the formulation of

$$E(\mathbf{u}, \text{grad } \mathbf{u}, d) = \int_{\Omega} [(d^2 + k) \psi_e^+(\epsilon_{el}) + \psi_e^-(\epsilon_{el})] dV + g_c \int_{\Omega} \left[\frac{1}{4\varepsilon} (1 - d)^2 + \varepsilon \text{grad } d \cdot \text{grad } d \right] dV + \frac{1}{2\tau} \int_{CR_{l-1}} d^2 dV \tag{2}$$

where d represents the crack field, see, Fig. 1b; k represents a residual stiffness. A penalized functional is introduced as one of several options to prevent usually unphysical healing of the crack field with τ the penalty constant.

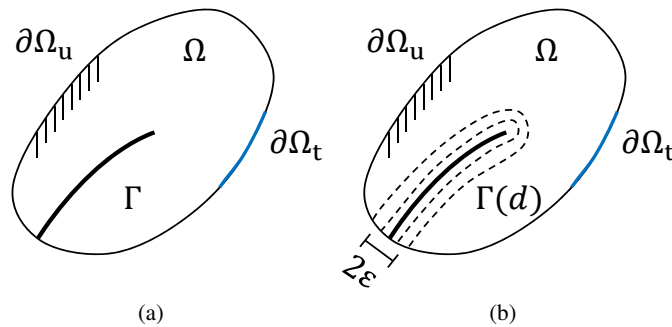


Figure 1: Elastic body with: (a) sharp crack; (b) diffusive crack characterised by a length scale parameter 2ε .

The external mechanical work functional is defined as

$$W_{\text{ext}}(\mathbf{u}) = \int_{\partial\Omega_t} \bar{\mathbf{t}} \cdot \mathbf{u} dA + \int_{\Omega} \rho \mathbf{b} \cdot \mathbf{u} dV \tag{3}$$

where $\bar{\mathbf{t}}$ is the surface traction on $\partial\Omega_t$, \mathbf{b} the specific body force.

Thus, the global system assembles in the case of elastic deformation and brittle fracture

$$\Pi = E(\mathbf{u}, \text{grad } \mathbf{u}, d) - W_{\text{ext}}(\mathbf{u}), \tag{4}$$

with equilibrium for a quasi-static process demanding

$$\delta\Pi = \frac{\partial\Pi}{\partial\mathbf{u}} \cdot \delta\mathbf{u} + \frac{\partial\Pi}{\partial d} \delta d = 0 \tag{5}$$

Applying the Gauss theorem with respect to each term of the right-hand side of Eq. (5) yields

$$\begin{aligned} \frac{\partial\Pi}{\partial\mathbf{u}} \delta\mathbf{u} = & - \int_{\Omega} \text{div} [(d^2 + k) \boldsymbol{\sigma}_0^+ + \boldsymbol{\sigma}_0^-] \delta\mathbf{u} dV + \int_{\partial\Omega_t} [(d^2 + k) \boldsymbol{\sigma}_0^+ + \boldsymbol{\sigma}_0^-] \mathbf{n} \cdot \delta\mathbf{u} dA \\ & - \int_{\partial\Omega_t} \bar{\mathbf{t}} \cdot \delta\mathbf{u} dA - \int_{\Omega} \varrho \mathbf{b} \cdot \delta\mathbf{u} dV \end{aligned} \tag{6}$$

$$\begin{aligned} \frac{\partial\Pi}{\partial d} \delta d = & \int_{\Omega} 2d\psi_e^+(\boldsymbol{\epsilon}_{\text{el}}) \delta d dV - \int_{\Omega} \frac{1-d}{2\varepsilon} g_c \delta d dV + \int_{\partial\Omega} 2\varepsilon g_c \text{grad } d \cdot \mathbf{n} \delta d dA \\ & - \int_{\Omega} 2\varepsilon g_c \text{div}(\text{grad } d) \delta d dV + \frac{1}{\tau} \int_{\text{CR}_{l-1}} d \delta d dV \end{aligned} \tag{7}$$

thus leading to the following set of PDEs along with the respective Neumann-type boundary conditions

$$\text{div} [(d^2 + k) \boldsymbol{\sigma}_0^+ + \boldsymbol{\sigma}_0^-] + \varrho \mathbf{b} = \mathbf{0} \tag{8}$$

$$2d\psi_e^+(\boldsymbol{\epsilon}_{\text{el}}) - \frac{1-d}{2\varepsilon} g_c - 2\varepsilon g_c \text{div}(\text{grad } d) + \frac{d}{\tau} H(\epsilon_{\text{tol}} - d) = 0 \tag{9}$$

$$[(d^2 + k) \boldsymbol{\sigma}_0^+ + \boldsymbol{\sigma}_0^-] \cdot \mathbf{n} - \bar{\mathbf{t}} = \mathbf{0} \quad \text{on } \partial\Omega_t \tag{10}$$

$$\text{grad } d \cdot \mathbf{n} = 0 \quad \text{on } \partial\Omega \tag{11}$$

THREE APPROACHES OF DERIVING THE PHASE-FIELD EQUATION FOR NON-EQUILIBRIUM EVOLUTION

Thermodynamic formulation

Based on the first and second law of thermodynamics, in the framework of linear elasticity for small deformations, the Clausius-Planck inequality for an isothermal process in a purely mechanical setting with $\bar{\psi}(\boldsymbol{\epsilon}, d, \text{grad } d)$ is formulated as (cf., Ehlers (2017))

$$\left(\boldsymbol{\sigma} - \varrho \frac{\partial\bar{\psi}}{\partial\boldsymbol{\epsilon}} \right) : \dot{\boldsymbol{\epsilon}} - \varrho \left[\frac{\partial\bar{\psi}}{\partial d} - \text{div} \left(\frac{\partial\bar{\psi}}{\partial \text{grad } d} \right) \right] \dot{d} - \varrho \text{div} \left(\frac{\partial\bar{\psi}}{\partial \text{grad } d} \dot{d} \right) \geq 0 \tag{12}$$

with a specific Helmholtz free energy $\bar{\psi}$. To fulfill the inequality, the constitutive equation for stresses is found as

$$\boldsymbol{\sigma} = \varrho \frac{\partial\bar{\psi}}{\partial\boldsymbol{\epsilon}} \tag{13}$$

and the boundary condition

$$\frac{\partial \bar{\psi}}{\partial \text{grad } d} \cdot \mathbf{n} = 0 \quad \text{on } \partial \Omega \tag{14}$$

The evolution equation can be found with $M > 0$ as

$$\dot{d} = -\rho \left[\frac{\partial \bar{\psi}}{\partial d} - \text{div} \left(\frac{\partial \bar{\psi}}{\partial \text{grad } d} \right) \right] M \tag{15}$$

We here use a well-qualified approximating function proposed by Ambrosio (1990) to define the Helmholtz free energy functional as

$$\rho \bar{\psi} = (d^2 + k) \psi_e^+(\boldsymbol{\epsilon}) + g_c \left[\frac{1}{4\varepsilon} (1 - d)^2 + \varepsilon \text{grad } d \cdot \text{grad } d \right] + \psi_e^-(\boldsymbol{\epsilon}) \tag{16}$$

Substituting Eq. (16) into Eq. (15) obtains a specific formulation of the evolution equation

$$\frac{\dot{d}}{M} = -2d\psi_e^+(\boldsymbol{\epsilon}) + g_c \left[\frac{1}{2\varepsilon} (1 - d) + 2\varepsilon \text{div}(\text{grad } d) \right] \tag{17}$$

Geometrical treatment

A one-dimensional phase-field-type diffusive crack can be approached by an intuitive geometrical treatment, cf., Miehe (2010), see Fig. 1. The sharp crack (Fig. 1a) can be approximated by an exponential function

$$d(x) = 1 - e^{-\frac{|x|}{2\varepsilon}} \tag{18}$$

with the Dirichlet-type boundary conditions

$$d(0) = 0 \quad \text{and} \quad d(\pm\infty) = 1 \tag{19}$$

Eq. (18) defines a diffusive crack topology (Fig. 1b). $\varepsilon \rightarrow 0$ implies that the diffusive crack converges to a discontinuous sharp crack. In a mathematical sense, it can be found that Eq. (18) is the solution of a second-order partial differential equation

$$4\varepsilon^2 d''(x) - d(x) + 1 = 0 \quad \text{in } \Omega \tag{20}$$

Eq. (20) is the Euler equation of an integral with the solution

$$d = \underset{d \in \Lambda}{\text{Arg min}} [I(d)] \tag{21}$$

with

$$I(d) = \Gamma_\varepsilon(d) = \int_\Omega \gamma dV = \int_\Omega \left[\frac{1}{4\varepsilon} (1 - d)^2 + \varepsilon \text{grad } d \cdot \text{grad } d \right] dV \tag{22}$$

where $\Lambda = \{d | d(0) = 0, d(\pm\infty) = 1\}$. The evolution of crack process is characterised by the extend of the regularised crack surface

$$\dot{\Gamma}_\varepsilon(d) = \int_\Omega \frac{\delta \gamma}{\delta d} \dot{d} dV = \int_\Omega -\frac{1}{2\varepsilon} [(1 - d) + 2\varepsilon \text{div}(\text{grad } d)] \dot{d} dV \geq 0 \tag{23}$$

Configurational forces

In the framework of isothermal phase transitions, the crack field d is treated as an order parameter characterising the phases of the body. The evolution of the crack field, i.e., the order parameter can be derived from the notion of configurational (material) forces. Gurtin (2008) introduced an additional configurational balance equation for the micro force system:

$$\text{div}\boldsymbol{\xi} + \pi + \omega = 0 \tag{24}$$

Note that, in this context, $\boldsymbol{\xi}$ represents a micro stress vector, π and ω are scalar internal and external micro forces, respectively. Postulating $\tilde{\psi} = \tilde{\psi}(\boldsymbol{\epsilon}, d, \text{grad } d, \dot{d})$ the Clausius-Planck inequality extended for micro-system contributions reads

$$\left(\boldsymbol{\sigma} - \frac{\partial \tilde{\psi}}{\partial \boldsymbol{\epsilon}}\right) : \dot{\boldsymbol{\epsilon}} + \left(\boldsymbol{\xi} - \frac{\partial \tilde{\psi}}{\partial \text{grad } d}\right) \cdot \text{grad } \dot{d} - \left(\pi + \frac{\partial \tilde{\psi}}{\partial d}\right) \dot{d} - \frac{\partial \tilde{\psi}}{\partial \dot{d}} \ddot{d} \geq 0 \tag{25}$$

In which, due to equipresence, $\pi = \pi(\boldsymbol{\epsilon}, d, \text{grad } d, \dot{d})$. Then, the dissipation reads

$$\pi = -\frac{\dot{d}}{M} - \frac{\partial \tilde{\psi}}{\partial d} \tag{26}$$

Substituting Eq. (26) into Eq. (24) with $\omega := 0$ yields

$$\text{div} \frac{\partial \tilde{\psi}}{\partial \text{grad } d} - \frac{\partial \tilde{\psi}}{\partial d} = \frac{\dot{d}}{M} \tag{27}$$

Reformulating Eq. (27) based on Eq. (16) with respect to d , one obtains the Ginzburg-Landau-like evolution equation

$$\frac{\dot{d}}{M} = -2d\psi_e(\boldsymbol{\epsilon}) + g_c \left[\frac{1}{2\epsilon} (1 - d) + 2\epsilon \text{div}(\text{grad } d) \right] \tag{28}$$

Note that all approaches lead to identical thermodynamically consistent results but highlight different conceptual perspectives.

NUMERICAL EXAMPLE

The numerical implementation into OpenGeoSys follows Gerasimov (2016) and is verified against a one-dimensional quasi-static beam model with an analytical solution stated in Kuhn (2013) to verify the phase-field implementation. A beam is stretched by a prescribed displacement load applied to its two tips, see, Fig. 2.

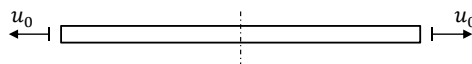


Figure 2: One-dimensional beam model.

Due to the symmetry of the boundary conditions, Fig. 3 only plots the phase-field parameter and displacement field distribution along a half beam. Comparisons of the analytical solution and the numerical approximation show the satisfactory match between these two solutions.

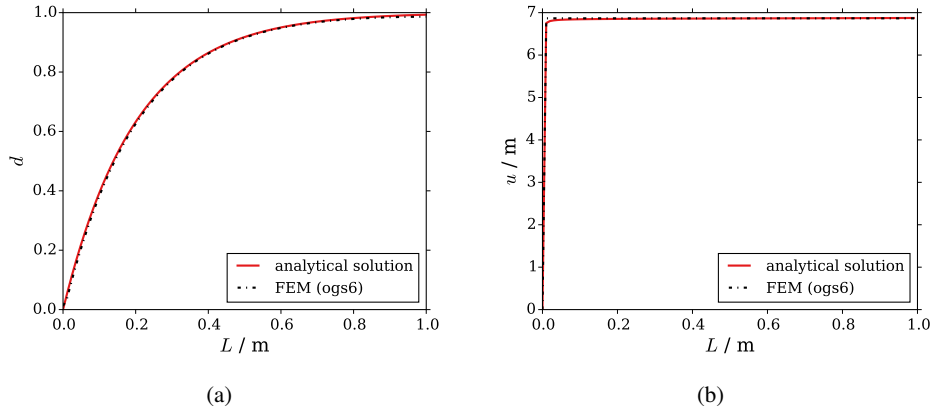


Figure 3: Phase-field parameter and displacement field distribution along the beam.

PHASE-FIELD MODELLING IN MULTI-PHYSICAL PROCESSES

To study how temperature and fluid-pressure fields affect the formation of cracks, and how the distribution of these field variables is affected by the presence of cracks, multi-physical aspects are incorporated into the framework. The thermo-hydraulic coupled phase-field approach is derived based on the Theory of Porous Media. Under the assumption of small deformations and brittle fracture, the Clausius-Planck inequality for the overall aggregate formulates, cf., Ehlers (2017),

$$\begin{aligned}
 & \left(\boldsymbol{\sigma}_S + \phi_S p \mathbf{I} - \varrho_S \frac{\partial \psi_S}{\partial \boldsymbol{\epsilon}_S} \right) : (\boldsymbol{\epsilon}_S)'_S - \left(\varrho_S \eta_S - p \frac{\phi_S}{\varrho_{SR0}} \frac{\partial \varrho_{SR}}{\partial T} + \varrho_S \frac{\partial \psi_S}{\partial T} \right) T'_S \\
 & + (\boldsymbol{\sigma}_F + \phi_F p \mathbf{I}) : \mathbf{d}_F - (\hat{\mathbf{p}}_F - p \text{grad } \phi_F) \cdot \mathbf{w}_F - \left(\varrho_F \eta_F - p \frac{\phi_F}{\varrho_{FR0}} \frac{\partial \varrho_{FR}}{\partial T} + \varrho_F \frac{\partial \psi_F}{\partial T} \right) T'_F \\
 & - \varrho_S \left[\frac{\partial \psi_S}{\partial d_S} - \text{div} \left(\frac{\partial \psi_S}{\partial \text{grad } d_S} \right) \right] (d_S)'_S - \varrho_S \text{div} \left(\frac{\partial \psi_S}{\partial \text{grad } d_S} (d_S)'_S \right) \geq 0 \quad (29)
 \end{aligned}$$

where ϕ_S and ϕ_F represents the volume fraction for solid and fluid, respectively. $(\cdot)'_S = \partial(\cdot)/\partial t + \text{grad}(\cdot) \cdot \mathbf{v}_S$ is the material time derivative of a quantity with respect to the solid motion. The extra solid and fluid stresses and entropy and the extra fluid momentum production are defined as

$$\boldsymbol{\sigma}_S^E = \boldsymbol{\sigma}_S + \phi_S p \mathbf{I}, \quad \boldsymbol{\sigma}_F^E = \boldsymbol{\sigma}_F + \phi_F p \mathbf{I} \quad (30)$$

$$\eta_S^E = \eta_S - \frac{p}{(\varrho_{SR})^2} \frac{\partial \varrho_{SR}}{\partial T}, \quad \eta_F^E = \eta_F - \frac{p}{(\varrho_{FR})^2} \frac{\partial \varrho_{FR}}{\partial T} \quad (31)$$

$$\hat{\mathbf{p}}_F^E = \hat{\mathbf{p}}_F - p \text{grad } \phi_F \quad (32)$$

To fulfill the inequality, the constitutive equation is found as

$$\boldsymbol{\sigma}_S^E = \varrho_S \frac{\partial \psi_S}{\partial \boldsymbol{\epsilon}_S} \quad (33)$$

and the boundary condition

$$\frac{\partial \psi_S}{\partial \text{grad } d_S} \cdot \mathbf{n} = 0 \tag{34}$$

the non-equilibrium conditions, cf., Ehlers (2017)

$$\boldsymbol{\sigma}_F^E = 2(1 - d_S)^2 \phi_F \mu_{FR} \mathbf{d}_F \tag{35}$$

$$\hat{\mathbf{p}}_F^E = - (d_S)^2 (\phi_F)^2 \mu_{FR} \mathbf{K}_S^{-1} \mathbf{w}_F \tag{36}$$

as well as the evolution equation

$$\frac{(d_S)'_S}{M} = \varrho_S \left[\frac{\partial \psi_S}{\partial d_S} - \text{div} \left(\frac{\partial \psi_S}{\partial \text{grad } d_S} \right) \right] \tag{37}$$

where μ_{FR} is the effective dynamic viscosity of the pore fluid, \mathbf{K}_S the intrinsic permeability. The Helmholtz free energy functions for solid and fluid phase are introduced as

$$\begin{aligned} \varrho_{S0} \psi_S(\boldsymbol{\epsilon}_S, d_S, \text{grad } d_S, T) &= [(d_S)^2 + k] (\psi_{Se})^+(\boldsymbol{\epsilon}_S) + (\psi_{Se})^-(\boldsymbol{\epsilon}_S) \\ &\quad - 3\alpha_{TS} K_S (T - T_{S0}) \boldsymbol{\epsilon}_S : \mathbf{I} + g_{Sc} \left[\frac{1}{4\varepsilon} (1 - d_S)^2 + \varepsilon \text{grad } d_S \cdot \text{grad } d_S \right] \\ &\quad - \varrho_{S0} c_S^E \left(T \ln \frac{T}{T_{S0}} - T + T_{S0} \right) - \varrho_{S0} \eta_{S0} (T - T_{S0}) \end{aligned} \tag{38}$$

$$\varrho_{F0} \psi_F(T) = -\varrho_{F0} c_F^E \left(T \ln \frac{T}{T_{F0}} - T + T_{F0} \right) - \varrho_{F0} \eta_{F0} (T - T_{F0}) \tag{39}$$

The governing partial differential equations read (cf., Ehlers (2017))

Mixture volume balance:

$$\text{div}(\mathbf{v}_S + \phi_F \mathbf{w}_F) - (\phi_S 3\alpha_{TS} + \phi_F \beta_{TF}) (T)'_S - \phi_F \beta_{TF} \text{grad } T \cdot \mathbf{w}_F = 0 \tag{40}$$

Momentum balance for solid phase:

$$\varrho_S (\mathbf{v}_S)'_S = \text{div} \boldsymbol{\sigma}_S^E - \phi_S \text{grad } p + \varrho_S \mathbf{g} - \hat{\mathbf{p}}_F^E \tag{41}$$

Momentum balance for fluid phase:

$$\varrho_F (\mathbf{v}_F)'_F = \text{div} \boldsymbol{\sigma}_F^E - \phi_F \text{grad } p + \varrho_F \mathbf{g} - \hat{\mathbf{p}}_F^E \tag{42}$$

Mixture energy balance:

$$(\varrho c_p)_{\text{eff}} \frac{\partial T}{\partial t} + \phi_F \varrho_{FR} c_{pF} \text{grad } T \cdot \mathbf{w}_F - \text{div}(\boldsymbol{\lambda}_{\text{eff}} \text{grad } T) = 0 \tag{43}$$

Evolution equation for phase-field:

$$\frac{(d_S)'_S}{M} = 2d_S (\psi_{Se})^+(\boldsymbol{\epsilon}_S) + g_{Sc} \left[\frac{1}{2\varepsilon} (1 - d_S) + 2\varepsilon \text{div}(\text{grad } d_S) \right] \tag{44}$$

CONCLUSION

In this contribution, a continuum phase-field model of brittle fracture was presented. To offer physical insight to the interested reader, three treatments for obtaining the evolution equation of the phase-field were summarised. The direct incentive of developing a phase-field model is to allow the assessment for the crack formation and evolution in porous storage material under multi-physical conditions. The model implementation was outlined and the pure mechanical case was verified through comparing with an analytical solution.

REFERENCES

- Ambrosio, L., Tortorelli, V. M., 1990. Approximation of functional depending on jumps by elliptic functional via Γ -convergence. *Communications on Pure and Applied Mathematics* 43 (8), 999-1036.
- Ehlers, W., Luo, C., 2017. A phase-field approach embedded in the theory of porous media for the description of dynamic hydraulic fracturing. *Computer Methods in Applied Mechanics and Engineering* 315, 3483-368.
- Gerasimov, T., De Lorenzis, L., 2016. A line search assisted monolithic approach for phase-field computing of brittle fracture. *Computer Methods in Applied Mechanics and Engineering* 312, 2763-303.
- Gurtin, M. E., 2008. *Configurational forces as basic concepts of continuum physics*. Vol. 137. Springer Science & Business Media.
- Kuhn, C., 2013. Numerical and analytical investigation of a phase field model for fracture. Ph.D. thesis, Technische Universität Kaiserslautern.
- Miao, X.-Y., Beyer, C., Grke, U.-J., Kolditz, O., Hailemariam, H., Nagel, T., 2016. Thermo-hydro-mechanical analysis of cement-based sensible heat stores for domestic applications. *Environmental Earth Sciences* 75 (18), 1293.
- Miao, X.-Y., Zheng, T., Grke, U.-J., Kolditz, O., Nagel, T., 2017. Thermo-mechanical analysis of heat exchanger design for thermal energy storage systems. *Applied Thermal Engineering* 114, 1082-1089.
- Miehe, C., Welschinger, F., Hofacker, M., 2010. Thermodynamically consistent phase-field models of fracture: Variational principles and multi-field fe implementations. *International Journal for Numerical Methods in Engineering* 83 (10), 1273-1311.

2.5 Phase-field modelling of fracture in thermo-elastic solids

X.-Y. Miao, T. Zheng, O. Kolditz, T. Nagel, Phase-field modeling of cracking processes in geomaterials for subsurface geotechnical engineering and energy storage. *Advance of Computer Methods in Geomechanics: Proceedings of the fifteenth International Conference of the International Association for Computer Methods and Advanced in Geomechanics*, Wuhan, China, October 19-23, 2017, accepted.

Phase-field modeling of cracking processes in geomaterials for subsurface geotechnical engineering and energy storage

Xing-Yuan Miao^{ab*}, Tianyuan Zheng^{ab}, Olaf Kolditz^{ab}
and Thomas Nagel^{ac}

^aHelmholtz Centre for Environmental Research – UFZ, Leipzig, Germany

^bTechnische Universität Dresden, Germany

^cTrinity College Dublin, College Green, Dublin, Ireland

*xing-yuan.miao@ufz.de

Abstract

This contribution presents the development of a fully coupled phase-field model for brittle fracture of solids subject to thermo-mechanical loading. The phase-field approach treats the discontinuity at the discrete lower-dimensional crack interface in a continuous diffusive setting. The system of equations is treated numerically by a monolithically coupled Newton-Raphson iterative-incremental solution strategy implemented into the scientific open-source finite element software OpenGeoSys. This contribution presents the governing equations along with details of said numerical implementation together with initial verification examples and perspectives for model application.

Keywords: Phase-field, Brittle fracture, Monolithic coupling, Thermal cracking, OpenGeoSys

1. Introduction

Fractures in geological materials have a dominating impact on the success of geotechnical engineering applications associated with the energy sector such as geothermal reservoirs, carbon dioxide sequestration, shale gas production and subsurface energy storage. Fractures induced by multi-physical effects based on external stimulation can have both advantages and disadvantages in energy geotechnics. On the one hand, both natural and artificial fracture networks provide efficient flow circuits for heat/fluid storage, injection or extraction, enhancing the productivity and sustainability of the geotechnical applications. On the other hand, the long-term stability of a geotechnical component as well as the load-carrying capacity of the surrounding geomaterials may be challenged due to unintended or secondary fractures caused by, e.g., cyclic loads imposed onto the system. Insufficient knowledge on existing fractures, a lack of control over the emergence of new ones or the over-stimulation of reservoirs for productivity enhancements can have detrimental consequences endangering not only the entire project but also the environment, such as contaminant leakage, a desta-

bilisation of the stratum, or induced local seismicity.

Using a phase-field approach for the numerical treatment of crack evolution has a number of attractive features. The principal highlight of this approach is that it describes the crack interface from a continuous configurational perspective by introducing a phase-indicator variable that smoothly transitions between the undamaged material phase and the crack domain and evolves with the crack. Phase-field models and numerical implementations of brittle fracture based on variational principles were presented by [2, 3, 11] and others.

The motivation of this work is to study the morphogenesis and the propagation regimes of complex crack patterns in geotechnical components in a thermo-mechanical setting in which cracks may be induced both by external loading as well as by incompatible strains associated with temperature gradients. For that purpose, a thermo-mechanically coupled phase-field model is implemented into the scientific open-source finite element framework OpenGeoSys [6]. The subjects of this research are (i) to explore effects of fractures in terms of performance enhancement or degradation of engineered subsurface energy systems; (ii) to identify how the operation of the geotechnical system involving subsurface fracture networks potentially affects the environment below and above ground. The study of fractures induced by critical tensile stresses within a cement-based heat storage material used in an intelligent thermal energy storage system [8, 9] serves as a first test case.

2. Numerical treatment

2.1. Model formulation

We introduce firstly definitions and notations of the variational formulation. Let $\Omega \subset \mathcal{R}^D$ be the reference configuration of a material body in dimension $D \in [2, 3]$ and $\partial\Omega \subset \mathcal{R}^{D-1}$ its external boundary with $\partial\Omega_u$ and $\partial\Omega_t$ the Dirichlet and Neumann boundaries, respectively, such that both $\partial\Omega_u \cup \partial\Omega_t = \partial\Omega$ and $\partial\Omega_u \cap \partial\Omega_t = \emptyset$ holds. $\Gamma \subset \mathcal{R}^{D-1}$ is the inserted sharp crack surface, see, Fig. 1a. The inserted sharp crack surface can be regularised as a diffusive topology in relation to an order parameter d , Eq. (1), to create a transition phase between the damaged and intact part of material, see, Fig. 1b and reference [11].

$$\Gamma_\varepsilon(d) = \int_{\Omega} \gamma dV = \int_{\Omega} \left[\frac{1}{4\varepsilon} (1-d)^2 + \varepsilon \text{grad } d \cdot \text{grad } d \right] dV \quad (1)$$

where ε is the length-scale parameter controlling the regularisation.

To study how temperature fields affect the formation of cracks, thermally induced strains and thermo-mechanical coupling are incorporated into the framework within a kinematically linear setting. The total strain is composed of the elastic and thermal part

$$\boldsymbol{\epsilon} = \boldsymbol{\epsilon}_{\text{el}} + \boldsymbol{\epsilon}_{\text{th}} \quad (2)$$

with

$$\boldsymbol{\epsilon}_{\text{th}} = \alpha \Delta T \quad (3)$$

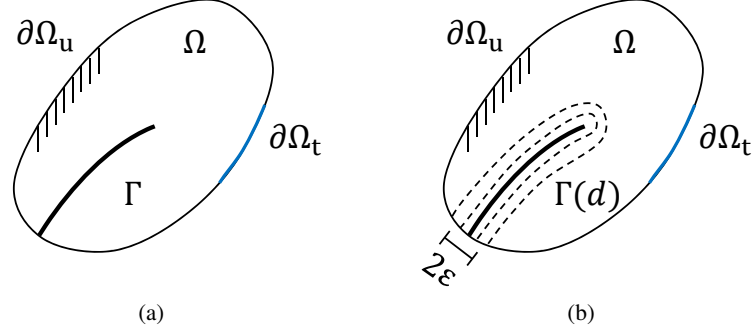


Figure 1: Elastic body with: (a) sharp crack; (b) diffusive crack characterised by a length scale parameter 2ε .

where α stands for the linear thermal expansion tensor. Only the elastic part contributes to the elastic energy density

$$\psi_e^+(\boldsymbol{\epsilon}_{el}) := \frac{1}{2}K \langle \text{tr}(\boldsymbol{\epsilon} - \boldsymbol{\epsilon}_{th}) \rangle_+^2 + \mu(\boldsymbol{\epsilon} - \boldsymbol{\epsilon}_{th})^D : (\boldsymbol{\epsilon} - \boldsymbol{\epsilon}_{th})^D \quad (4)$$

$$\psi_e^-(\boldsymbol{\epsilon}_{el}) := \frac{1}{2}K \langle \text{tr}(\boldsymbol{\epsilon} - \boldsymbol{\epsilon}_{th}) \rangle_-^2 \quad (5)$$

where K is the bulk modulus, μ the shear modulus, and $\langle \bullet \rangle_{\pm} := (\bullet \pm |\bullet|) / 2$.

In accordance with physical observations in many materials, compression perpendicular to a crack does not cause crack propagation, but rather closes the crack (contact of the crack faces). To distinguish between tensile and compressive contributions to the degradation of the elastic energy, the undamaged elastic energy density has been decomposed here based on a split into volumetric and deviatoric parts, cf. [1].

Summing the stored elastic energy and the crack-surface energy, the total energy functional of a fractured body can be formulated as

$$E(\mathbf{u}, \text{grad } \mathbf{u}, d) = \int_{\Omega} \left[(d^2 + k) \psi_e^+(\boldsymbol{\epsilon}_{el}) + \psi_e^-(\boldsymbol{\epsilon}_{el}) \right] dV + g_c \int_{\Omega} \left[\frac{1}{4\varepsilon} (1 - d)^2 + \varepsilon \text{grad } d \cdot \text{grad } d \right] dV \quad (6)$$

where k represents a residual stiffness used in numerical calculations to ensure a residual elastic energy density in the fully damaged state. The parameter g_c stands for the critical Griffith-type fracture energy release rate. The order parameter d is constrained between 0 (fully damaged) and 1 (intact material).

To formulate the governing equations, we further consider the external mechanical work functional

$$W_{\text{ext}}(\mathbf{u}) = \int_{\partial\Omega_t} \bar{\mathbf{t}} \cdot \mathbf{u} dA + \int_{\Omega} \varrho \mathbf{b} \cdot \mathbf{u} dV \quad (7)$$

where $\bar{\mathbf{t}}$ is the surface traction on $\partial\Omega_t$, \mathbf{b} the specific body force.

Based on the potential

$$\Pi = E(\mathbf{u}, \text{grad } \mathbf{u}, d) - W_{\text{ext}}(\mathbf{u}), \quad (8)$$

the equilibrium equations for a quasi-static process can be found by the variation

$$\delta\Pi = \frac{\partial\Pi}{\partial\mathbf{u}} \cdot \delta\mathbf{u} + \frac{\partial\Pi}{\partial d} \delta d = 0 \quad (9)$$

where the individual terms evaluate to

$$\begin{aligned} \frac{\partial\Pi}{\partial\mathbf{u}} \cdot \delta\mathbf{u} = & - \int_{\Omega} \text{div} \left[(d^2 + k) \boldsymbol{\sigma}_0^+ + \boldsymbol{\sigma}_0^- \right] \cdot \delta\mathbf{u} dV + \int_{\partial\Omega_t} \left[(d^2 + k) \boldsymbol{\sigma}_0^+ + \boldsymbol{\sigma}_0^- \right] \mathbf{n} \cdot \delta\mathbf{u} dA \\ & - \int_{\partial\Omega_t} \bar{\mathbf{t}} \cdot \delta\mathbf{u} dA - \int_{\Omega} \boldsymbol{\rho}\mathbf{b} \cdot \delta\mathbf{u} dV \end{aligned} \quad (10)$$

$$\begin{aligned} \frac{\partial\Pi}{\partial d} \delta d = & \int_{\Omega} 2d\psi_e^+(\boldsymbol{\epsilon}_{\text{el}}) \delta d dV - \int_{\Omega} \frac{1-d}{2\varepsilon} g_c \delta d dV + \int_{\partial\Omega} 2\varepsilon g_c \text{grad } d \cdot \mathbf{n} \delta d dA \\ & - \int_{\Omega} 2\varepsilon g_c \text{div}(\text{grad } d) \delta d dV \end{aligned} \quad (11)$$

Thus, we obtain the following set of PDEs in the case of thermo-elastic deformation and brittle fracture along with the respective Neumann-type boundary conditions

$$\text{div} \left[(d^2 + k) \boldsymbol{\sigma}_0^+ + \boldsymbol{\sigma}_0^- \right] + \boldsymbol{\rho}\mathbf{b} = \mathbf{0} \quad (12)$$

$$2d\mathcal{H}(\boldsymbol{\epsilon}_{\text{el}}) - \frac{1-d}{2\varepsilon} g_c - 2\varepsilon g_c \text{div}(\text{grad } d) = 0 \quad (13)$$

$$(\rho c_p)_{\text{eff}} \frac{\partial T}{\partial t} - \text{div}(\lambda_{\text{eff}} \text{grad } T) = 0 \quad (14)$$

$$\left[(d^2 + k) \boldsymbol{\sigma}_0^+ + \boldsymbol{\sigma}_0^- \right] \cdot \mathbf{n} - \bar{\mathbf{t}} = \mathbf{0} \quad \text{on } \partial\Omega_t \quad (15)$$

$$\text{grad } d \cdot \mathbf{n} = 0 \quad \text{on } \partial\Omega \quad (16)$$

$$-\mathbf{q} \cdot \mathbf{n} - \bar{q}_n = 0 \quad \text{on } \partial\Omega_q \quad (17)$$

where the heat conduction equation has been added for the determination of the temperature field and in which $(\rho c_p)_{\text{eff}}$ represents the effective volumetric heat capacity, λ_{eff} the thermal conductivity tensor, and \mathbf{q} the heat flux. Note further, that in Eq. (13), a damage-driving history field associated with the maximum local tensile strain energy has been used instead of ψ_e^+ to ensure irreversibility of the crack propagation by preventing crack healing [10]. This history field stores the maximum positive strain energy achieved during the deformation history and governs the evolution equation for phase-field:

$$\mathcal{H}(\mathbf{x}, t) := \max_{s \in [0, t]} \psi_e^+(\boldsymbol{\epsilon}_{\text{el}}, s) \quad (18)$$

In addition, to take into account the degradation of the heat conductivity within the crack field, the effective heat conductivity is defined as (cf., [7])

$$\lambda_{\text{eff}} = \left\{ H[\text{tr}(\boldsymbol{\epsilon}_{\text{el}})] (d^2 + k_\lambda - 1) + 1 \right\} \lambda \quad (19)$$

where $H[\bullet]$ is the Heaviside step function and k_λ is the (residual) thermal conductivity of the cracked material which depends on the surrounding medium (e.g. air, water, thermal oil, etc.). At this stage, similar effects related to the volumetric heat capacity have been neglected.

2.2. Weak forms

For the numerical implementation, we derive the weak forms of the governing PDEs with test functions v_u , v_d and v_T .

- Momentum balance:

$$\int_{\Omega} (\text{grad } v_u)^T : \boldsymbol{\sigma} \, dV - \int_{\Omega} \varrho v_u \cdot \mathbf{b} \, dV - \int_{\partial\Omega_t} v_u \cdot \bar{\mathbf{t}} \, dA = 0 \quad (20)$$

with

$$\boldsymbol{\sigma} := (d^2 + k) \frac{\partial \psi_e^+(\boldsymbol{\epsilon}_{\text{el}})}{\partial \boldsymbol{\epsilon}_{\text{el}}} + \frac{\partial \psi_e^-(\boldsymbol{\epsilon}_{\text{el}})}{\partial \boldsymbol{\epsilon}_{\text{el}}} \quad (21)$$

$$:= (d^2 + k) \left[K \langle \text{tr}(\boldsymbol{\epsilon}_{\text{el}}) \rangle_+ \mathbf{I} + 2\mu \boldsymbol{\epsilon}_{\text{el}}^D \right] + K \langle \text{tr}(\boldsymbol{\epsilon}_{\text{el}}) \rangle_- \mathbf{I} \quad (22)$$

- Evolution equation for phase-field:

$$\int_{\Omega} \left\{ v_d \frac{\dot{d}}{M} + \text{grad } v_d \cdot 2g_c \varepsilon \text{ grad } d + v_d \left[2d \mathcal{H}(\boldsymbol{\epsilon}_{\text{el}}) - \frac{g_c}{2\varepsilon} (1-d) \right] \right\} dV = 0 \quad (23)$$

where damping was introduced by $\dot{d} = -M \frac{\delta \psi}{\delta d}$, with M a kinetic coefficient. This Ansatz can be defined to address rate-dependent settings or simply to improve numerical stability. $M \rightarrow \infty$ recovers the rate-independent state.

- Heat conduction

$$\int_{\Omega} v_T \varrho c \dot{T} \, dV + \int_{\Omega} \text{grad } v_T \cdot \lambda_{\text{eff}} \text{ grad } T \, dV = 0 \quad (24)$$

Finite element approximations to displacements, crack field and their respective test functions are denoted by

$$\begin{aligned} u_i &= N_{ij}^u \hat{u}_j & d &= N_i^d \hat{d}_i & T &= N_i^T \hat{T}_i \\ (v_u)_i &= N_{ij}^{v_u} (\hat{v}_u)_j & v_d &= N_i^{v_d} (\hat{v}_d)_i & v_T &= N_i^{v_T} (\hat{v}_T)_i \\ \text{sym grad } u_\alpha &= B_{\alpha j}^u \hat{u}_j & \text{grad } d_i &= \nabla N_{ij}^d \hat{d}_j & \text{grad } T_i &= \nabla N_{ij}^T \hat{T}_j \\ \text{sym grad } (v_u)_\alpha &= B_{\alpha j}^{v_u} (\hat{v}_u)_j & \text{grad } (v_d)_i &= \nabla N_{ij}^{v_d} (\hat{v}_d)_j & \text{grad } (v_T)_i &= \nabla N_{ij}^{v_T} (\hat{v}_T)_j \end{aligned} \quad (25)$$

So that the discrete forms of Eqs. (20) and (23) read

$$\Psi_i^u = \underbrace{\int_{\Omega} B_{\alpha i}^{v_u} \sigma_\alpha \, dV}_{P_i^u} - \int_{\partial\Omega_t} N_{ij}^{v_u} \bar{t}_j \, dA - \int_{\Omega} N_{ij}^{v_u} \varrho b_j \, dV \quad (26)$$

$$\Psi_i^d = \underbrace{\int_{\Omega} N_i^{v_d} \frac{\dot{d}}{M} \, dV + \int_{\Omega} \nabla N_{ij}^{v_d} 2g_c \varepsilon \text{ grad } d \, dV + \int_{\Omega} N_i^{v_d} 2d \mathcal{H} \, dV - \int_{\Omega} N_i^{v_d} \frac{g_c}{2\varepsilon} (1-d) \, dV}_{P_i^d} \quad (27)$$

$$\Psi_i^T = \underbrace{\int_{\Omega} N_i^{v_T} \varrho c \dot{T} \, dV + \int_{\Omega} \nabla N_{ij}^{v_T} \lambda_{\text{eff}} \text{ grad } T \, dV}_{P_i^T} \quad (28)$$

A linearisation within an incremental-iterative Newton-Raphson scheme in conjunction with the implicit backward-Euler method for time discretisation yields the discrete linearized matrix-vector system

$$\begin{bmatrix} K_{ij}^{uu} & K_{ij}^{ud} & K_{ij}^{uT} \\ K_{ij}^{du} & K_{ij}^{dd} + \frac{D_{ij}^{dd}}{\Delta t} & K_{ij}^{dT} \\ K_{ij}^{Tu} & K_{ij}^{Td} & K_{ij}^{TT} + \frac{D_{ij}^{TT}}{\Delta t} \end{bmatrix} \begin{bmatrix} \Delta \hat{u}_j \\ \Delta \hat{d}_j \\ \Delta \hat{T}_j \end{bmatrix} = \begin{bmatrix} -\Psi_i^u \\ -\Psi_i^d \\ -\Psi_i^T \end{bmatrix} \quad (29)$$

where

$$K_{ij}^{uu} = \frac{\partial P_i^u}{\partial u_j} = \int_{\Omega} B_{\alpha i}^{v_u} [(d^2 + k) D_{0\alpha\beta}^+ + D_{0\alpha\beta}^-] B_{\beta j}^u dV \quad (30)$$

$$K_{ij}^{ud} = \frac{\partial P_i^u}{\partial d_j} = \int_{\Omega} B_{\alpha i}^{v_u} 2d\sigma_{0\alpha}^+ N_j^d dV \quad (31)$$

$$K_{ij}^{uT} = \frac{\partial P_i^u}{\partial T_j} = - \int_{\Omega} B_{\alpha i}^{v_u} [(d^2 + k) D_{0\alpha\beta}^+ + D_{0\alpha\beta}^-] \alpha I_{\beta} N_j^T dV \quad (32)$$

$$K_{ij}^{du} = \frac{\partial P_i^d}{\partial u_j} = \int_{\Omega} N_i^{v_d} H [\psi_e^+ - \mathcal{H}_n] 2d\sigma_{0\alpha}^+ B_{\alpha j}^u dV \quad (33)$$

$$K_{ij}^{dd} = \frac{\partial P_i^d}{\partial d_j} = \int_{\Omega} \nabla N_{\alpha i}^{v_d} 2g_c \varepsilon \nabla N_{\alpha j}^d dV + \int_{\Omega} N_i^{v_d} 2\mathcal{H} + N_j^d dV + \int_{\Omega} N_i^{v_d} \frac{g_c}{2\varepsilon} N_j^d dV \quad (34)$$

$$K_{ij}^{dT} = \frac{\partial P_i^d}{\partial T_j} = - \int_{\Omega} N_i^{v_d} H [\psi_e^+ - \mathcal{H}_n] 2d\sigma_{0\alpha}^+ \alpha I_{\alpha} N_j^d dV \quad (35)$$

$$K_{ij}^{Td} = \frac{\partial P_i^T}{\partial d_j} = \int_{\Omega} \nabla N_{\alpha i}^{v_T} H [\text{tr}(\epsilon_{el})] 2d\lambda \text{grad} T N_{\alpha j}^d dV \quad (36)$$

$$K_{ij}^{TT} = \frac{\partial P_i^T}{\partial T_j} = \int_{\Omega} \nabla N_{\alpha i}^{v_T} \lambda_{\text{eff} \alpha\beta} \nabla N_{\beta j}^T dV \quad (37)$$

$$D_{ij}^{dd} = \frac{\partial P_i^d}{\partial \hat{d}_j} = \int_{\Omega} N_i^{v_d} \frac{1}{M} N_j^d dV \quad (38)$$

$$D_{ij}^{TT} = \frac{\partial P_i^T}{\partial \hat{T}_j} = \int_{\Omega} N_i^{v_T} \varrho c N_j^T dV \quad (39)$$

3. Numerical verification

3.1. Cracking bar under tension

The numerical implementation for phase-field modelling in the framework of isotropic linear elasticity is verified against a one-dimensional quasi-static beam model with an analytical solution stated

in [7]. Fig. 2 illustrates the geometry and boundary conditions of the beam model. Equivalent displacement loads are applied to both sides. The material properties, geometrical and part of numerical settings are listed in Table 1. Note, that all numerical examples presented in this section share the same material properties while different geometrical sizes, boundary conditions and loadings. A discretisation of 100 quadratic elements with the element length of 0.01 mm is applied for the beam model.

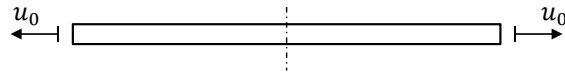


Figure 2: One-dimensional beam model.

Fig. 3 compares the approximated phase-field parameter and displacement field distribution along a half beam to the analytical solution. Results show satisfactory agreement.

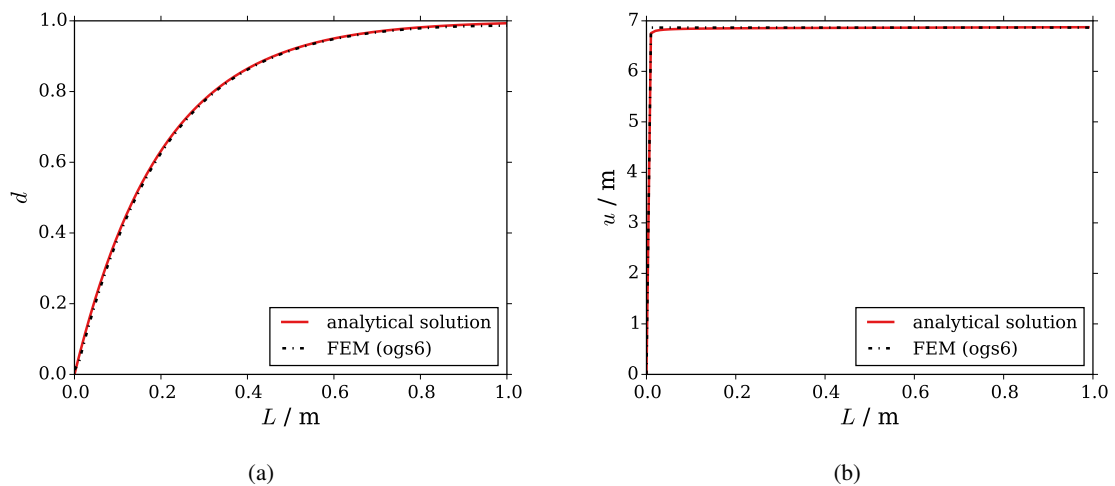


Figure 3: Phase-field parameter and displacement field distribution along the beam.

3.2. Single-edge-notch tensile test

A classical single-edge-notched tension test (see, Fig. 4) often used in literature for testing crack propagation models (cf., [11, 4]) was chosen to provide another verification example for the implemented algorithm. The mesh was refined a priori in the region through which the crack is expected to propagate. The geometry of the model is described in Table 1. The displacement loading was applied in increments of $\delta u = 1 \cdot 10^{-5}$ mm prescribed on the upper edge of the specimen. The mesh contained 20,094 triangular elements with a minimum mesh size of approximately 0.001 mm within the expected crack region.

Table 1: Parameters for numerical examples.

Material properties	Young's Modulus E (GPa)	Poisson's ratio ν	Crack resistance g_c (N mm ⁻¹)
	210	0.3	2.7
Geometry	length (mm)	width (mm)	
beam	1	-	
single-edge-notched	1	1	
Numerical settings	residual stiffness k	length scale 2ϵ (mm)	kinetic coefficient M (mm ² N ⁻¹ s ⁻¹)
beam	$1 \cdot 10^{-3}$	0.04	$1 \cdot 10^6$
single-edge-notched	$1 \cdot 10^{-3}$	0.03	$2 \cdot 10^{-4}$

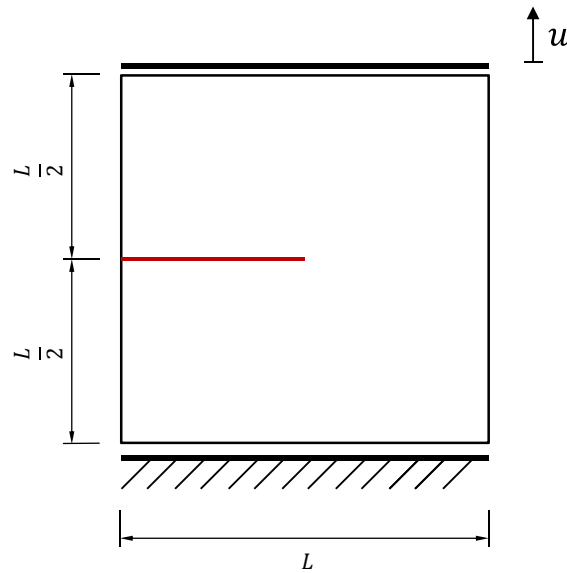


Figure 4: Single-edge-notched model.

Fig. 5a shows both the horizontal pre-existing crack as well as its propagation along a straight path through the material as predicted by the phase-field model. In addition, the load-displacement curve for the upper edge is illustrated in Fig. 5b. Both the crack propagation and the load-displacement patterns are consistent with the literature, cf. [11, 4].

3.3. Thermal cracking test

The following numerical examples are used to verify the numerical implementation for phase-field modelling in using thermo-mechanical coupling. For that purpose, an unconfined compression test is simulated in a purely mechanical setting with a compressive displacement load applied to the upper surface of the model, see Fig. 6a. It is then compared to an axially constrained thermal expansion model where an axial elastic strain is imposed analogously to unconfined compression by means of

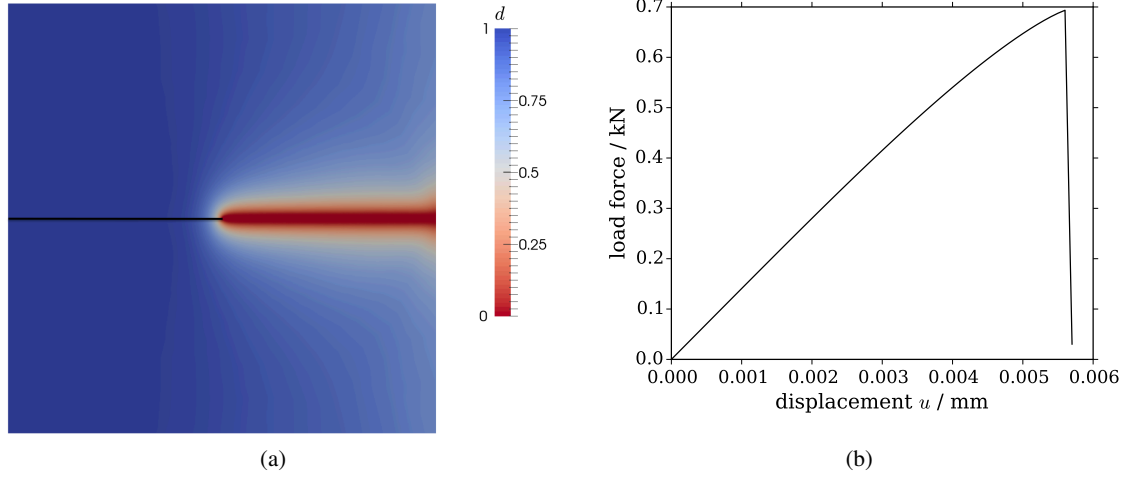


Figure 5: Single-edge-notched tension test: (a) crack propagation pattern; (b) load - displacement curve.

imposing a temperature increase while the top surface is held in place. The temperature load is set to achieve the same axial elastic compression as that imposed in the unconfined compression test. Both models are free to expand in the depth direction. Fig. 6b indicates the boundary constraints for the thermal expansion model. Both models are simulated based on a single three-dimensional element. Because of the homogeneous evolution of the phase field ($\text{div grad } d = 0$), the phase-field parameter can be determined analytically to

$$d = \frac{g_c}{g_c + 4\epsilon\psi_e^+} \quad (40)$$

where due to negative (elastic) volume strains only the deviatoric energy drives the phase field.

$$\psi_e^+ = \begin{cases} \mu \epsilon^D : \epsilon^D = \frac{2\mu}{3} \left(\frac{u(1+\nu)}{L} \right)^2 & \text{mechanical case} \\ \mu \epsilon_{el}^D : \epsilon_{el}^D = \frac{2\mu}{3} [\alpha\Delta T(1+\nu)]^2 & \text{thermo-mechanical case} \end{cases} \quad (41)$$

Note, that the Poisson's ratio is evolving as also only the shear modulus is degraded. Hence,

$$\nu(d) = \frac{3K - 2Gd^2}{2(3K + Gd^2)} \quad (42)$$

The phase-field evolution in both tests is expected to be identical for $\alpha = 10^{-3}$. This result is confirmed by the numerical simulations (Fig. 7).

4. Conclusions

In this contribution, a thermal coupled phase-field model for brittle fracture has been presented. A monolithic algorithm with a tension-compression split of the elastic strain energy has been im-

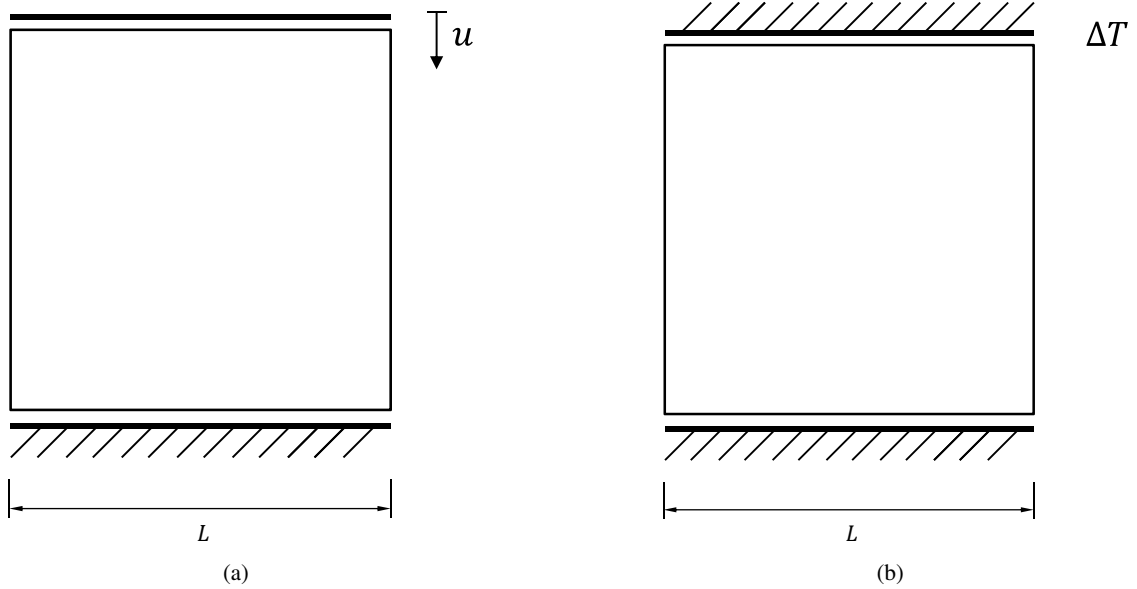


Figure 6: Geometry and boundary conditions: (a) unconfined compression test; (b) thermal expansion test.

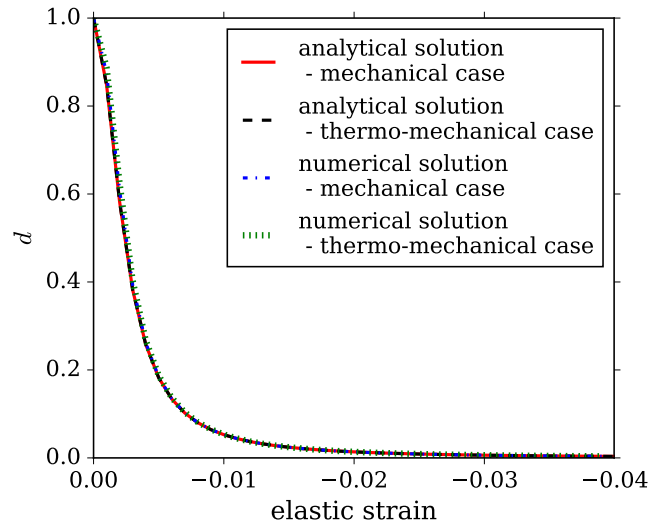


Figure 7: Phase-field - elastic strain curve.

plemented into the scientific open-source finite element platform OpenGeoSys [5]. A local history field associated with the maximum positive elastic strain energy is used to govern the crack evolution. All derivatives necessary for the implementation including an analytical Jacobian have been provided. The implementation has been quantitatively verified in the context of pure mechanical

loading by comparison against an appropriate analytical solution as well as qualitatively by means of a single-edge-notched tension test. In particular, an unconfined compression test and a constrained thermal expansion test are performed to quantitatively demonstrate the modelling capacity of thermo-mechanical coupling effect for fracturing process.

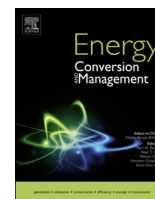
References

- [1] Amor, H., Marigo, J.-J., Maurini, C., 2009. Regularized formulation of the variational brittle fracture with unilateral contact: numerical experiments. *Journal of the Mechanics and Physics of Solids* 57 (8), 1209–1229.
- [2] Bourdin, B., Francfort, G. A., Marigo, J.-J., 2000. Numerical experiments in revisited brittle fracture. *Journal of the Mechanics and Physics of Solids* 48 (4), 797–826.
- [3] Bourdin, B., Francfort, G. A., Marigo, J.-J., 2008. The variational approach to fracture. *Journal of Elasticity* 91 (1-3), 5–148.
- [4] Ehlers, W., Luo, C., 2017. A phase-field approach embedded in the theory of porous media for the description of dynamic hydraulic fracturing. *Computer Methods in Applied Mechanics and Engineering* 315, 348–368.
- [5] Kolditz, O., Bauer, S., Bilke, L., Böttcher, N., Delfs, J. O., Fischer, T., Görke, U. J., Kalbacher, T., Kosakowski, G., McDermott, C. I., Park, C. H., Radu, F., Rink, K., Shao, H., Shao, H. B., Sun, F., Sun, Y. Y., Singh, A. K., Taron, J., Walther, M., Wang, W., Watanabe, N., Wu, Y., Xie, M., Xu, W., Zehner, B., Sep. 2012. OpenGeoSys: an open-source initiative for numerical simulation of thermo-hydro-mechanical/chemical (THM/C) processes in porous media. *Environmental Earth Sciences* 67 (2), 589.
- [6] Kolditz, O., Görke, U.-J., Shao, H., Wang, W., 2012. *Thermo-Hydro-Mechanical-Chemical Processes in Porous Media: Benchmarks and Examples*. Vol. 86. Springer Science & Business Media.
- [7] Kuhn, C., 2013. Numerical and analytical investigation of a phase field model for fracture. Ph.D. thesis, Technische Universität Kaiserslautern.
- [8] Miao, X.-Y., Beyer, C., Görke, U.-J., Kolditz, O., Hailemariam, H., Nagel, T., 2016. Thermo-hydro-mechanical analysis of cement-based sensible heat stores for domestic applications. *Environmental Earth Sciences* 75 (18), 1293.
- [9] Miao, X.-Y., Zheng, T., Görke, U.-J., Kolditz, O., Nagel, T., 2017. Thermo-mechanical analysis of heat exchanger design for thermal energy storage systems. *Applied Thermal Engineering* 114, 1082–1089.
- [10] Miehe, C., Hofacker, M., Welschinger, F., 2010. A phase field model for rate-independent crack propagation: Robust algorithmic implementation based on operator splits. *Computer Methods in Applied Mechanics and Engineering* 199 (45), 2765–2778.

- [11] Miehe, C., Welschinger, F., Hofacker, M., 2010. Thermodynamically consistent phase-field models of fracture: Variational principles and multi-field fe implementations. *International Journal for Numerical Methods in Engineering* 83 (10), 1273–1311.

2.6 *Thermo-mechanical phase-field modelling of fracture for solid thermal energy storage*

X.-Y. Miao, O. Kolditz, T. Nagel, Modelling thermal performance degradation of high and low-temperature solid thermal energy storage due to cracking processes using a phase-field approach. *Energy Conversion and Management*, Volume 180, January 2019, Pages 977-989.



Modelling thermal performance degradation of high and low-temperature solid thermal energy storage due to cracking processes using a phase-field approach

Xing-Yuan Miao^{a,b,c,*}, Olaf Kolditz^{a,b}, Thomas Nagel^{a,d,1}

^a Department of Environmental Informatics, Helmholtz Centre for Environmental Research – UFZ, Permoserstr. 15, 04318 Leipzig, Germany

^b Applied Environmental Systems Analysis, Technische Universität Dresden, Germany

^c Department of Energy Conversion and Storage, Technical University of Denmark, Risø Campus, Frederiksborgvej 399, 4000 Roskilde, Denmark

^d Department of Mechanical and Manufacturing Engineering, School of Engineering, Trinity College Dublin, College Green, Dublin, Ireland



ARTICLE INFO

Keywords:

Phase-field
Brittle fracture
Thermal cracking
Thermal energy storage
OpenGeoSys

ABSTRACT

Solid heat storage is an attractive solution for a wider utilisation of solar power for domestic and commercial applications alike. Thermal efficiency and long-term stability are of major concern both scientifically and industrially. There are many aspects that influence the thermal performance of a specific solid thermal energy storage (TES), such as the energy storage capacity of its storage material, the characteristics of its heat transfer fluid, and the mechanical integrity of the solid storage medium. In the present study, we develop a thermo-mechanical phase-field approach to fracture in order to examine the thermal performance degradation of the solid sensible heat storage (SHS) caused by potential thermally induced cracking of the heat storage medium around the embedded heat exchangers. Two representative solid SHS structures are examined: one applied in a low-temperature setting, the other used at high temperature levels. In both cases, fracturing caused by the mismatch of thermal expansion coefficients of the storage medium and the heat exchanger occurs under certain conditions. The open fractures form a space that will be filled by a fluid whose nature is determined by the system concept and which may well have a low thermal conductivity. Hence, heat transfer can be disturbed in the damaged regions, causing high temperature anomalies, which further may lead to significant fluctuations/loss of heating power during the heating phase. In the two specific scenarios investigated here, the highest loss of heat flow was estimated to be 7.7% in the water-saturated low-temperature SHS and 20.5% in the high-temperature SHS.

1. Introduction

The utilisation of solar thermal energy in the energy system has gained extensive popularity as a consequence of the thrive for sustainable energy production and storage with a low environmental impact of engineered solutions (cf. [1,2]). Besides direct thermal use, concentrating solar power (CSP) technologies offer the ability to harvest solar thermal energy and convert it into electricity (see, Fig. 1). One of the principal hindrances that limits an economical application of CSP is the mismatch between the daily/monthly/annual energy supplies and the persistent energy demands (cf. [3–7]). To facilitate a reliable dispatch of CSP-based power systems, thermal energy storage

(TES) solutions can be integrated akin to a battery for the storage/release of surplus heat (cf. [7–14]). TES is a highly efficient and economical flexibility option for the management of the generated solar thermal power in order to satisfy power demand requirements during different periods.

Sensible heat storage (SHS) is one of the main technologies available for implementing TES. SHS is widely used in practical applications mostly due to its comparatively low investment cost and technical maturity (cf. [6,15–25], Fig. 1). It is based on directly storing/releasing the thermal energy by raising/lowering the temperature of a liquid or solid storage medium. The present article is focused on sensible heat storage via solid storage media.

* Corresponding author at: Department of Environmental Informatics, Helmholtz Centre for Environmental Research – UFZ, Permoserstr. 15, 04318 Leipzig, Germany.

E-mail address: xing-yuan.miao@ufz.de (X.-Y. Miao).

¹ Present address: Chair of Soil Mechanics and Foundation Engineering, Institute of Geotechnics, Technische Universität Bergakademie Freiberg, 09599 Freiberg, Germany.

Nomenclature		ϑ_0	reference temperature [K]
<i>Greek symbols</i>		<i>Operators</i>	
α_T	linear thermal expansion tensor [K^{-1}]	$\mathbf{a} \cdot \mathbf{b}$	dot product of \mathbf{a} and \mathbf{b}
ϵ	small strain tensor [-]	$\mathbf{A} : \mathbf{B}$	double contraction of \mathbf{A} and \mathbf{B}
ϵ	length-scale parameter [m]	$(\bullet)^D$	deviatoric part of a tensor
ϵ_{el}	elastic strain tensor [-]	div()	divergence operator
ϵ_{th}	thermal strain tensor [-]	grad()	gradient operator
γ	crack-surface density [m^{-1}]	$\langle \bullet \rangle_{\pm}$	Signed Macauley brackets: $\langle \bullet \rangle_{\pm} = [\bullet \mp \bullet]/2$
κ_{eff}	effective thermal conductivity tensor [$W m^{-1} K^{-1}$]	tr()	trace operator
κ_d	residual thermal conductivity of crack-phase [$W m^{-1} K^{-1}$]	<i>Roman symbols</i>	
κ	thermal conductivity tensor [$W m^{-1} K^{-1}$]	c_p	isobaric specific heat capacity [$J kg^{-1} K^{-1}$]
κ_s	thermal conductivity of intact storage medium [$W m^{-1} K^{-1}$]	d	crack-phase indicator [-]
μ	shear modulus [$N m^{-2}$]	E	Young's modulus. [$N m^{-2}$]
η	specific entropy [$J K^{-1} kg^{-1}$]	G_c	critical Griffith-type energy release rate [$J m^{-2}$]
ν	Poisson's ratio [-]	K	bulk modulus [$N m^{-2}$]
$\bar{\psi}$	specific Helmholtz free energy [$J kg^{-1}$]	K_{Ic}	critical stress intensity factor of mode I [$N m^{-3/2}$]
ψ	Helmholtz free energy density [$J m^{-3}$]	l_{ch}	material's internal length [m]
ψ_m	mechanical part of Helmholtz free energy density [$J m^{-3}$]	l_G	griffith length [m]
ψ_{surf}	crack surface energy density [$J m^{-3}$]	\mathbf{n}	outward unit normal vector [-]
ψ_{th}	thermal part of Helmholtz free energy density [$J m^{-3}$]	\mathbf{q}	heat flux [$W m^{-2}$]
σ	Cauchy stress tensor [$N m^{-2}$]	r	specific heat source [$W kg^{-1}$]
ϑ	absolute temperature [K]		

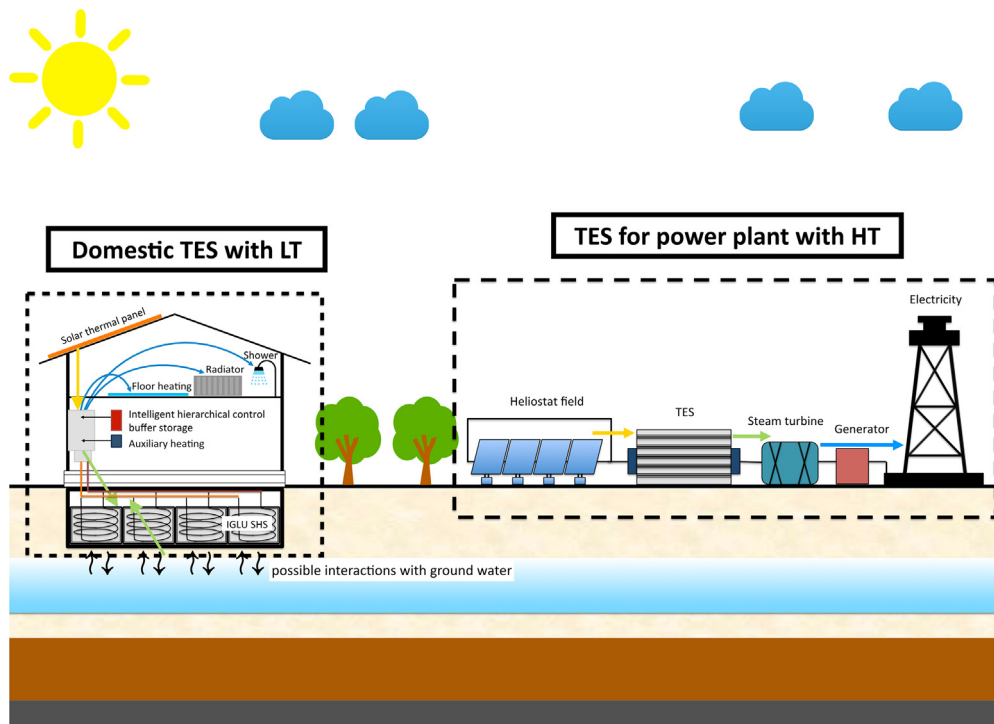


Fig. 1. Design and construction of solid TES systems for specific applications. (a) TES operating at low temperature for domestic applications. Due to the integration into the shallow subsurface, potential interactions with ground water need to be considered; (b) TES operating at high temperature for solar thermal power plants.

In comparison with fluid storage media, the alternative use of solids, such as concrete, rocks, and ceramics as the thermal energy storage media can significantly reduce the costs of TES system, at a moderate expense of the energy storage capacity (cf. [25–33]). Intensive research and development of solid storage media have been conducted to optimise the performance of specific TES systems, such as increasing the heat capacity, shortening the charging/discharging time, and strengthening the thermal and mechanical stability of the storage media

at high temperature. A comprehensive investigation on the construction of a concrete thermal storage system used in parabolic trough solar thermal power plants has been reported by [27,34] with a particular focus on the long-term storage performance. Comparing to fluid storage media (mineral/synthetic oils, molten salts, etc.), a considerable cost reduction was achieved by using an appropriate high-temperature concrete storage material ([34,35]).

For the performance characterisation of the solid storage materials,

particularly concrete, many experimental studies have been conducted. For example, Laing et al. [36] tested the long-term behaviour of two distinct storage materials (a castable ceramic and a high-temperature concrete) developed by [37]. John et al. [38] developed an economical high-temperature concrete mixture with a temperature resistance of up to 600 °C. The development of such concrete mixtures is aimed at reducing the cost of the storage medium in order to make it more competitive compared to traditional power generation. Ozger et al. [39] produced a nylon fibre-reinforced concrete to enhance both the thermal and the mechanical performance as thermal storage material in TES systems. Particularly, the fibres can not only enhance the mechanical capability of the concrete to bear the strains in high temperature condition, preventing the formation of cracks, and also restrain the growth of cracks by lying on their propagation paths. The thermal properties and stability of such concrete mixtures were investigated in a range of temperature levels up to 450 °C. Skinner et al. [30] tested an ultrahigh-performance concrete incorporated into a TES system capable of operating at temperatures of up to 500 °C. They observed significant thermally induced cracking in the concrete as a consequence of the mismatched thermal expansion between the concrete and the heat exchanger (see also [23,24]). Alonso et al. [40] designed a calcium aluminate cement-based thermal storage material and tested its long-term stability under thermal cycles at high temperatures up to 550 °C. The degradation of mechanical strength of such cementitious composite were detected during the heating cycle testing.

Several of the above studies have shown that for TES systems composed of heat exchangers embedded within a solid storage material. The most significant potential for thermal cracking arises from the incompatible thermal deformation of the solid storage material and the heat exchanger from a macroscopic perspective. Fractures in solid storage media can have a dominating impact on the success of TES applications. On the one hand, they can degrade the charging/discharging efficiency by lowering the effective thermal conductivity ([30,41]). Particularly, Vejmelková et al. [41] investigated the influence of cracks to the moisture and heat transport in high performance concrete. The thermal conductivity exhibited an up to 40% loss in the cracked concrete. On the other hand, the long-term mechanical stability of a TES module may be challenged due to these unexpected fractures. On top of the mismatch of the thermal expansivity of the solid storage material and the heat exchanger, a similar mismatch exists between the cement-based matrix and the aggregates as well as between mineralogically different constituents in general (cf. [42–45,40,46]). These microstructural incompatibilities can lead to micro-cracking manifesting itself as distributed damage causing the degradation of mechanical (decreased stiffness and strength), thermal (decreased heat conductivity) and hydraulic (increased permeability) properties.

Exposed to cyclic temperature loads, thermal ratcheting effects can severely destroy solid storage media over time [38]. In this contribution, we focus on macroscopic effects around the heat exchangers where the transfer of the heat between the storage medium and the heat transfer loop occurs.

Recently, the thermo-hydro-mechanical behaviour of a water-saturated cement-based SHS for domestic low-temperature applications has been investigated by [23]. Critical tensile stresses within the cement-based storage material were observed during heating. These critical stresses can cause damage and subsequently fracture which may be associated with a thermal performance loss or the partial loss of long-term mechanical stability of the structures composed of the storage medium. To assist the engineering of an optimal design of TES systems from a thermo-mechanical perspective, an analytical approach was proposed by [24] to estimate the effects of the dominant physical and geometrical quantities on the critical tensile stresses observed in configurations composed of tubular heat exchangers embedded within the solid storage material.

Neither of the previous studies [23,24] was able to quantify: (i) whether damage remains local or progresses to structurally relevant sizes and (ii) to what degree thermal performance characteristics are affected once fractures or damage are present. From a wider perspective, it remains to be shown how cracks in solid storage media affect thermal power or capacity depending on the fluid medium (gas or liquid) which is going to fill the cracks.

Due to the limitation of laboratory experiments and field tests in terms of time, expenses, equipment, and measurable quantities, challenges arise as to the experimental quantification of the entire thermal cracking process within a solid storage material in a TES module under elevated temperature for a range of system configurations. This is particularly true since the failure is expected to occur in the bulk of large storage bodies and its detection would require sophisticated imaging or acoustic methods or post-mortem analyses.

It is therefore the aim of this contribution to propose a numerical approach to perform an initial estimate of both the extent of fracturing as well as its impact on thermal fields. Specifically, potential propagation patterns of cracks within prescribed concrete storage materials during heating processes at different temperatures are identified. The resulting changes in thermal properties relevant to the performance of the SHS are presented as well.

Fracture mechanical simulations require sophisticated numerical tools due to the development of discontinuities along paths not known a priori. Phase-field modelling was chosen as a numerical approach to fracture mechanics due to a number of attractive features. The principal highlight of this approach is that it smears the discontinuous crack by introducing a phase-indicator variable that smoothly transitions

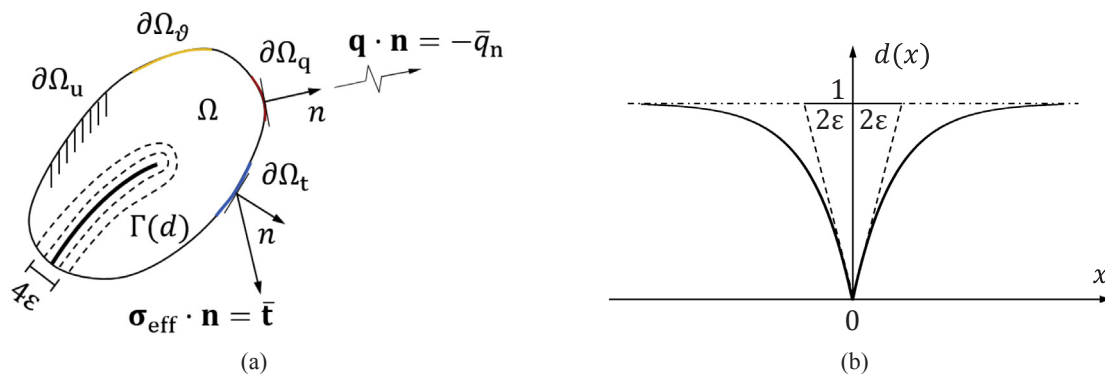


Fig. 2. (a) Elastic body with embedded diffusive crack. Here, we let $\Omega \subset \mathbb{R}^D$, $D \in [2, 3]$ be a reference configuration of a material body and $\partial\Omega \subset \mathbb{R}^{D-1}$ its external boundary with $\partial\Omega_u$, $\partial\Omega_s$ and $\partial\Omega_t$, $\partial\Omega_q$ the Dirichlet and Neumann boundaries for the mechanical and thermal fields, respectively, such that $\partial\Omega_u \cup \partial\Omega_t = \partial\Omega$ and $\partial\Omega_s \cup \partial\Omega_q = \partial\Omega$, with $\partial\Omega_u \cap \partial\Omega_t = \emptyset$ and $\partial\Omega_s \cap \partial\Omega_q = \emptyset$. (b) Schematic of the diffusive crack's exponential profile in 1D, characterised by a length-scale parameter 2ϵ .

between the undamaged material phase and the crack domain, so that the crack can be described from a continuous configurational perspective. Several phase-field implementations for brittle fracture based on variational principles were presented by [47–49] and others. The development of a fully coupled phase-field model for brittle fracture of solids subject to thermo-mechanical loading used in this study was presented in [50] based on similar work by [51].

Two analyses associated with a low-temperature TES based on water-saturated cement and a representative high-temperature TES in concrete are conducted, respectively. The fracture patterns are considered an indicator for the thermo-mechanical integrity of the SHS. The consequences of the presence of open fractures on the heat transfer behaviour are subsequently quantified. The demonstrated numerical analyses can assist the design optimisation for a designated TES system composed of a brittle solid storage material with embedded tubular heat exchangers from a thermo-mechanical perspective. Engineers might use this numerical approach to determine both designs and operation modes (e.g., peak temperatures) of a projected TES system based on the estimated mechanical stability and thermodynamic requirements. The approach can also be used to compare it with simpler methods of analysis designed for use in practice.

The present article is organised as follows. In Section 2, we briefly introduce the basic concept of the phase-field approach that is applied for our study. Particular attention is placed on the coupling of damage to heat transport. The model is tested on simple examples in Section 3. In Section 4, comprehensive analyses for the thermal fracture processes in the two different TES systems are performed. A further discussion and main conclusions of this paper are stated in Sections 5 and 6, respectively.

2. Model formulation for brittle fracture in thermo-mechanically loaded materials

2.1. The concept of a smeared crack

Instead of modelling a sharp crack interface, a continuously varying phase-field variable or order parameter d is introduced which is constrained between 0 (fully damaged) and 1 (intact material), see Fig. 2.

In such a continuous setting, the regularised crack surface functional can be written as a volume integral using the crack-surface density γ as (cf. [47–49,52])

$$\Gamma_\epsilon(d) = \int_\Omega \gamma dV = \int_\Omega \left[\frac{1}{4\epsilon}(1-d)^2 + \epsilon \text{grad } d \cdot \text{grad } d \right] dV \quad (1)$$

where $\Gamma \subset \mathcal{R}^{D-1}$ is the crack surface regularised by means of a length-scale parameter ϵ , hence Γ_ϵ . The formulation on the right-hand side of Eq. (1) implies an exponential characteristic of the transition between damaged and intact material as depicted in Fig. 2b for a one-dimensional setting.

It is worth noting that in addressing crack nucleation problems in the transition regime between strength and toughness-controlled phenomena, such a length-scale parameter must be carefully determined because of its physical association with the characteristic length (material's internal length) linked to the material's tensile strength defined in other gradient damage models (cf. [53–55]).

2.2. A thermodynamic approach of deriving the constitutive equations for thermoelasticity

The governing equations of phase-field models of fracture can be derived from various considerations including variational settings, rational thermodynamics, geometrical arguments, and configurational mechanics, respectively, cf. [49,56–58]. Under certain assumptions, all the three approaches lead to identical thermodynamically consistent results but highlight different conceptual perspectives. In this section, we combine the purely mechanical phase-field modelling of cracking

process with conductive heat transport (Fig. 2)a, and derive the constitutive equations from a thermodynamic perspective.

Based on the first and second laws of thermodynamics, in the framework of linear thermoelasticity for small deformations, the Clausius-Duhem inequality is formulated as (cf. [51])

$$\left(\sigma - \varrho \frac{\partial \bar{\psi}}{\partial \epsilon} \right) : \dot{\epsilon} - \varrho \left[\frac{\partial \bar{\psi}}{\partial d} - \text{div} \left(\frac{\partial \bar{\psi}}{\partial \text{grad } d} \right) \right] \dot{d} - \varrho \text{div} \left(\frac{\partial \bar{\psi}}{\partial \text{grad } d} \dot{d} \right) - \varrho \left(\eta + \frac{\partial \bar{\psi}}{\partial \vartheta} \right) \dot{\vartheta} - \varrho \frac{\partial \bar{\psi}}{\partial \text{grad } \vartheta} \cdot \text{grad } \dot{\vartheta} - \frac{1}{\vartheta} \mathbf{q} \cdot \text{grad } \vartheta \geq 0 \quad (2)$$

based on the postulate of a specific Helmholtz free energy with the following dependence: $\bar{\psi}(\epsilon, d, \text{grad } d, \vartheta, \text{grad } \vartheta)$.

To fulfill the inequality, standard arguments lead to the constitutive equation of mechanical part

$$\sigma = \varrho \frac{\partial \bar{\psi}}{\partial \epsilon} \quad (3)$$

The equilibrium formulation of the phase-field equation (the choice of irreversibility treatment for this study will be highlighted later on) can be extracted as

$$\frac{\partial \bar{\psi}}{\partial d} - \text{div} \left(\frac{\partial \bar{\psi}}{\partial \text{grad } d} \right) = 0 \quad (4)$$

along with the Neumann-type boundary condition

$$\frac{\partial \bar{\psi}}{\partial \text{grad } d} \cdot \mathbf{n} = 0 \quad \text{on } \partial\Omega \quad (5)$$

The specific entropy follows as

$$\eta = - \frac{\partial \bar{\psi}}{\partial \vartheta} \quad (6)$$

and from

$$\frac{\partial \bar{\psi}}{\partial \text{grad } \vartheta} = 0 \quad (7)$$

we find the independence of $\bar{\psi}$ from the temperature gradient. The residual dissipation inequality

$$- \frac{1}{\vartheta} \mathbf{q} \cdot \text{grad } \vartheta \geq 0 \quad (8)$$

yields Fourier's law:

$$\mathbf{q} = -\kappa \text{grad } \vartheta \quad \text{with } \mathbf{a} \cdot \kappa \mathbf{a} \geq 0 \quad \forall \mathbf{a} \neq \mathbf{0} \quad (9)$$

Based on the first law of thermodynamics, the energy balance can be written in local form as

$$\varrho \vartheta \dot{\eta} + \text{div } \mathbf{q} - \varrho r = 0 \quad (10)$$

where r is the specific heat source and where thermo-elastic coupling effects have been neglected.

The isobaric specific heat capacity can be found from the condition

$$c_p = -\vartheta \frac{\partial^2 \bar{\psi}}{\partial \vartheta^2} \quad (11)$$

Thus combining Eqs. (6) and (11), Eq. (10) can be expressed in a source-free form as the familiar heat conduction equation

$$(\varrho c_p)_{\text{eff}} \frac{\partial \vartheta}{\partial t} - \text{div} (\kappa_{\text{eff}} \text{grad } \vartheta) = 0 \quad (12)$$

with a Neumann-type boundary condition

$$- \mathbf{q} \cdot \mathbf{n} = \bar{q}_n \quad \text{on } \partial\Omega_q \quad (13)$$

where the use of the effective volumetric heat capacity $(\varrho c_p)_{\text{eff}}$ and the effective thermal conductivity tensor κ_{eff} indicates that in the sequel these quantities will be properties of different phase contributions. Aside from that, no provisions are made in this study to account for the

presence of kinematically independent fluid phases, cf. [23].

2.3. Degradation of elastic energy and thermal properties

The thermally induced strains and thermo-mechanical coupling are incorporated into the framework within a kinematically linear setting. The total strain is therefore additively composed of the elastic and thermal part

$$\epsilon = \epsilon_{el} + \epsilon_{th} \tag{14}$$

with

$$\epsilon_{th} = \alpha_T (\vartheta - \vartheta_0) \tag{15}$$

where α_T stands for the linear thermal expansion tensor.

We formulate the Helmholtz free energy density of a thermoelastic solid as the combination of mechanical, thermal and regularised surface-energy contributions:

$$\psi(\epsilon, \vartheta) = \psi_m(\epsilon_{el}) + \psi_{th}(\vartheta) + \psi_{surf}(\gamma) \tag{16}$$

It is a reasonable assumption in many situations that the compression perpendicular to a crack does not cause crack propagation and that the strain energy is not degraded in that case so that crack-face interpenetration is prevented. Several approaches exist for this so-called tension-compression split (cf. [49,57–62]). We choose to decompose the intact strain energy density ψ_{m0} into volumetric and deviatoric contributions following [59,60]:

$$\psi_{m0}^+(\epsilon_{el}) = \frac{1}{2}K(\text{tr}(\epsilon_{el}))_+^2 + \mu(\epsilon_{el})^D : (\epsilon_{el})^D \tag{17}$$

$$\psi_{m0}^-(\epsilon_{el}) = \frac{1}{2}K(\text{tr}(\epsilon_{el}))_-^2 \tag{18}$$

where μ is the second Lamé constant/shear modulus, K is the bulk modulus, $\langle \cdot \rangle_{\pm} := (\pm|\cdot|)/2$ the Macauley brackets and $\epsilon^D := \epsilon - 1/3\text{tr}(\epsilon)\mathbf{I}$ a deviatoric strain tensor.

Using standard formulations for the thermal part (cf. [63]), an approximation of the Helmholtz free energy density of a fractured body in thermoelasticity can be formulated as

$$\begin{aligned} \varrho\bar{\psi}(\epsilon, d, \text{grad } d, \vartheta) &= (d^2 + k)\psi_{m0}^+(\epsilon, \vartheta) + \psi_{m0}^-(\epsilon, \vartheta) \\ &+ G_c \left[\frac{1}{4\epsilon} (1 - d)^2 + \epsilon \text{grad } d \cdot \text{grad } d \right] \\ &- (\varrho c_p)_{\text{eff}} \left(\vartheta \ln \frac{\vartheta}{\vartheta_0} - \vartheta + \vartheta_0 \right) \end{aligned} \tag{19}$$

where k represents a residual stiffness used in numerical calculations to ensure a residual elastic energy density in the fully damaged state. The parameter G_c stands for the critical Griffith-type energy release rate such that $\psi_{surf} = G_c \gamma$.

Substituting Eq. (19) into Eq. (3), one obtains the specific formulation of the stresses

$$\sigma = (d^2 + k)\sigma_0^+ + \sigma_0^- \tag{20}$$

Substituting Eq. (19) into Eq. (4), one obtains the specific formulation of the phase-field equation

$$- 2d\psi_{m0}^+(\epsilon, \vartheta) + G_c \left[\frac{1}{2\epsilon} (1 - d) + 2\epsilon \text{div}(\text{grad } d) \right] = 0 \tag{21}$$

This equation represents an equilibrium formulation as indicated earlier. To enforce irreversibility of the fracturing process (no healing),

we employ a Dirichlet constraint to the phase-field d once a crack has developed (cf. [47])

$$d := \{d = 0 \mid d \leq 0.05\} \tag{22}$$

The effective thermal conductivity κ_{eff} , depends on the presence of fractures in the material body, i.e. the medium contained within the cracked volume will affect the thermal performance of the material body, and in general, the thermal conductivity of the fracture body will degrade. To take into account the degradation of the thermal conductivity within the cracked domain, the following dependence has been chosen (cf. [51,56]):

$$\mathbf{q} = -\{H[\text{tr}(\epsilon_{el})][d^2 - 1)\kappa_s + (1 - d)^2\kappa_d + \kappa_s\} \text{grad } \vartheta \tag{23}$$

where κ_s the conductivity of the undamaged storage medium and κ_d the (residual) thermal conductivity of the crack-phase which depends on the medium filling the newly created voids (e.g. air, water, thermal oil, etc.). The presence of the Heaviside term $H[\text{tr}(\epsilon_{el})]$ allows for a simple treatment of crack closure: In the case of positive volumetric elastic strain the crack is considered open and the thermal properties degrade with the progression of damage. Once the volumetric elastic strain turns negative, we consider the crack faces in contact and the conductivity of the undamaged material is restored. At this stage, similar effects related to the volumetric heat capacity have been neglected.

2.4. Numerical implementation

The numerical implementation of the continuum-mechanical phase-field model is realised within the scientific open-source finite element platform OpenGeoSys [50,58,64], in an incremental-iterative Newton–Raphson scheme in conjunction with the implicit backward-Euler method for time discretisation. In particular, the alternative minimisation scheme embedded in a staggered algorithm has been adopted following [65]. The source code is freely available at <https://github.com/ufz/ogs/tree/master/ProcessLib/ThermoMechanicalPhaseField> upon publication of the manuscript. For a description of an alternative monolithic numerical realisation, as well as model verification, the interested reader can refer to [50,58]. Selected further aspects will be presented in the next section.

3. Model verification

To verify the numerical realisation of the non-isothermal fracture-mechanical model, two classical yet simple tests are performed to demonstrate the modelling capability from purely mechanical and thermo-mechanical perspectives, respectively. The main material and geometrical parameters used in the following tests are listed in Tables 1 and 2. A direct solver (SparseLU) is always used for solving the linear system. Newton-Raphson iterations are performed to resolve non-linearities with an absolute tolerance of 10^{-10} associated with the phase-field for both tests, and a convergence tolerance of 10^{-10} related to the phase-field process in coupling iterations.

3.1. Single-edge-notched isothermal tension test

A classical single-edge-notched tension test in association with a pre-existing straight crack ([49,53,56,57,60,65]) is performed for testing the capability of the implemented numerical algorithm in tracing the expected single straight propagation process driven by

Table 1
Parameters for numerical examples: part I – material properties.

Models	Young's modulus E /GPa	Poisson's ratio ν	Fracture toughness G_c /(J mm ⁻²)	Thermal expansion coefficient α_T /(K ⁻¹ × 10 ⁻⁶)
Single-edge-notched	210	0.3	2.7	–
Slab	340	0.22	0.04247	8

Table 2
Parameters for numerical examples: part II – geometric sizes.

Models	Length L /mm	Width W /mm	Height H /mm
Single-edge-notched Slab	1 2	– 0.01	1 0.4

appropriately controlled Dirichlet boundary conditions.

A straight horizontal notch is placed at the mid-height of the left edge with a length of 0.5 mm extending to the centre of the specimen (see, Fig. 3) by defining a corresponding initial condition for the phase-field variable. A series of displacement increments of $\Delta u = 0.01 \mu\text{m}$ is applied to the upper edge of the model to drive the propagation of the pre-existing horizontal crack (Mode I crack) until a maximum displacement of approximate $6 \mu\text{m}$ is reached. The mesh is refined a priori with a minimum mesh size h_{single} of approximately $1 \mu\text{m}$ in the region through which the crack is expected to propagate, and a total of 18,440 linear triangular plane-strain elements are used.

The OGS input files for this test can be found at <https://github.com/ufz/ogs/tree/master/Tests/Data/ThermoMechanicalPhaseField>.

The propagation path of the pre-existing crack driven by the tensile loading through the material is illustrated in Fig. 4a, while Fig. 4b depicts the corresponding load-displacement curve for the upper edge. Both the crack propagation and the load-displacement patterns are consistent with the literature, cf. [49,57].

3.2. Thermal shock

To test the model under non-isothermal conditions, the following example demonstrates the nucleation and propagation of multiple cracks induced by a thermal shock, cf. [51,53,66]. The specimen configuration (Fig. 5) is motivated by the experimental study on sequential crack patterns forming in brittle solids subjected to thermal shocks by e.g. water-quenching [67–69]. In experimental investigations, the brittle slab is first heated up to a uniform preset temperature, and then placed in contact with a cold bath so that one edge of the slab is rapidly cooled down, forming a temperature gradient through the slab in the direction perpendicular to the cold bath.

A discretisation of 8,000 hexahedral elements with an uniform element size h_{slab} of $10 \mu\text{m}$ is applied (dimensions see Table 2). The bottom surface of the specimen is fixed in all directions and plane-stress conditions are imposed. A temperature drop of $\Delta T = 800 \text{K}$ is imposed to ensure stresses induced by this temperature field can be high enough to initiate the cracking process and drive the propagation of cracks, cf. [53,68].

According to Bourdin and coworkers [55,66], the geometric dimension of the domain L , the material’s internal length l_{ch} , and the Griffith length l_G govern the material’s response to the external loading fields.

The internal length characterises the link between the material’s fracture toughness and strength

$$l_{\text{ch}} = \frac{G_c E}{\sigma_t^2} = \frac{K_{\text{Ic}}^2}{\sigma_t^2} \tag{24}$$

while the Griffith length is defined as

$$l_G = \frac{G_c}{E(\alpha_T \Delta T)^2} \tag{25}$$

and expresses a ratio between the fracture energy and a strain energy measure due to constrained thermal expansion. A large enough domain ($L \gg l_{\text{ch}}$) must be applied to obtain a localised solution so that inhomogeneous cracking processes can be triggered.

The use of Helmholtz free energy functional in the formulation of Eq. (19) requires a specific adjustment to the internal length (cf. [55,66]), thus

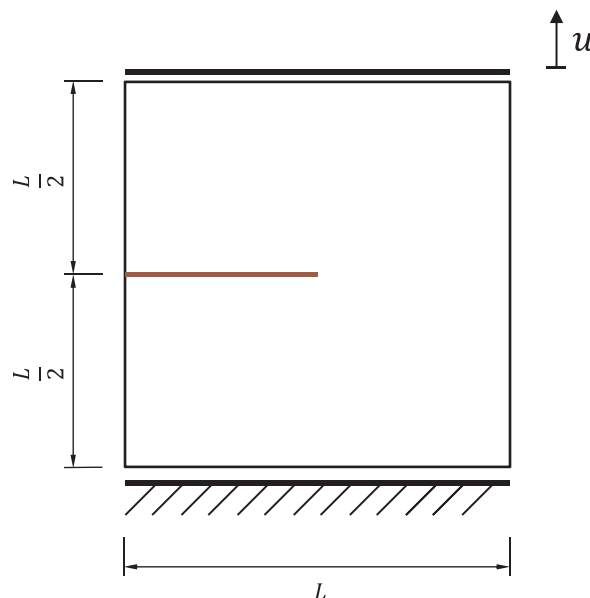


Fig. 3. Single-edge-notched model.

$$l: = \frac{27G_c E}{256\sigma_t^2} \tag{26}$$

The crack characteristics in the specimen during the cooling process are demonstrated in Fig. 6. Crack initiation emerges in parallel arrays along the surface exposed to the temperature drop because of the induced thermal contraction and associated high tensile transversal stress in the vicinity of the surface. Cracks then propagate through the specimen perpendicular to the exposed surface. It is worth noting that the density of cracks nucleating along the specimen is governed by the intensity of the imposed temperature drop, i.e. the Griffith length. For the case of $l_G \ll l$, i.e. a severe thermal shock, the ideal initial crack spacing λ_c should be proportional to $\sqrt{l_G l}$ ($\lambda_c \propto \sqrt{l_G l}$, see Fig. 7, cf. [53,66]).

The OGS input files for this case can be found at <https://github.com/ufz/ogs/tree/master/Tests/Data/ThermoMechanicalPhaseField>.

In addition, further tests for model verification, as well as consistency checks of the numerical implementation are deposited in the repository.

4. Thermal cracking processes within the concrete storage material

In this section, we investigate two solid TES systems based on our previous studies of a low-temperature module [23,24] and a well-studied high-temperature module [27,34], respectively, to systematically explore how fracturing may occur within specific SHS and how it affects the thermal performance of the system. The two systems differ in thermal conditions (temperature, power), material properties, pore/crack-filling fluid, and heat exchanger configurations.

4.1. Low-temperature SHS

The IGLU project² aims at developing a cement-based SHS with embedded heat exchangers through which a heat transfer medium,

²“Untersuchung, Modellierung und Bewertung eines intelligenten geothermischen Langzeitwärmespeichers mit umweltneutralem Verhalten”, or “Analysis, Modelling and assessment of an intelligent and environmentally neutral geothermal long-term heat storage system.” is a project funded by the German Federal Ministry of Economy and Energy (BMWi) and coordinated by SCHEER Heizsysteme & Produktionstechnik GmbH, see Acknowledgements.

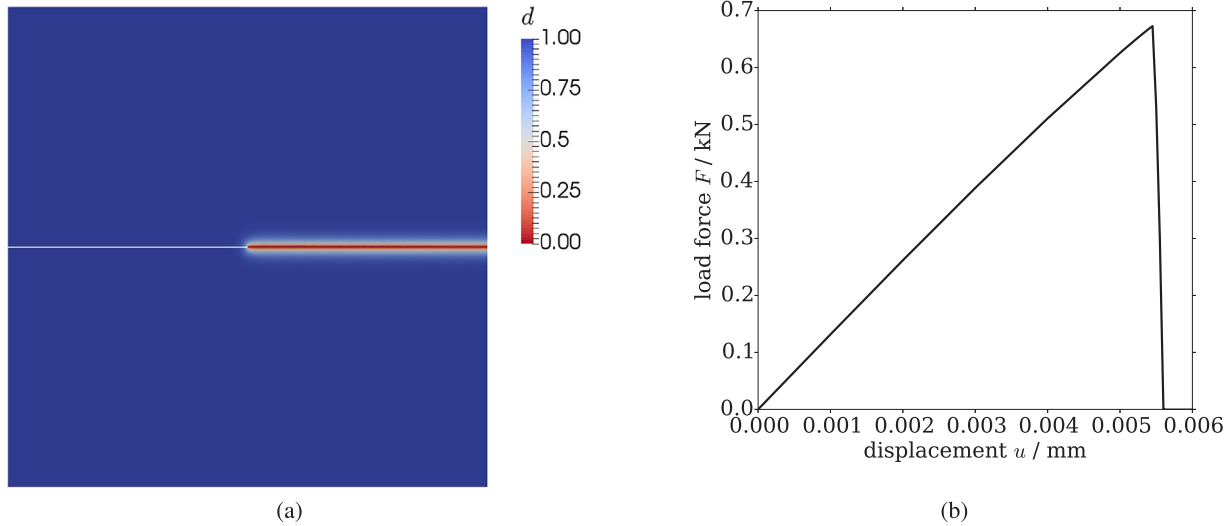


Fig. 4. Single-edge-notched tension test: (a) crack propagation pattern; (b) load-displacement curve.

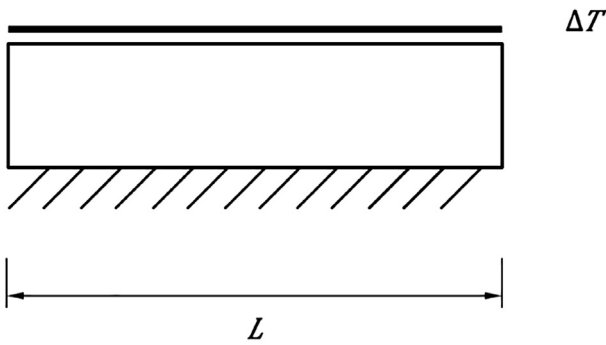


Fig. 5. Slab under a thermal shock.

currently water, is flowing. This solution is considered an effective alternative to currently available storage systems for limiting vessel costs, process complexity and space requirements combined with easy handling and the general advantages of SHS, see Fig. 8.

Fig. 9 illustrates the configuration of a designated single SHS used in the IGLU project. The heat exchanger material is selected to be an aluminium-polyethylene composite, and the heat transfer fluid circulating through the pipes will be heated up to 90 °C during the charging phase. The highly porous cement-based storage material is fully saturated by water. Thus, in the event of crack formation, the open fractures are assumed to fill with water. The crack-phase heat conductivity κ_d in Eq. (23) is thus set to the values for liquid water.

To investigate how far potential cracks spread and whether cracks

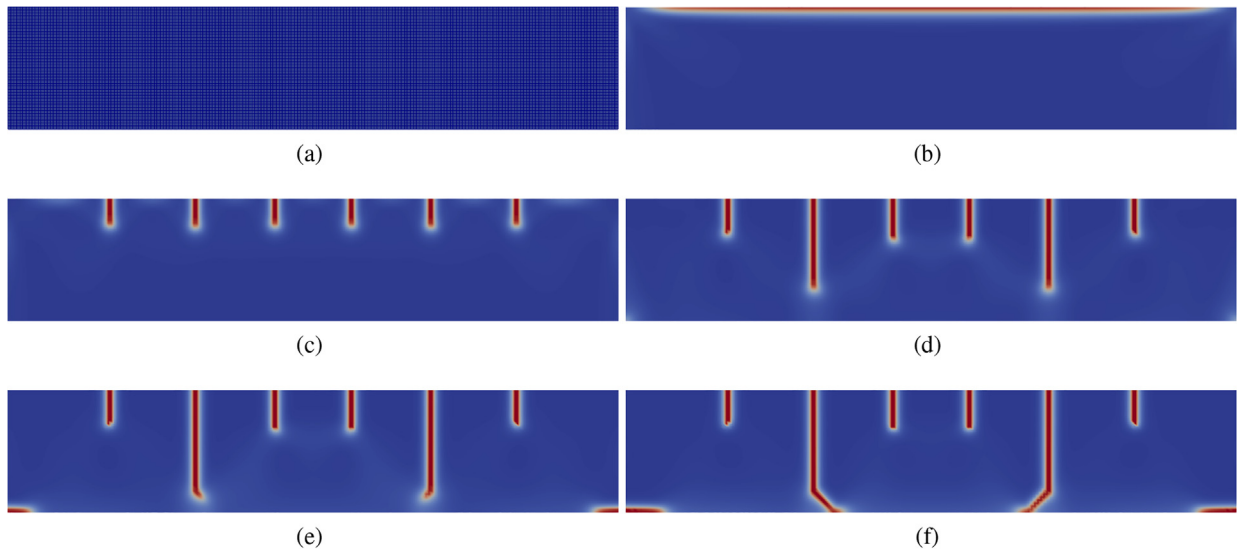


Fig. 6. Evolving patterns of cracks nucleation and propagation in the specimen (red region represents crack bands; $h_{slab} < l$; $\Delta T = 800$ K; $l = 0.013$ mm; $l_G = 0.234l$).



Fig. 7. Evolving patterns of cracks nucleation in the specimen ($\Delta T = 1000$ K; $l_G = 0.15l$, $\sqrt{l_G l} = 0.005$ mm, $\lambda_c \approx 0.06$ mm).

initiated around the heat exchangers connect to a full-length crack throughout the entire storage body, a sample model extracted from a single SHS is built, see Fig. 10.

Similar to previous analyses of the test rig [23], an axisymmetric FEM model is set up to analyse the thermal and mechanical behaviour of the SHS module. A temperature field applied on the inside wall of the heat exchanger is increased linearly from 10 °C to a maximum of 90 °C

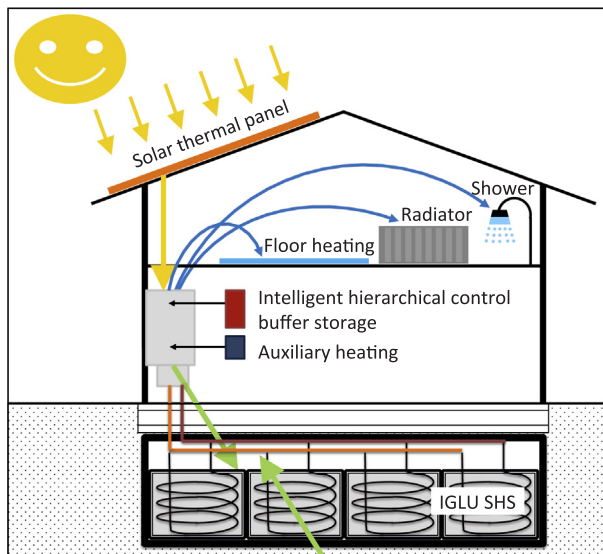


Fig. 8. Schematic of the system configuration investigated as part of the IGLU project.

within 10 min and subsequently held constant over the next two hours.

Because the simulations in the present study serve the purpose of detecting the crack evolution without a priori knowledge of the exact crack path, all following tests are performed with a prescribed uniform element size in the entire or selected domain to avoid prescribing a discretisation-based directional energetic bias for fracture propagation.

In this present case, the remote temperature gradient from the centre of the SHS module has no contribution to the crack formation around the heat exchangers within the prescribed computational scenario. Hence, the mesh of the model contained 34,020 linear triangular elements with a uniformly refined mesh size of 1.5 mm in a selected domain surrounding the heat exchangers covering approximately one third of the volume of the computational model.

Note that to properly capture the cracking behaviour inside the material body, the element size employed in all following tests is smaller than the internal lengths characterising the specific storage materials (cf. [55,66]).

Fig. 11 shows the fracture pattern of the sample module due to elevated temperatures. When the temperature reaches around 41 °C, cracks already initiate within the material body due to its very low fracture toughness, see Table 4. Damage within the storage material produced by the incompatibility of thermal strains and the resulting tensile stresses is observed around the concrete phase boundaries near the left surface of heat exchangers. Cracks in the matrix propagate along the material interfaces and approach each other, eventually forming a full-length connected crack around the inner field of the

model during the demonstrated heating scenario. In consequence, the storage body is separated into an annulus and a core, and thus both the mechanical and thermal properties of such SHS will degrade. Note that the radial displacements of the heat exchangers causing the tensile stresses in the storage material are very small and that this result is strongly dependent on whether the initial bonding between pipes and cement is perfect, as assumed here, or there exists an initial gap. Such an initial gap can drastically reduce the stresses in the cement and hence the tendency for failure but is difficult to quantify as it depends on the production of the storage module as well as shrinkage of the cement during curing.

To illustrate the effect of the fractures on the thermal properties of the heat storage, we simulate another heating cycle, now using the cracked model. Fig. 12 highlights the thermal performance differences between the intact and fractured cases. A profile of the temperature difference of the two cases corresponding to the highest performance loss is depicted in Fig. 12b. It can be seen that the highest temperature discrepancy of the two models occurs around the damaged zones and amounts to ± 6 K.

In this TES module, to increase the energy density of the SHS, the storage material is in fully water-saturated condition, thus the residual medium within the damaged area is assumed to be water. Because of this assumption, the temperature perturbation remains low. Particularly, although the original heat conduction process is impaired due to the formation of a crack within the storage body, the highest loss of heat flow is only 7.7% ($\Delta\dot{Q} = (\dot{Q}_{\text{intact}} - \dot{Q}_{\text{damaged}})/\dot{Q}_{\text{intact}}$).

4.2. High-temperature SHS for TES systems

The second example deals with a solid storage configuration (Fig. 13) designed for high power and temperature tolerance to serve in power plants, and usually synthetic oil [36] or molten nitrate salt [30] are considered as the heat transfer medium. High-performance concrete or ceramics are typically employed as economical storage materials. However, significant cracking was found in experiments of a unit block concrete TES at high temperatures reported in [30]. The incompatible thermal deformation leads to severe damage in the concrete storage media when the charging temperature is sufficiently high. In consequence, the thermal and mechanical stability of this type of solid TES system is challenged by the elevated operational temperature condition. The demonstrated high-temperature SHS module we investigate here is based on [27,34,37] and depicted in Fig. 13. Note that in practical application, heat exchanger bundles are incorporated in such SHS module, and the number of the used pipes per cross-sectional area depends on the design power of a designated TES system. The heat exchanger material considered here is 316 stainless steel, and the pipes are heated up to 390 °C during the charging phase. The residual medium in the fracture zones is assumed to be air in contrast to the previous example, resulting in a much lower value for κ_d . The tube pitch between two adjacent pipes is set to 80 mm.



Fig. 9. Configuration of the SHS used in IGLU TES: (a) a heat exchanger and a cylindrical mold prepared for the SHS; (b) a single configured testing module. Images with kind permission by Prof. Frank Wuttke, Chair of Geomechanics & Geotechnics, Kiel University, www.geotechnics.ifg.uni-kiel.de.

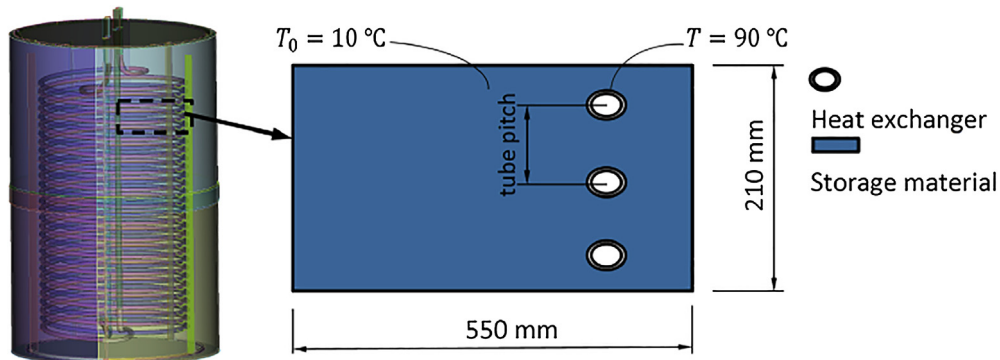


Fig. 10. A testing module. The axisymmetric model (right) is extracted from the single SHS module (left), and contains three vertically lined heat exchanger pipes. The length of this model equals to the radius of the single SHS module.

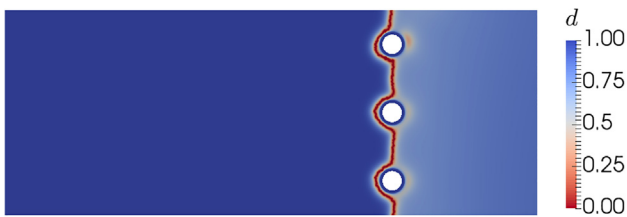


Fig. 11. Cracking evolution in the storage body with axisymmetry.

Two reference modules taking into account two typical locations (model a: centro-symmetrically constrained sub-domain, Fig. 13(a); model b: bottom constrained boundary-adjacent sub-domain, Fig. 13(b)) of the concrete-pipe units are performed in this case. The geometry and materials of the solid storage medium and the heat exchanger illustrated in Laing and coworkers’ investigation [27,34,35] are used, see Tables 3 and 4, and Fig. 13. The model covers four heat exchanger pipes with arrangement in a 2×2 configuration, i.e., the height and the length of the model both equal two times the tube pitch. In this test, a temperature field applied on the inside wall of the heat exchanger is increased linearly from 10 °C to a maximum of 390 °C within 5 min, which is then held constant over the next two hours. 30,028 linear triangular plane-strain elements with a uniform mesh size of 1.5 mm are employed in model a, and model b uses the same mesh type and contains 29,756 elements with a homogeneous mesh size of 1.5 mm.

It is worth noting that because some material’s mechanical properties (fracture toughness, Young’s modulus, and Poisson’s ratio) that are required in our study are not available for the studied SHS module.

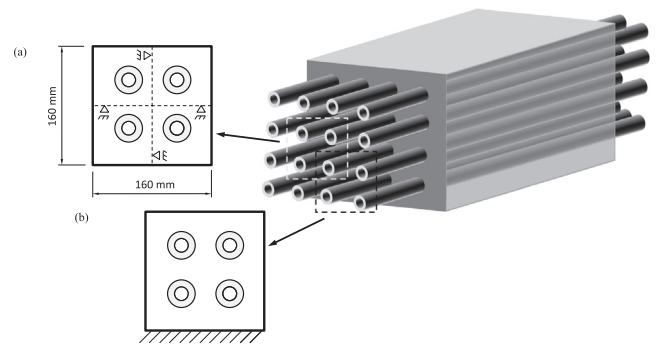


Fig. 13. Schematic of standard SHS module subset with tabular heat exchanger pipes and two reference models applied for representing the potential path of crack evolution.

We thus select an alternative concrete from the literature [70] based on the design temperature, the characteristics of the concrete defined in Laing and coworkers’ field/in situ investigations which might differ in detail from the values of the material employed in their specific SHS configuration. Thus, the numerical values of the results should be considered as qualitative.

Figs. 14 and 16 show the fracture patterns in the two reference models due to elevated temperatures. Due to differences in the thermal expansion coefficients of the heat exchanger and the concrete storage material, tensile stresses are induced in the circumferential direction within the concrete, which are the forces that drive the initiation and propagation of cracks, and the initial cracks develop along the material

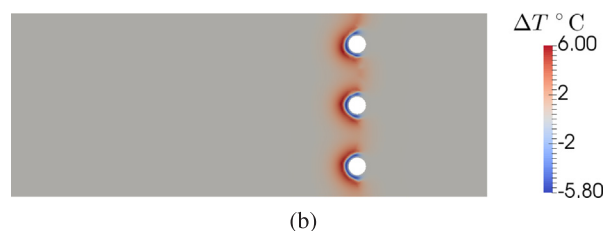
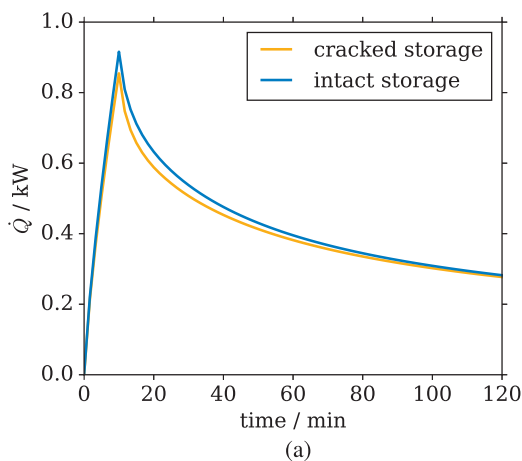


Fig. 12. Heating power and temperature performance over a charging process: (a) power profiles of the intact and cracked SHS body over a heating period; (b) temperature difference ($\Delta T = T_{\text{intact}} - T_{\text{damaged}}$) between the intact and cracked SHS body corresponding to the highest power difference.

Table 3
Material properties of heat exchangers and storage materials: part I – thermal properties.

Materials	Thermal conductivity κ_s ($\text{W m}^{-1} \text{K}^{-1}$)	Thermal expansion coefficient α_T ($\text{K}^{-1} \times 10^{-6}$)	Specific heat capacity c_p ($\text{J kg}^{-1} \text{K}^{-1}$)
Low-temperature IGLU TES			
Heat exchanger Alu-PE composite	0.4	30.0	1261
Storage material Füllbinder L	0.96	10.7	2083
High-temperature TES			
Heat exchanger 316 stainless steel	16.2	17.5	530
Storage material High-temperature concrete	1.65	9.9	950

Table 4
Material properties of heat exchangers and storage materials: part II – mechanical properties.

Materials	Young's modulus E GPa	Poisson's ratio ν	Fracture toughness G_c (J mm^{-2})
Low-temperature IGLU TES			
Heat exchanger Alu-PE composite	68.9	0.4	8
Storage material Füllbinder L	1.9	0.17	0.00067
High-temperature TES			
Heat exchanger 316 stainless steel	200	0.27	11
Storage material High-temperature concrete	33	0.22	0.3

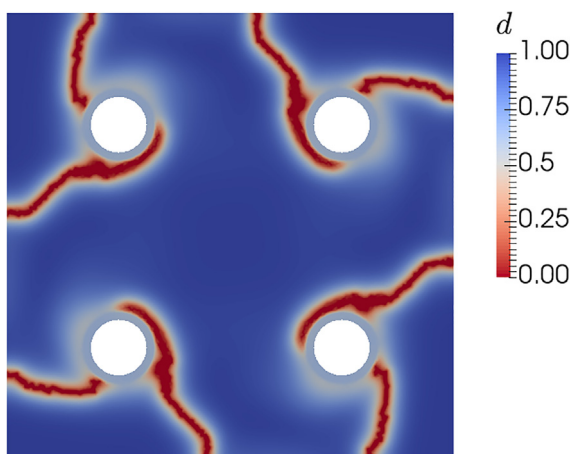


Fig. 14. Cracking profile over a charging process in model a.

interfaces between the two components in a circumferential way. Under the same geometrical setting, the nature of cracking highly depends on the stress gradient induced by the mismatched thermal expansion between the two components and the response from the matrix boundaries, as well as the assumptions of the external constraints (boundary conditions related to the location of the unit cell within a larger storage module). In model a, upon the heating process, localised radiating cracks are formed from the heat exchanger to the adjacent radiaries

of the matrix body.

Cracking processes around each single heat exchanger proceed independently, separating the near field of the heat exchanger from the storage body. In model b, cracks initiate along the interfaces between the two components and propagate towards the matrix body, finally approaching each other or the adjacent boundaries, indicating potential breakage of the storage body into separate parts. As before, the occurrence of these patterns is not only strongly dependent on material and boundary conditions, but also on contact conditions. Any gap present before heating starts would strongly decrease the propensity for cracking.

Figs. 15 and 17 underline the heating power discrepancies between the assumed intact and damaged storage modules during additional heating cycling when distinct damaged zones have been formed under the specific simulation scenarios.

In principle, the developed cracks form an air (residual medium) space between the remaining storage body of two sides, which behaves as a barrier to heat transfer because of its relatively low thermal conductivity, leading to high temperature gradients in the damaged regions. The differences in local temperatures compared between the two scenarios for a given time point peak at more than 200 °C.

Unlike the case of IGLU project in association with low heating loadings, in the case of solar thermal power plant with high power input, it causes significant fluctuations in heat flows over the heating cycle. During the first 20 min of charging, the heating power is significantly diminished.

5. Discussion

Previous studies have identified the critical regions in a concrete TES structure caused by incompatible thermal strains originating from temperature gradients or jumps in material properties as well as from the specific impact of the pore fluid [23]. These results were used for identifying optimal configurations to minimise induced critical stresses based on the dominant material properties and geometrical quantities that can affect the mechanical integrity of a solid TES structure [24].

Potential damage in those regions leading to a loss of thermal performance has been discussed in this paper from a thermo-mechanical perspective. A phase-field approach for addressing the fracturing processes themselves is applied here to a solid TES structure subject to thermo-mechanical loading. The implemented numerical framework has first demonstrated its capability to capture material and structural failure based on several classical benchmarks, as well as a qualitative reference to an experimental study conducted by [30].

The application of phase-field modelling in our present study and the results obtained have shown the principal capability of this numerical approach in analysing complex scenarios associated with multi-physical conditions. It can be helpful in interpreting and complementing field/laboratory testing, e.g. for planning a solid TES system. In turn, the results may imply that for system monitored during operation, potential local failure can be picked up from the observation of a permanent decline or fluctuation of the heat flow.

The present results should not be considered as quantitative. This is due to uncertain material parameters, uncertain contact conditions, as well as numerical uncertainties. However, the analyses clearly highlight a potential degradation mechanism of the thermal operational characteristics of a solid heat storage by thermo-mechanically initiated damage processes.

Some further aspects can be considered in the future: (i) full-scale three-dimensional models can offer more straightforward and accurate assessment of the performance of solid TES systems; (ii) shape variations of the heat exchangers should be taken into account which might influence crack nucleation due to the non-symmetric stress fields in the storage body; (iii) contact conditions should be investigated and measured, because they can highly change the development of critical stresses based on our previous study ([23]); (iv) simple practical design

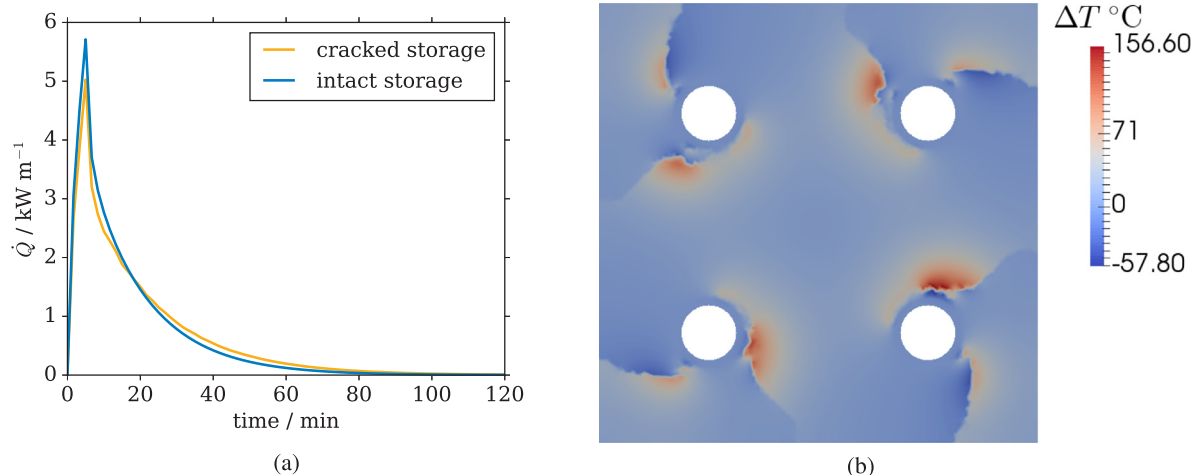


Fig. 15. Heating power and temperature performance over a charging process in model a: (a) power profiles of the intact and cracked SHS body over a heating period; (b) temperature difference ($\Delta T = T_{\text{intact}} - T_{\text{damaged}}$) between the intact and cracked SHS body corresponding to the highest power difference.

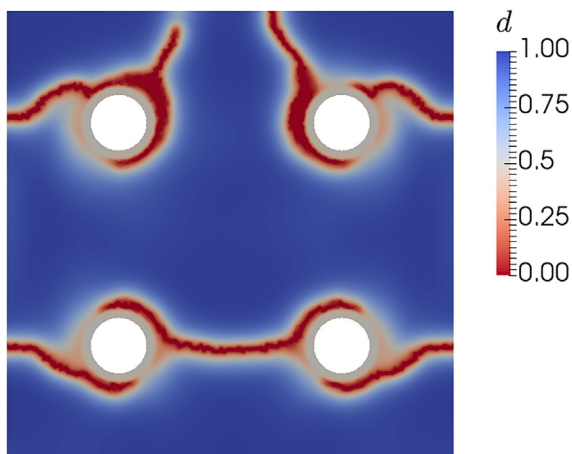


Fig. 16. Cracking profile over a charging process in model b.

guidelines not requiring such complex analyses should be derived and backed up by numerical simulations; (v) the effective heat conductivity model associated with damage requires improvement; the tension compression split for crack-face contact should consider the crack orientation, and radiation should be added as a heat transfer mechanism

especially in high-temperature cases; (vi) heat storage devices are cyclically loaded. Fatigue and thermal ratcheting effects, as well as material degradation due to microscopic damage effects associated with different mineralogical constituents of the storage material are to be expected. They likely present a dominant mechanism for the long-term integrity of the solid heat storage and have not been considered here.

6. Conclusions

Two representative solid SHS configurations with different materials and subjected to different thermal conditions were investigated. By quantifying the influences of the ensuing damage on temperature fields and thermal power into the SHS, it was shown that a mechanically driven thermal power loss is possible. The significance of this effect highly depends on the degree of fracturing and the difference of thermal conductivities between the intact storage material and the residual medium in the open fractures. For water-saturated low-temperature heat storage considered as part of the IGLU project, the expected heating power loss is small for the parameters applied here. For the high-temperature TES on the other hand, significant potential fluctuations in charging power were found, which are undesirable for a solar thermal project. Future work should specifically address both material degradation associated with microscopic effects and phenomena associated with cyclic loading.

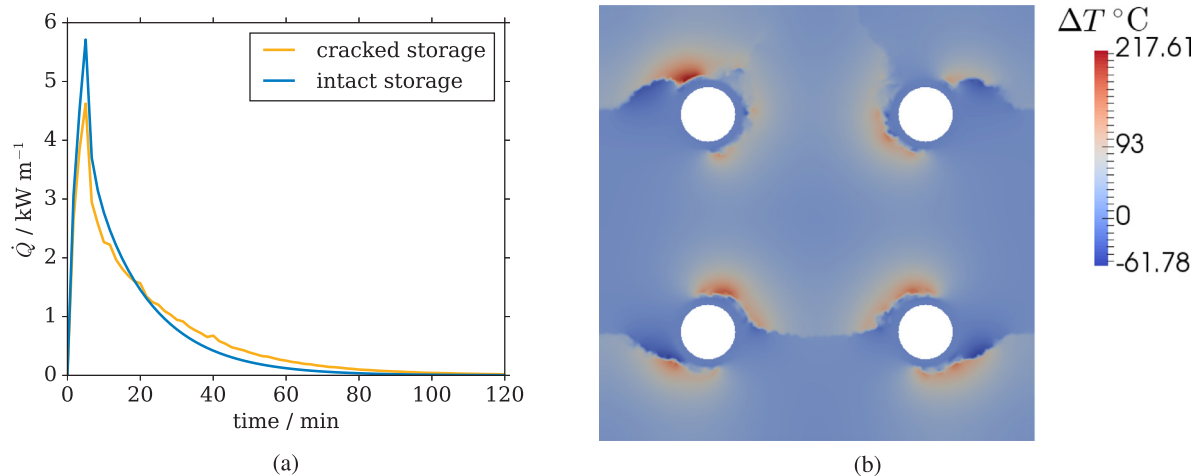


Fig. 17. Heating power and temperature performance over a charging process in model b: (a) power profiles of the intact and cracked SHS body over a heating period; (b) temperature difference ($\Delta T = T_{\text{intact}} - T_{\text{damaged}}$) between the intact and cracked SHS body corresponding to the highest power difference.

Acknowledgements

The authors would like to thank Wenqing Wang, Keita Yoshioka, and Dmitri Naumov for their support on the numerical implementation of the model into OpenGeoSys. The authors also thank Frank Wuttke and his colleagues from Kiel University for providing various photos of the test configurations, and for testing certain material properties of the storage material used in the IGLU project. Finally, we acknowledge Florian Wallburg for the support during the initial literature review on multi-physical phase-field models.

Funding was provided by the German Federal Ministry of Economic Affairs and Energy under Grant No. 0325547C (“Analysis, modelling and assessment of an intelligent and environmentally neutral geothermal long-term heat storage system”, project acronym IGLU) and is gratefully acknowledged.

References

- Gil Antoni, Medrano Marc, Martorell Ingrid, Lazaro Ana, Dolado Pablo, Zalba Belen, et al. State of the art on high temperature thermal energy storage for power generation. part 1—concepts, materials and modellization. *Renew Sust Energy Rev* 2010;14(1):31–55.
- Zhang HL, Baeyens Jan, Degreè J, Cacères G. Concentrated solar power plants: review and design methodology. *Renew Sust Energy Rev* 2013;22:466–81.
- Liu Ming, Tay NH Steven, Bell Stuart, Belusko Martin, Jacob Rhys, Will Geoffrey, et al. Review on concentrating solar power plants and new developments in high temperature thermal energy storage technologies. *Renew Sust Energy Rev* 2016;53:1411–32.
- Bijarniya Jay Prakash, Sudhakar K, Baredar Prashant. Concentrated solar power technology in india: a review. *Renew Sust Energy Rev* 2016;63:593–603.
- Soria Rafael, Lucena André FP, Tomaschek Jan, Fichter Tobias, Haasz Thomas, Szklo Alexandre, et al. Modelling concentrated solar power (csp) in the brazilian energy system: a soft-linked model coupling approach. *Energy* 2016;116:265–80.
- Zhang Huili, Baeyens Jan, Caceres Gustavo, Degreve Jan, Lv Yongqin. Thermal energy storage: recent developments and practical aspects. *Prog Energy Combust Sci* 2016;53:1–40.
- González-Portillo Luis F, Muñoz-Antón Javier, Martínez-Val José M. An analytical optimization of thermal energy storage for electricity cost reduction in solar thermal electric plants. *Appl Energy* 2017;185:531–46.
- Kuravi Sarada, Trahan Jamie, Yogi Goswami D, Rahman Muhammad M, Stefanakos Elias K. Thermal energy storage technologies and systems for concentrating solar power plants. *Prog Energy Combust Sci* 2013;39(4):285–319.
- Chacartegui R, Vigna Leo, Becerra JA, Verda V. Analysis of two heat storage integrations for an organic rankine cycle parabolic trough solar power plant. *Energy Convers Manage* 2016;125:353–67.
- Mao Qianjun. Recent developments in geometrical configurations of thermal energy storage for concentrating solar power plant. *Renew Sust Energy Rev* 2016;59:320–7.
- Iranzo Alfredo, Suárez Christian, Guerra José. Mixing enhancement in thermal energy storage molten salt tanks. *Energy Convers Manage* 2018;168:320–8.
- Mehrpooya Mehdi, Dadak Ali, et al. Investigation of a combined cycle power plant coupled with a parabolic trough solar field and high temperature energy storage system. *Energy Convers Manage* 2018;171:1662–74.
- Wang Xiaohe, Liu Qibin, Lei Jing, Han Wei, Jin Hongguang. Investigation of thermodynamic performances for two-stage recompression supercritical CO₂ brayton cycle with high temperature thermal energy storage system. *Energy Convers Manage* 2018;165:477–87.
- Salas D, Tapachès E, Mazet N, Aussel D. Economical optimization of thermochemical storage in concentrated solar power plants via pre-scenarios. *Energy Convers Manage* 2018;174:932–54.
- Dincer Ibrahim, Dost Sadik, Li Xianguo. Performance analyses of sensible heat storage systems for thermal applications. *Int J Energy Res* 1997;21(12):1157–71.
- Eames PC, Norton B. The effect of tank geometry on thermally stratified sensible heat storage subject to low reynolds number flows. *Int J Heat Mass Transfer* 1998;41(14):2131–42.
- Hasnain SM. Review on sustainable thermal energy storage technologies, Part i: Heat storage materials and techniques. *Energy Convers Manage* 1998;39(11):1127–38.
- Tamme Rainer, Laing Doerte, Steinmann Wolf-Dieter. Advanced thermal energy storage technology for parabolic trough. *J Solar Energy Eng* 2004;126(2):794–800.
- Fernandez AI, Martínez M, Segarra M, Martorell I, Cabeza LF. Selection of materials with potential in sensible thermal energy storage. *Solar Energy Mater Solar Cells* 2010;94(10):1723–9.
- Khare S, Dell'Amico M, Knight C, McGarry S. Selection of materials for high temperature sensible energy storage. *Solar Energy Mater Solar Cells* 2013;115:114–22.
- Prasad Likhendra, Muthukumar P. Design and optimization of lab-scale sensible heat storage prototype for solar thermal power plant application. *Solar Energy* 2013;97:217–29.
- Duffy Aidan, Rogers Martin, Ayompe Lacour. Renewable energy and energy efficiency: assessment of projects and policies. John Wiley & Sons; 2015.
- Miao Xing-Yuan, Beyer Christof, Görke Uwe-Jens, Kolditz Olaf, Hailemariam Henok, Nagel Thomas. Thermo-hydro-mechanical analysis of cement-based sensible heat stores for domestic applications. *Environ Earth Sci* 2016;75(18):1293.
- Miao Xing-Yuan, Zheng Tianyuan, Görke Uwe-Jens, Kolditz Olaf, Nagel Thomas. Thermo-mechanical analysis of heat exchanger design for thermal energy storage systems. *Appl Therm Eng* 2017;114:1082–9.
- Buscemi A, Panno D, Ciulla G, Beccali M, Lo Brano V. Concrete thermal energy storage for linear fresnel collectors: exploiting the south mediterranean's solar potential for agri-food processes. *Energy Convers Manage* 2018;166:719–34.
- Herrmann Ulf, Kearney David W. Survey of thermal energy storage for parabolic trough power plants. *J Solar Energy Eng* 2002;124(2):145–52.
- Laing Doerte, Bahl Carsten, Bauer Thomas, Fiss Michael, Breidenbach Nils, Hempel Matthias. High-temperature solid-media thermal energy storage for solar thermal power plants. *Proc IEEE* 2012;100(2):516–24.
- Miró Laia, Navarro Elena, Suresh Priyamvada, Gil Antoni, Fernández A Inés, Cabeza Luisa F. Experimental characterization of a solid industrial by-product as material for high temperature sensible thermal energy storage (tes). *Appl Energy* 2014;113:1261–8.
- Salomoni Valentina A, Majorana Carmelo E, Giannuzzi Giuseppe M, Miliozzi Adio, Maggio Rosa Di, Girardi Fabrizio, et al. Thermal storage of sensible heat using concrete modules in solar power plants. *Solar Energy* 2014;103:303–15.
- Skinner Joel E, Strasser Matthew N, Brown Brad M, Panneer Selvam R. Testing of high-performance concrete as a thermal energy storage medium at high temperatures. *J Solar Energy Eng* 2014;136(2):021004.
- Jian Yongfang, Bai Fengwu, Falcoz Quentin, Xu Chao, Wang Yan, Wang Zhifeng. Thermal analysis and design of solid energy storage systems using a modified lumped capacitance method. *Appl Therm Eng* 2015;75:213–23.
- Jian Yongfang, Falcoz Quentin, Neveu Pierre, Bai Fengwu, Wang Yan, Wang Zhifeng. Design and optimization of solid thermal energy storage modules for solar thermal power plant applications. *Appl Energy* 2015;139:30–42.
- Lizana Jesús, Chacartegui Ricardo, Barrios-Padura Angela, Valverde José Manuel. Advances in thermal energy storage materials and their applications towards zero energy buildings: a critical review. *Appl Energy* 2017;203:219–39.
- Laing Doerte, Lehmann Dorothea, Fiß Michael, Bahl Carsten. Test results of concrete thermal energy storage for parabolic trough power plants. *J Solar Energy Eng* 2009;131(4):041007.
- Laing Doerte, Bauer Thomas, Lehmann Dorothea, Bahl Carsten. Development of a thermal energy storage system for parabolic trough power plants with direct steam generation. *J Solar Energy Eng* 2010;132(2):021011.
- Laing Doerte, Steinmann Wolf-Dieter, Tamme Rainer, Richter Christoph. Solid media thermal storage for parabolic trough power plants. *Solar Energy* 2006;80(10):1283–9.
- Tamme Rainer, Steinmann Wolf-Dieter, Laing Doerte. High temperature thermal energy storage technologies for power generation and industrial process heat. In: *Proceedings of FUTURE-STOCK 2003, 9th international conference on thermal energy storage*. Warsaw, Poland; 2003.
- John Emerson, Hale Micah, Selvam Panneer. Concrete as a thermal energy storage medium for thermocline solar energy storage systems. *Solar Energy* 2013;96:194–204.
- Ozger OB, Girardi F, Giannuzzi GM, Salomoni VA, Majorana CE, Fambri L, et al. Effect of nylon fibres on mechanical and thermal properties of hardened concrete for energy storage systems. *Mater Des* 2013;51:989–97.
- Alonso MC, Vera-Agullo J, Guerreiro L, Flor-Laguna V, Sanchez M, Collares-Pereira M. Calcium aluminate based cement for concrete to be used as thermal energy storage in solar thermal electricity plants. *Cement Concr Res* 2016;82:74–86.
- Vejmelková Eva, Padevř Pavel, Černý Robert. Effect of cracks on hygric and thermal characteristics of concrete. *Bauphysik* 2008;30(6):438–44.
- Fu YF, Wong YL, Tang CA, Poon CS. Thermal induced stress and associated cracking in cement-based composite at elevated temperatures—Part i: Thermal cracking around single inclusion. *Cement Concr Compos* 2004;26(2):99–111.
- Fu YF, Wong YL, Tang CA, Poon CS. Thermal induced stress and associated cracking in cement-based composite at elevated temperatures—Part ii: Thermal cracking around multiple inclusions. *Cement Concr Compos* 2004;26(2):113–26.
- Martins Matthieu, Villalobos Uver, Delclos Thomas, Armstrong Peter, Bergan Pal G, Calvet Nicolas. New concentrating solar power facility for testing high temperature concrete thermal energy storage. *Energy Proc* 2015;75:2144–9.
- Pan Jianwen, Zou Renxin, Jin Feng. Experimental study on specific heat of concrete at high temperatures and its influence on thermal energy storage. *Energies* 2016;10(1):33.
- Martin Claudia, Bonk Alexander, Braun Markus, Odenthal Christian, Bauer Thomas. Investigation of the long-term stability of quartzite and basalt for a potential use as filler materials for a molten-salt based thermocline storage concept. *Solar Energy* 2018;171:827–40.
- Bourdin Blaise, Francfort Gilles A, Marigo Jean-Jacques. Numerical experiments in revisited brittle fracture. *J Mech Phys Solids* 2000;48(4):797–826.
- Bourdin Blaise, Francfort Gilles A, Marigo Jean-Jacques. The variational approach to fracture. *J Elast* 2008;91(1–3):5–148.
- Miehe C, Welschinger F, Hofacker M. Thermodynamically consistent phase-field models of fracture: variational principles and multi-field fe implementations. *Int J Numer Meth Eng* 2010;83(10):1273–311.
- Miao Xing-Yuan, Zheng Tianyuan, Kolditz Olaf, Nagel Thomas. Phase-field modeling of cracking processes in geomaterials for subsurface geotechnical engineering and energy storage. In: *Advance of computer methods in geomechanics: proceedings of the fifteenth international conference of the international association for computer methods and advanced in geomechanics*. Wuhan, China; 2017.
- Miehe Christian, Schänzel Lisa-Marie, Ulmer Heike. Phase field modeling of fracture

- in multi-physics problems. Part i. Balance of crack surface and failure criteria for brittle crack propagation in thermo-elastic solids. *Comput Meth Appl Mech Eng* 2015;294:449–85.
- [52] Francfort Gilles A, Marigo J-J. Revisiting brittle fracture as an energy minimization problem. *J Mech Phys Solids* 1998;46(8):1319–42.
- [53] Farrell Patrick, Maurini Corrado. Linear and nonlinear solvers for variational phase-field models of brittle fracture. *Int J Numer Meth Eng* 2017;109(5):648–67.
- [54] Sargado Juan Michael, Keilegavlen Eirik, Berre Inga, Nordbotten Jan Martin. High-accuracy phase-field models for brittle fracture based on a new family of degradation functions. *J Mech Phys Solids* 2018;111:458–89.
- [55] Tanné Erwan, Li Tianyi, Bourdin Blaise, Marigo J-J, Maurini Corrado. Crack nucleation in variational phase-field models of brittle fracture. *J Mech Phys Solids* 2018;110:80–99.
- [56] Kuhn Charlotte. Numerical and analytical investigation of a phase field model for fracture PhD thesis Technische Universität Kaiserslautern; 2013.
- [57] Ehlers Wolfgang, Luo Chenyi. A phase-field approach embedded in the theory of porous media for the description of dynamic hydraulic fracturing. *Comput Meth Appl Mech Eng* 2017;315:348–68.
- [58] Miao Xing-Yuan, Kolditz Olaf, Nagel Thomas. Phase-field modeling of fracture in poroelastic solids for thermal energy storage. *Poromechanics VI: proceedings of the sixth biot conference on poromechanics*. 2017. p. 1976–83.
- [59] Amor Hanen, Marigo Jean-Jacques, Maurini Corrado. Regularized formulation of the variational brittle fracture with unilateral contact: numerical experiments. *J Mech Phys Solids* 2009;57(8):1209–29.
- [60] Ambati Marreddy, Gerasimov Tymofiy, Lorenzis Laura De. A review on phase-field models of brittle fracture and a new fast hybrid formulation. *Comput Mech* 2015;55(2):383–405.
- [61] Gerasimov T, Lorenzis L De. A line search assisted monolithic approach for phase-field computing of brittle fracture. *Comput Meth Appl Mech Eng* 2016;312:276–303.
- [62] Klinsmann Markus, Rosato Daniele, Kamlah Marc, McMeeking Robert M. An assessment of the phase field formulation for crack growth. *Comput Meth Appl Mech Eng* 2015;294:313–30.
- [63] Ehlers Wolfgang, Häberle Kai. Interfacial mass transfer during gas-liquid phase change in deformable porous media with heat transfer. *Transport Porous Media* 2016;114(2):525–56.
- [64] Kolditz Olaf, Bauer S, Bilke L, Böttcher Niels, Delfs JO, Fischer T, et al. OpenGeoSys: an open-source initiative for numerical simulation of thermo-hydro-mechanical/chemical (THM/C) processes in porous media. *Environ Earth Sci* 2012;67(2):589–99.
- [65] Miehe Christian, Hofacker Martina, Welschinger Fabian. A phase field model for rate-independent crack propagation: Robust algorithmic implementation based on operator splits. *Comput Meth Appl Mech Eng* 2010;199(45):2765–78.
- [66] Bourdin Blaise, Marigo Jean-Jacques, Maurini Corrado, Sicsic Paul. Morphogenesis and propagation of complex cracks induced by thermal shocks. *Phys Rev Lett* 2014;112(1):014301.
- [67] Geyer John F, Nemat-Nasser S. Experimental investigation of thermally induced interacting cracks in brittle solids. *Int J Solids Struct* 1982;18(4):349–56.
- [68] Shao Yingfeng, Zhang Yue, Xu Xianghong, Zhou Zhiliang, Li Wei, Liu Boyang. Effect of crack pattern on the residual strength of ceramics after quenching. *J Am Ceram Soc* 2011;94(9):2804–7.
- [69] Jiang CP, Wu XF, Li J, Song F, Shao YF, Xu XH, et al. A study of the mechanism of formation and numerical simulations of crack patterns in ceramics subjected to thermal shock. *Acta Mater* 2012;60(11):4540–50.
- [70] Yu Kequan, Yu Jiangtao, Lu Zhoudao, Chen Qingyang. Determination of the softening curve and fracture toughness of high-strength concrete exposed to high temperature. *Eng Fract Mech* 2015;149:156–69.